Investigation of an Articulated Spine in a Quadruped Robotic System

by

Brooke M. Haueisen

A dissertation submitted in partial fulfillment
of the requirements for the degree of
Doctor of Philosophy
(Mechanical Engineering)
in The University of Michigan
2011

Doctoral Committee:

Professor Gregory M. Hulbert, Chair
Professor Jessy W. Grizzle
Professor Arthur D. Kuo
Assistant Research Scientist Jonathan E. Luntz

I have not failed. I've just found 10,000 ways that won't work.

-Thomas Edison

To my favorite engineer- my father

Acknowledgments

Many, many thanks are wished to everyone who has assisted with the formulation and execution of this research. Your help was immensely appreciated.

Special thanks are extended to my committee for all of their support, as well as all of the additional faculty that have helped along the way, especially Prof. Kokkolaras for his assistance with the optimization. Prof. Assanis, Prof. Awtar, Prof. Brei, Dr. Filipi, Dr. Garikipati, Prof. Gillespie, Prof. Hart, Prof. Koditschek, Prof. Kota, Prof. Saitou, Dr. Skerlos, Prof. Stein, Cynthia Quann-White, Matt Navarre and Bob Coury are thanked for all of their support and words of encouragement.

To my family, for always being there whenever I needed them. Dad, Mom, Dr. Anton, Eddie, Caitlin, Grandma Wil and George, Grandpa Chuck and Margaret, Grandpa Joe and Grandma Marge, Aunt Mary, Uncle Mark, Aunt Andrea, Uncle Mark, Uncle Chris, Aunt Gretchen, Uncle Roger, Aunt Adriane, Uncle Mike, Aunt Barb, Jamie, Shawn, Bobby, Lauren, Steven, Stephanie, Diane, Kristen, Nick, Cynthia, David, Uncle Joe, Fr. Vaughn, Aunt Kim and Uncle Henry. Without my family, I would not have been as successful in my scholastic endeavors. I love all of you and thank you for the continued support through my many ups and downs.

And last, but definitely not least, I want to thank all of my friends. Without your support (and libation sharing), I couldn't have made it through this long process. I want to especially extend thanks to Gina, Chris, Tyler, Rebecca, Chris, Rosanna, Howard, Tami, Mike, Bill, Brenda, Mike, Dmitri, Anya, Mike, Derek, Carlos, Yasmina, Serge, Stewart, Alicia, Aris, Nickoleta, Bruno, Rob, Jason, Dave, Kate, Mike, Brian, Colleen, Anupam, Rachel, Ryan, Sarah, Russell, Braden, Brian, Dave, Paul, Jerry, Doug, Peter, Steve, Dave, Greg, Jim, Connie, Chad, Jesse, Shiva, Harish, Eric, Geunsoo, Hao Pan, Jake, Sung-ick and so many others that I'm sure should be listed. Please know that I am eternally grateful to all of you.

Preface

The idea to study the articulation in the spine started from a series of passive dynamic experiments with a Tinkertoy walker and a robotic mule prototype. Through various iterations, this idea blossomed into the document before you. It has been a long journey, but well worth the many hills and valleys passed over and through along the way. With the burgeoning research in the area of cheetah mobility and robotics, perhaps this work will provide additional encouragement for improvements in future systems.

Table of Contents

List of Tables

Table

List of Figures

Figure

List of Appendices

Appendix

Abstract

An efficient, high-speed quadruped robot is useful in applications spanning the service and entertainment industries. The military is also keenly interested in this platform as legged, robotic convoys for soldier support are becoming technically viable and a battlefield necessity with skirmishes in rough, unstructured terrain, inaccessible to wheels and tracks. Legs have the advantage in this domain and motivates the investigation of this mobility mechanism.

The research presented here quantitatively analyzes a multi-body dynamics quadrupedal model with an articulated spine to evaluate the effects of speed and stride frequency on the energy requirements of the system. The planar articulated model consists of six planar, rigid bodies with a single joint in the middle of the torso. All joints are frictionless and mass is equally distributed in the limbs and torso. A model with the mid-torso joint removed, denoted as the rigid model, is used as a baseline comparison. Impulsive forces and torques are used to instantaneously reset the velocities at the phase transitions, allowing for ballistic trajectories during flight phases. Active torques at the haunch and shoulder joints are used during the stance phases to increase the model robustness. Simulations were conducted over effective high-speed gaits from 6.0 - 9.0 m/s. Stride frequencies were varied for both models. An evolutionary algorithm was employed to find plausible gaits based on biologically realistic constraints and bounds. The objective function for the optimization was cost of transport.

Results show a decreasing cost of transport as speed increases for the articulated model with an optimal stride frequency of 3 s^{-1} and an increasing cost of transport with increasing speed for the rigid model at an optimal stride frequency of 1.4 s^{-1}, with a crossover in the cost of transport between the two models occurring at 7.0 m/s. The rigid model favors low speeds and stride frequencies at the cost of a large impulsive vertical force, driving the system through a long, gathered flight phase used to cover the long distances at the low stride frequencies. The articulated model prefers higher speeds and stride frequencies at the cost of a large impulsive torque in the back joint, akin to the contraction of abdomen muscles, preventing the collapse of the back. Thus, it is demonstrated that the inclusion

of back articulation enables a more energetically efficient high-speed gait than a rigid back system, as seen in biological systems. Detailed analysis is provided to identify the mechanics associated with the optimal gaits of both the rigid and the articulated systems to support this claim.

Chapter 1
Introduction

1.1 Goals in Brief

The *primary* contribution of this research is to qualitatively analyze a multi-body dynamics quadrupedal system with an articulated torso, focusing on the influence of the spine articulation on speed and energy requirements compared to a rigid-backed model. A *secondary* contribution of this research is developing tools with which to analyze a multi-body, articulated system with metrics providing meaningful system insight.

To achieve these goals, two models were developed. Both models are composed of planar, rigid bodies connected by frictionless, revolute joints. Each rigid body has an equally distributed mass. To simplify the system dynamics, a 'virtual' leg is created by joining a pair of legs into a single body. The front and rear legs are combined into one leg with a joint connecting two equal length limbs. In conjunction with this simplification, a symmetric approximation of the high-speed gallop gait is employed in the form of the bound.

The baseline model has a rigid torso, connecting the front and rear leg pairs. The model described is well studied at low speeds (less than 10 bodylengths/s), with little work done at speeds greater than 10 bodylengths/s. Speed is a desirable performance characteristic, typically sacrificed due to high energetic costs. However, biology shows that it is possible to have a fast *and* efficient system (64). Motivated by animals such as the the cheetah and greyhound, a second model was built. The model shares all of the same characteristics as the rigid model but includes a single node of articulation in the middle of the torso, allowing sagittal plane motion. Using an appropriately constrained optimization, the hypothesis is that with an articulating spine, better foot placement options should be able to reduce the system's energetic requirements in comparison to a model with a rigid spine running under similar conditions.

1.2 Motivation

As robots continue to play a growing role in various aspects of our lives, the need for improved understanding of their capabilities increases. Ranging in application from domestic chores to bomb disposal, robots are playing pivotal roles in the new technological frontier. One such vital role is providing support for the nations' troops on and off the battlefield. Soldiers' packs are increasing in weight as their needs in the field grow. Standard issue equipment can reach upwards of 100 lbs. A possible solution to this weighty issue is to remove non-essentials from the soldiers' packs and redistribute these items to a robotic convoy. Quadruped robots are one possibility that the military is pursuing to address this issue. As with robots in general, the quadruped robots suffer from limited range due to restricted on-board power density, slow speeds and constrained mobility.

Looking to biology for inspiration has led to many advances in robotics [(16), (42), (76), (85), (128)] . From cockroaches to lizards, it is clear that evolution has perfected these systems to ensure survival. The animal kingdom, in general, provides a good starting point for successful systems that excel in areas where robots have concerns. In particular, speed is not an issue for many animals and especially members of the biological family *Felidae.* The member of this family of interest is the *Acinonyx jubatus*, more commonly known as the cheetah. This phenomenal creature has statistics that would make a gearhead drool- not only can it reach average speeds of 70 mph, it can accelerate from 0 to 60mph in 3 seconds (134). This incredible speed can be linked to its large hind leg muscles and to another feature that all mammals share to some degree. When watching a cheetah in pursuit of its prey, it is clear that the spine is not rigid, but rather a highly flexible part of the anatomy. Using insight from this natural system, the research here focuses on extending the capabilities of quadruped robots through the addition of a flexible spine. The primary aim of the research is to develop an articulated model of a quadruped in order to determine changes in speed, mobility and energetic costs to improve the operating performance.

The applications, beyond military, where a highly mobile quadruped robot would be of use, reach into the medical field (for hospice care [(34),(151)]), entertainment [(40), (46),(69)], search and rescue operations (33), and law enforcement (102).

1.3 Outline

The dissertation is composed of several parts, beginning with the background. This section gives an overview and brief history of robotic technology, focusing on the use of legs. The biological motivation for the present study is presented with particular emphasis on

quadruped mammals. The modeling chapter provides the details on the construction of the simulations used to prove the hypothesis, including all constraints, bounds, assumptions and modeling parameters. The results and analysis chapter organize the outcomes of the various trials to evaluate the inclusion of the spine in a quantitative fashion. Lastly, the conclusions from the study are presented and further research directions addressed.

Chapter 2
Background

2.1 Literature Review

The literature review looks at the state-of-the-art in articulated robotic research and how the current research provides a meaningful contribution. This chapter is organized as follows: a history of relevant robots, a discussion of the advantages and disadvantages of various modes of mobility, and finally, an overview of the robots and models that are pertinent to the development of the current simulation.

2.1.1 A Brief History

In order to have a more complete understanding of robotics, it is useful to look at their history, starting with automata. Some of the most famous automata were built by Jacques Vaucanson, including a flute player with complicated mechanisms to simulate the different air pressures, tongue positions, and fingering needed to produce a tune, as well as a duck that acted (quacked, flapped, swam, moved) like a real duck (124) including the consumption, digestion, and excretion of food (Fig. 2.1). These mechanical marvels employed a mechanism similar to that of a music box- a cartridge with subtle pockets and pads that activated a series of levers and gears to allow the automaton to move, seemingly of its own accord.

Following the duck, Vaucanson developed an automatic loom based on his success with his automata. One of the initial responses to the machine was a revolt by the workers, motivated by the fear that they would be replaced, a theme that has echoed throughout history in connection with robots. In 1804, Joseph-Marie Jacquard introduced punch cards into his version of the automatic loom, based on Vaucanson's original design, to create complex patterns. This addition of punch cards would later influence Charles Babbage during the 1830's, when he attempted to create the Difference Engine, a precursor to early computers.

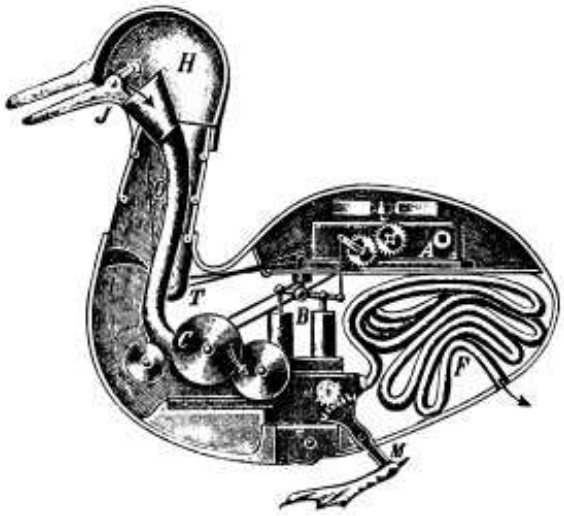

Figure 2.1 Vaucanson's Automaton Duck

In terms of etymology, the word 'robot' first appeared in Karel Capek's play R.U.R. (Rossum's Universal Robots, (28)) in 1921, from the Czech word for forced labor. The artificial people (known as 'robots' in the play) were created as a way for the worker to have someone to do their monotonous work for them.

> "I wanted man to become the master, so that he shouldn't live merely for a crust of bread."

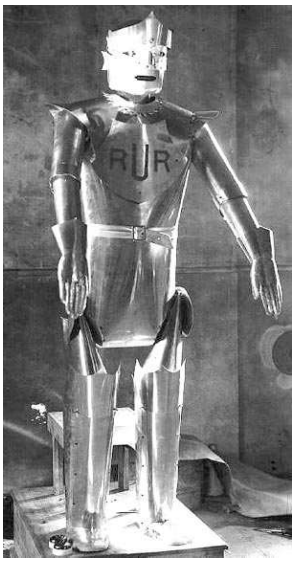

Figure 2.2 Rossum's Universal Robot

And thus, the motivation for mechanical creatures was codified. The fascination with the machines has continued to play a prominent role in movies, books, plays and songs, playing with the notion of exactly how far machine intelligence will go.

Aside from the Hollywood versions, the scientific field of robotics continued to progress with the development of the CNC Machine at MIT in the 1950's, and the Unimate robot by George Devol and Jospeh Engelberger in 1956 (Fig. 2.3). The first Unimate to be installed was at GM in 1961 to work with heated die-casting machines, fulfilling its role of performing jobs that were dirty, dull and dangerous.

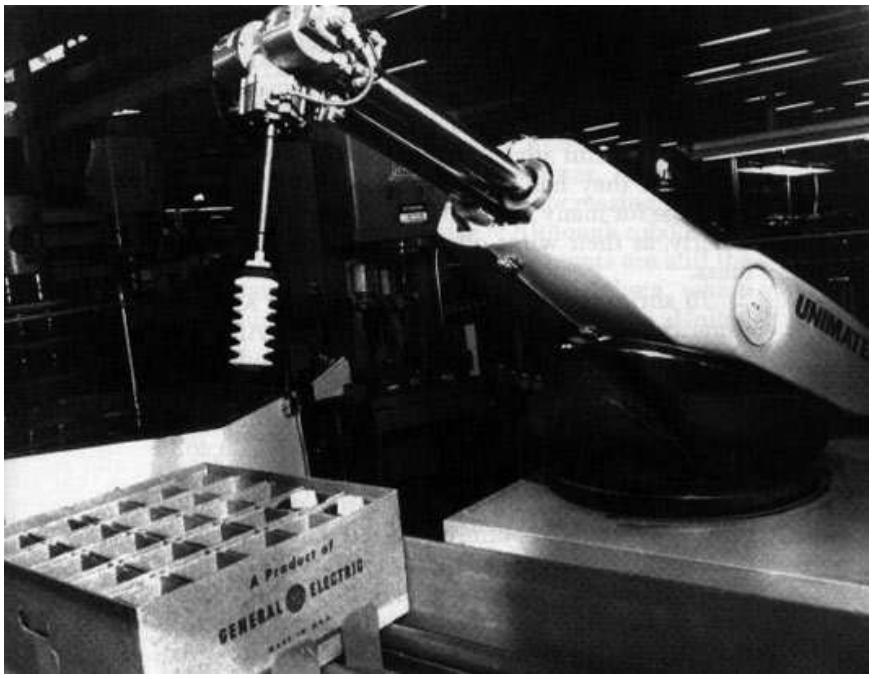

Figure 2.3 Unimate Robot

Along with their progression into the entertainment mainstream, most notably Honda's humanoid ASIMO, and Sony's robotic dog AIBO (41) and dancing humanoid QRIO (69), robots have also taken on domestic duties. The 21^{st} century has seen a surge in the popularity of robotics and witnessed its progression into previously unseen facets of life. From the socially interactive Kismet (25), to the babysitter bot PaPeRo (109) (Fig. 2.4), robots are becoming more sophisticated with enhanced sensors and materials, allowing for advanced interactions with a softer, human-like touch, facial recognition and learning algorithms, improving a multitude of tasks.

The recent insurgence of robots into every day life has also been seen in the military, where robot use has risen dramatically. With the field's continual advances, robots have proven their mettle as life-saving tools. As Sgt. Francisco Huereque explains in a Nov. 2004 Wired News article ("Save Soldiers by Remote Control"),

> "We fill some of the gaps in the intelligence field. We put one of these in harm's way instead of a soldier. It's all about saving lives."

iRobot is a company that has bridged the gap between domestic and military robots. The

Figure 2.4 Kismet and Papero robots

company is most well known for its household autonomous vacuum cleaner Roomba and their highly durable and mobile man-packable military robot, PackBot. PackBot has become a regular in the military, with tasks ranging from cave scouting, vehicle inspections, mine retrieval and bomb disposal, to name a few. During a search for roadside bombs,

> "One robot was blown up. That was a cause for celebration, because the robot saved the life of a soldier."

The quote is from retired Vice Adm. Joe Dyer, general manager of iRobot's government and industrial robotics division (*Wired News*, "Robots May Fight for the Army", April 13, 2004).

When thinking of lightweight unmanned ground vehicles (UGV's) for use in the military, wheeled and tracked configurations of robots will certainly come to mind. Systems like the three-wheeled Omni-Directional Inspection System (ODIS) are used to inspect vehicles passing through checkpoints and come equipped with vision and chemical sensors to detect possible hazardous materials. The aforementioned PackBot is used for activities ranging from scouting to improvised explosive device (IED) detection. However, legged systems are quickly on their way to being integrated into the robotic military. One such system, known as BigDog, may be used as part of a robotic convoy for transporting mission supplies.

As the face of war changes and the battlefields are shifted to increasingly remote, inaccessible portions of the world, the necessity for legged transport becomes more apparent. A US Army report stated that only 50% of the Earth's land surface is accessible to wheeled

or tracked vehicles (125), and in a 2002 *Foreign Affairs* article, Donald Rumsfeld describes the new war zone:

> [The troops] sported beards and traditional scarves and rode horses trained to run into machine gun fire. They used pack mules to transport equipment across some of the roughest terrain in the world, riding at night, in darkness, near minefields and along narrow mountain trails with drops so sheer that, as one soldier put it,'it took me a week to ease the death grip on my horse'.

His conclusion was that the old paradigms of battle are changing, and the military needs to change with them. Robots are one aspect of how the military is addressing these needs.

The narrow trails and unstructured ground of this new battlefield (requiring specially trained horses) is well-suited to the use of legged robots which don't have the disadvantages of live animals. Although wheeled and tracked robots have the advantage of a simpler, more commonly used platform, they are limited to relatively flat terrain with minimal obstructions, whereas legs are not. The various benefits and drawbacks of these systems will be evaluated in the following section.

2.1.2 Wheels, Tracks or Legs?

The following section describes a small subset of UGV's of growing interest for the military. These systems weigh under 300 lbs and are primarily used for government applications. The three main categories of robots, from a mobility standpoint, are wheeled, tracked, and legged (Fig. 2.5). Wheels and tracks compose the majority of military robots, with new legged systems close to being fielded.

Figure 2.5 Wheels, Tracks and Legs

2.1.2.1 Configurations

The wheeled robots discussed here have wheels as their primary mobility mechanism, using two to six wheels and a total weight under 300 lbs. Solid rubber or inflated rubber

tires with various types of tread are used. Depending on the number of wheels and layout, various steering mechanisms are employed like Ackerman or differential.

The highlights of this technology are the speed (when on paved roads or defined paths) and the commonality of platform. These characteristics allow for easy commercial, off-the-shelf part integration and replacement. Wheels have also been one of the most popular commercial means of mobility, creating a rich history and expansive knowledge base. Wheels are a reliable technology, therefore a logical first choice.

However, there are some constraints to the system. Their high speed achievement is limited to well structured environments. Obstacle negotiation is typically half the height of the wheel (unless some articulation is used).

Tracked robots have various configurations. The majority of those in the lightweight military category have a band of tread that is wrapped around the entire length of their body and can be made of either continuous rubber or interlocking pieces of metal / plastic to create the track. Some of these have additional flippers for mobility. This added feature allows some of these machines to overcome obstacles that would otherwise be insurmountable. This will be addressed in more detail when discussing the individual robots. Directionality is accomplished through variable speed of the left/right treads (skid steering).

The main advantage of the tracked systems is the distribution of weight over a large area, decreasing the ground pressure, as opposed to wheeled vehicles. This enables the tracked vehicles to venture into less structured terrain, such as mud and sand, with veritable ease when compared to their wheeled and legged counterparts.

Disadvantages include slower speeds and less maneuverability but a tighter turn radius than wheeled. The tracked robots are still limited in their obstacle negotiation, although they have some advantage to the wheeled robots. With the continuity of the tread in contact with an obstacle, the tracked robots can overcome obstacles that are the height of their guide wheel.

The last type of mobility methodology, for the purposes of this discussion, are legs. As in nature, there are a variety of configurations for these. Typically, the robots in this category have either two, four, or six legs. Leg design is a key feature in the robots and is one determinant of how quickly and agilely the robot can move. Steering is accomplished similarly to tanks using something akin to skid steering- speeding up or slowing down the limbs on either the left or right hand side. These machines can also turn around on the spot. Foot design is also an important design characteristic of these robots but the majority use the approximation of a point foot contact. Obstacle negotiation is not easily classifiable but is usually around shoulder height for the legged robot.

While legged robots are still relatively young in terms of their technology, they hold

a great deal of promise. A legged platform enables the robot to have an isolated foothold that provides for a more precise placement of the foot in unstructured terrain, allowing access to areas wheeled and tracked vehicles cannot reach (Fig. 2.6). This isolated foothold also enhances the potential stealth capabilities as path traversal is less obvious for a legged system in comparison to a wheeled or tracked vehicle where an obvious path remains after traversal. The potential for increased speed and maneuverability over comparable wheeled or tracked vehicles of similar size in off-road terrain is possible. These characteristics and power / efficiency benefits will be discussed later.

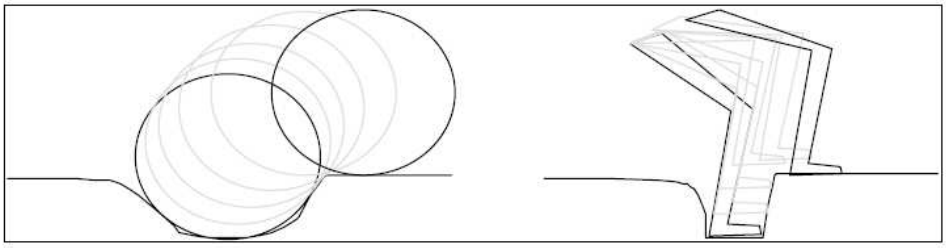

Figure 2.6 Wheel and leg moving out of a localized depression

The major disadvantage is that many of these advantages are still theoretical. Looking at existing legged robot technologies, there are a myriad of issues. Power density is a problem (although this can be said of wheels and tracks of similar size). Fall recovery can be difficult or non-existent. The increased complexity of the designs is also an issue. With increased complexity comes increased cost and repair/replacement difficulties. Control of walking machines is more complex than in wheeled and tracked vehicles.

One such government funded project to extend legged systems known as Big Dog (see Fig. 2.7), hopes to fill this gap in technology with a quadruped robot used to assist soldiers by carrying equipment and supplies. A typical soldier carries about 100 lbs of supplies in his pack. Lightening some of this load would enable the soldier to go for longer periods of time with less fatigue and a decreased likelihood of injury. The goal of the Big Dog project is to develop a 'power autonomous quadruped capable of carrying significant payloads, operating outdoors, with static and dynamic mobility, and fully integrated sensing' (113). Boston Dynamics, the main contributor to Big Dog, has done just that. Their physical prototype walks over loose rocks, through ankle-deep snow, on ice, and carries 50 kg or more of payload. It is an amazing prototype, but there is always room for improvement. What if it were possible to increase the speed, stability, robustness and mobility, and/or reduce power and energy requirements, giving soldiers better range, maneuverability or efficiency over more difficult terrain with fewer stumbles and able to keep pace with their human counterparts? One possible solution is to look at what biology has done to address these issues- the inclusion of an articulated spine.

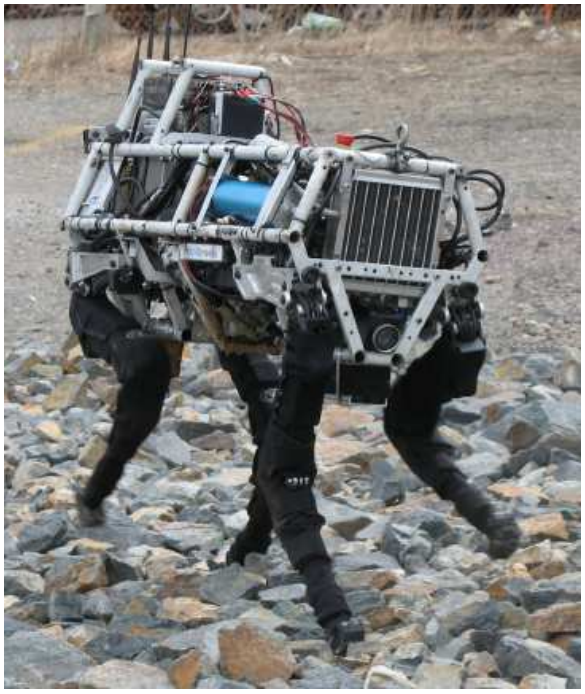

Figure 2.7 Boston Dynamics' Big Dog Quadruped Robot

2.1.3 Advantages of an Articulated Spine

Consider the cheetah. It is the fastest land animal, running at speeds close to 60 mph. As a cheetah runs, it is visually apparent that the back is not a rigid entity but rather a fluid, bending part of the body that enables the animal to move quickly and lithely. With the additional movement provided by the spine, a larger range of body configurations are available for the animal, creating possibilities for mass distributions that enhance stability and mobility, otherwise unavailable to a rigid-spined system. In addition, the flexibility of the spine can be likened to a spring which has energy storage capabilities. In this mode, the articulated spine can decrease energy and power requirements. Each of these advantages will be addressed from a biological standpoint in order to gain an understanding of spines' overall contribution to the system.

2.1.3.1 Speed

Hildebrand (60) pioneered much of the work regarding locomotion studies with the horse and cheetah. He lists the major contributions of the flexion and extension of the back on the animals' speed as the following:

- As the swing of the limbs increases, the distance covered during the aerial phase is increased.

- With the combination of spine muscles and limb muscles working concurrently, the limbs move faster than a single group of muscles working alone.
- The spine adds to the maximum forward extension of the legs, increasing the maximum backward acceleration of the limbs before they strike the ground.
- The spine aids in moving the body forward in an inch-worm fashion.
- The spine reduces the relative forward velocity of the girdles when their respective limbs are moving the body.

Additional studies by Hildebrand (61), showed an increase in speed of 10% due to the flexion / extension of the spine in the cheetah. Increasing the speed of current legged robots by 10% would benefit time-sensitive situations like reconnaissance missions, critical in the military. It would also allow a larger range based on an equivalent power supply (assuming all other factors held constant).

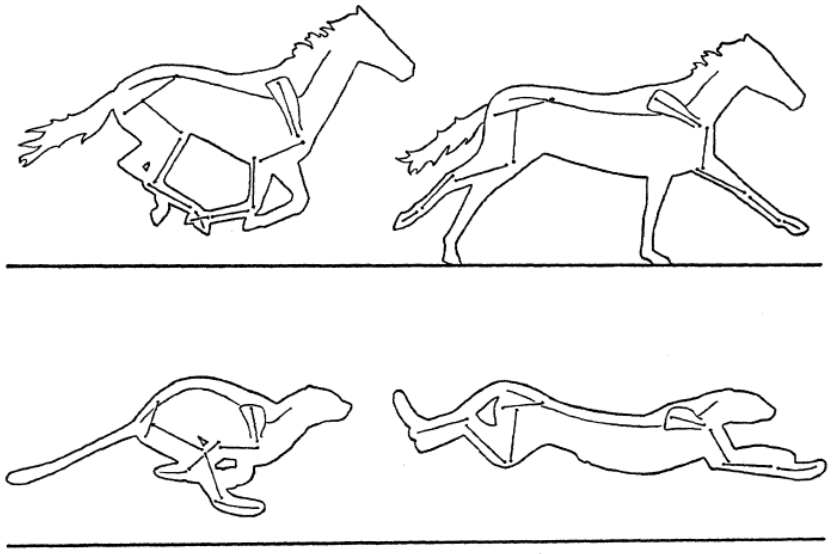

Figure 2.8 Hildebrand's sketches of flexion / extension in spine of horse and cheetah

2.1.3.2 Robustness and Mobility

Other critical characteristics of legged robots are the robustness and mobility of the system. If a robot is out in the field and cannot recover from a simple system perturbation, such as a bump or push from a solider, then the mission will be a failure. As in traditional systems, a marginally stable system can gain great advantages in speed and maneuverability. Incorporating a flexible spine has the potential to increase speed and maneuverability, while extending the robustness and mobility. The flexibility of an articulated spine provides added configuration options of the body and feet within the appropriate support polygon.

Biological insight has been provided by Hackert [(49), (50)] with the pika, and by Gra-

covetsky (45) in humans. In the experiments with the pikas, cineradiography was used to analyze the kinematics of the body to observe how the spine moves during the half-bound gait (Fig. 2.9). The study shows the flexion of the spine causes a change in the trunk's mass distribution aiding in the body's self-stabilization. The large flexion-extension of the spine enables the body to maintain a flatter trajectory of the center of mass, decreasing inertial effects that contribute to destabilization of the biological system. Although not directly related to the spine, the work of Daley and Biewener [(32)], demonstrates that as long as the center of mass remains relatively flat, the body is able to recover from unexpected perturbations. Their findings suggested that the limb contact angle, rather than the spring coefficient of the leg, dominates the stability parameters of the system.

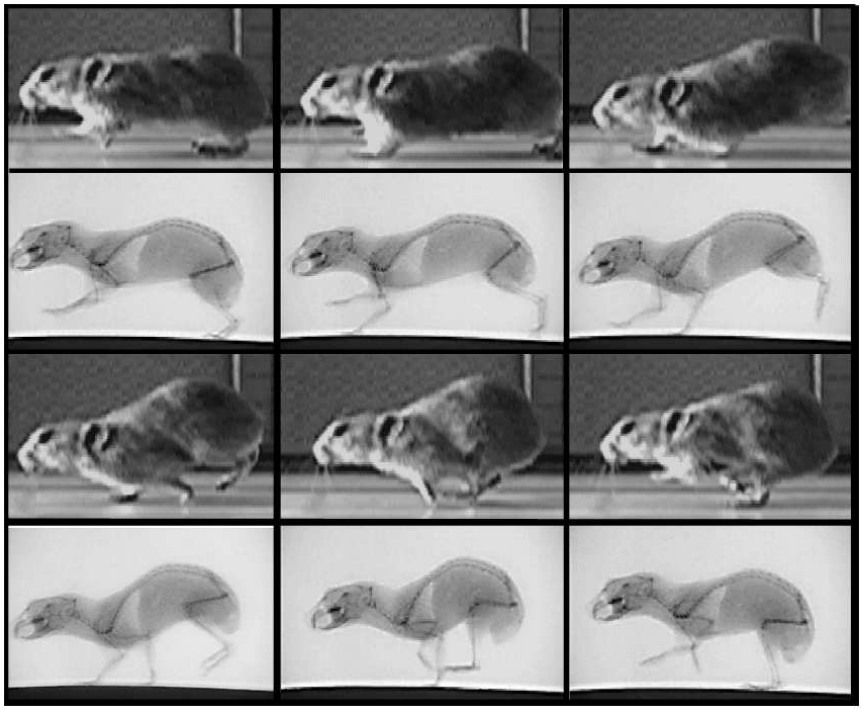

Figure 2.9 Pika in half-bound

Hackert's work [(50),(129)] with the pikas is also key in regards to system robustness. The self-stabilization characteristics of the flexible spine enable a wide range of dynamically stable, statically unstable gaits. The mobility, as discussed subsequently, allows the system to recover from falls and move in ways to enable a greater range of movement- both contributing to the robustness of the system.

English's work (36) looked at the function of the lower spine when a cat walks. His work demonstrates that the flexion of the spine adds to the step length of the cat and dampens vertical fluctuations in the center of mass during walking and trotting. The spine is a stabilization mechanism, and for many quadruped mammals, used to control the pelvis.

Although the main focus of the work is on quadrupeds, bipeds can also provide insight into the advantages of a flexible spine (138). Gracovetsky pioneered much of the work in looking at how the spine drives motion. In one of his experiments, he placed human test subjects in back braces that prevented the upper torso of the body from rotating during normal walking gait experiments. The restriction of the upper body caused abnormal gaiting and difficulties in maintaining balance. The rotation of the spine enabled stabilization of the head, also affecting the balance of the body.

From the studies in spinal fusion, it can be seen that the gait adjusts to accommodate for the impaired mobility, with increased energy requirements and lateral stability issues [(26),(30),(35),(89)]. Much of the work focused on the immobility of systems due to spinal injury centers around quadrupeds and humans [(35), (107), (138)] but some work done with insects sheds light on the link between the spine and stability. The simpler construction of insects provides insights into the mobility advantages of an articulated spine. Many insect species' articulating spine can be simplified to a single node in the back, operating between the thorax and abdomen. The work done by Ritzmann on cockroaches (126) clearly shows a decrease in obstacle negotiation with a fixed spine versus a segmented spine. His experiments focus on how the spine and pelvis are connected to each other and the mechanical advantage of the limbs when a) the body is allowed to move normally and b) the thorax region is fixed. With the thorax region fixed (in essence, removing the articulation of the spine), the cockroach 'high-centers'- a case in which the center of mass of the animal cannot be adjusted to bring it closer to the obstacle. This high-centering results in an elongation of the limbs that decreases their mechanical advantage, necessary for the creature to overcome certain obstacles (see Fig. 2.10).

Other demonstrations of the mobility of the spine can be seen in the climbing ability

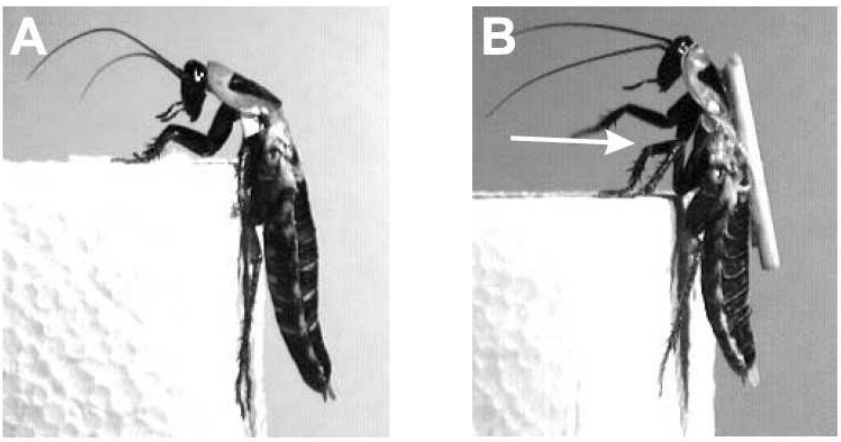

Figure 2.10 Ritzmann's A) Articulated and B) Fixed Spine Cockroaches

(23) of some cursorial animals. Leopards, especially, spend a great deal of time in trees. Without the articulation of the spine, this would be a difficult feat. Another animal using the articulation of its spine for unique mode of mobility is the click beetle (37). This particular species stores potential energy during the flexion of the spine, aided by a peg. Once the animal is ready, it catapults its body in a legless jump. Looking at the most extreme case of an articulated spine is the serpent. This animal has the capability of many different gaits, giving it surprising mobility in a variety of environments, even without the use of legs. In contrast, one could look at the tortoise which has a rigid body, short segmented legs and limited mobility. Once on its back, the tortoise has difficulty in righting itself. Even using a model with single node of articulation can increase the mobility and stability of a system as demonstrated in the two-link cat robot (144).

The main difficulty with robustness and mobility is quantifying them. There are few metrics that are able to concretely describe these system qualities. Rather, they are presented in order to give additional benefits for an articulated system.

2.1.3.3 Power and Energy Requirements

Another metric aided through the inclusion of a segmented spine deals with the reduction of power and energy requirements for a system. Without the necessary power, a system can be easily incapacitated. Most robotic systems utilize some type of battery, although battery technology is still limiting. The quadruped Big Dog uses a 17 hp, two cylinder combustion engine with hydraulic actuators for its power source (113). If it were possible to increase the range of a robot by decreasing its power and energy requirements, it would be a highly attractive prospect for an unmanned system. Experiments in the biological field have provided insight into the energy storage capacity of elastic structures in the backs of animals. Using nature as a guide, it may be possible to reduce the power and energy requirements in a robotic system through the use of an articulated spine.

Hoyt and Taylor (64) conducted experiments to calculate the amount of oxygen consumption by horses trained at various gaits. Their hypothesis was that nature optimizes itself and adjusts the gait to minimize energy requirements. The particular unforced gait chosen by the animal reflects an energetic minimum. The theory was corroborated through experiments demonstrating the subjects (horses) changing from a walk to a trot, and a trot to a gallop, when oxygen consumption increased, revealing that each particular gait required approximately the same amount of energy (Fig. 2.11) at the animals' naturally selected gait for a particular speed range. This indicates that for a certain critical speed, galloping is more economical than trotting.

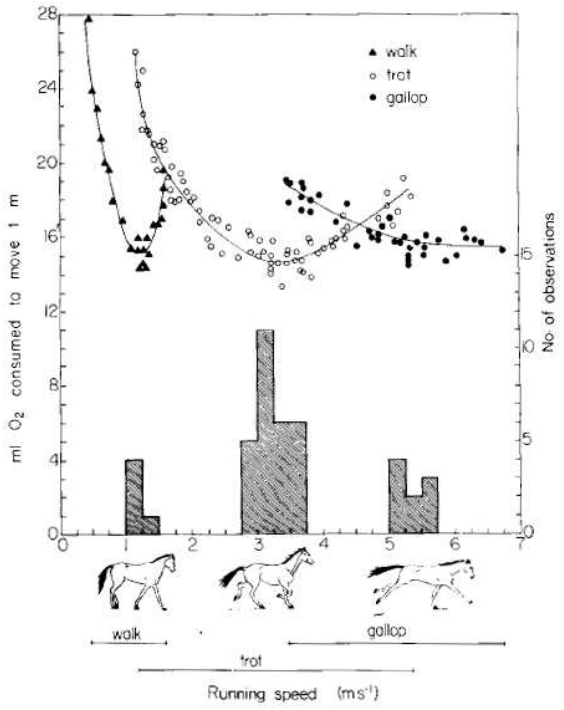

Figure 2.11 Hoyt and Taylor's Oxygen Consumption Plot for Horses at Different Gaits

R.M. Alexander has done substantial research on the gait and energetics of biological systems [(6), (7), (9), (10), (11), (142)]. One key work that addresses the biological optimization observed by Hoyt and Taylor details the energy saving mechanisms of elastic structures in the back (8). This work looks at the energies (internal and external) during the gallop of fallow deer and dogs. At high speeds, the internal energy fluctuations are at their maximum. During these large changes, the elastic structures, specifically the aponeurosis (a tendon-like mechanism in the back that acts like a spring), are able to store energy, reducing the power necessary during high speed gaits. Fig. 2.12 shows a sketch of the variation of the energies during the flexion/extension of the body in a galloping gait. Without articulation, this energy savings would not be possible.

All of these characteristics (speed, robustness/mobility, power/energy requirements) interrelate and work together in biological systems to create the optimal creatures that are observed in the world around us. The field of biomimetic robots takes its cue from this ideal and looks to build systems that make use of the optimization that evolution has provided as guidelines [(4), (14), (56), (76), (128)]. In the process of building these robots, much about their biological counterparts has been revealed. In the next section, the prior art, critical to the development of articulating robots, is evaluated to see where the field stands.

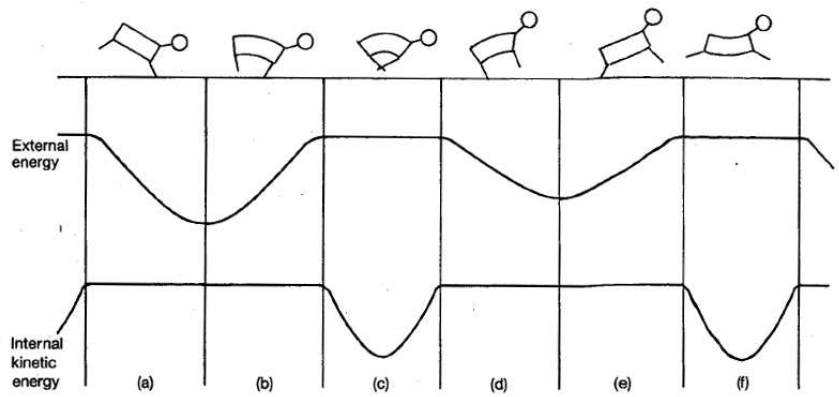

Figure 2.12 Alexander's Diagram of the Energy Fluctuations in a Galloping Mammal

2.1.4 Prior Art

After looking at the biological evidence of the benefits of the articulated spine, it is important to see how the robotics community has implemented these concepts and compare those prototypes to their rigid-spined counterparts. As has been noted with legged vehicles in general, the advantages range from enhanced terrain negotiation, due to the use of isolated footholds, to the decoupling of the payload from the body allowing for smooth transportation of goods over unstructured terrain (118).

2.1.4.1 Non-articulating Quadruped Robots

There are a number of legged walkers and their history has been well-documented [(118), (140)]. From Chebyshev's early walking mechanism in 1850, to GE's walking truck in 1968, legged robots have made great strides. Some rigid-spined quadrupeds of note include the Tekken series (76), which focuses on a small dog-like quadruped using a central pattern generator to study reactive control methodologies, Patrush (75), another quadruped in a similar vein to Tekken using a neural oscillator for control, and the group of dog-like quadrupeds from the AI Lab in Zurich known as Puppy and Mini-dog (68). The MIT Leg Lab also put together a quadruped robot that trotted, paced and bounded (120). Boston Dynamics' Big Dog has captured the spotlight in terms of quadruped robotic research.

2.1.4.2 Articulating Quadruped Robots

There has been considerably less work done in the field of articulating robots. To traverse the spectrum of articulation, there are the continuum robots (for example, the elephant trunk

(51) and eel robots (3)), the multi-segmented robots (Choset's snake robots and Bornstein's Omni-tread robots), and the single articulation models. These will be addressed in detail.

Stumpy is a simple hopping robot (66) with a pegged base and single articulation in the middle of the body (Fig. 2.13). The robot moves through an applied torque at this articulation point and hops around. The system uses an open-loop reactive based control structure to achieve some simple gaits and directionality. This robot is part of a series of prototypes based on cheap design and ecological balance (112). The use of the articulation to drive the motion of the robot is confirmation of one of the biological experiments done with a quadriplegic test subject in *The Spinal Engine* (45). These works demonstrate that the use of an articulated spine can be the primary motion generator in an animal or human.

Figure 2.13 Stumpy, the Hopping Robot

A four-segment legged robot with single joint articulation, BISAM (Fig. 2.14), can rotate in the sagittal plane for mammalian gaits, and, in the transverse plane, for reptilian gaits. The articulation in the spine (19) was investigated using a biologically inspired adaptive control concept. Subsequent research with this robot (5) focused on learning gaits using advanced reinforcement learning techniques for posture control during movement.

ELIRO is a unique example of an articulating robot (Fig. 2.15). Its main focus is not articulation, but rather eating (ELIRO stands for Eating LIzard RObot). It can bend passively

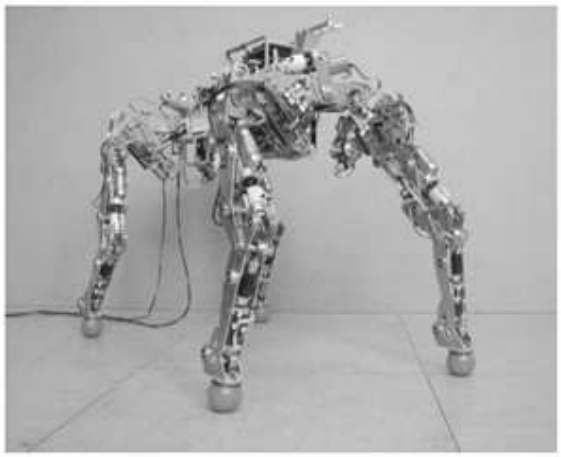

Figure 2.14 BISAM Robot

in the transverse plane and actively in the dorsal plane. The initial work looked at a zig-zag gaiting methodology [(74), (110)] utilizing the articulation in the spine for the negotiation of narrow spaces and direction changes, based on rotation around the articulating node. Subsequent work focused on the autonomous eating mechanism of the robot (70).

Figure 2.15 ELIRO Robot

Ikuo Mizuuchi created a line of articulated robots, starting with a quadruped known as SQ43 ((88) , Fig. 2.16). More robots followed but all in the humanoid articulated spine form [(90), (91), (93), (94)]. In the SQ43 prototype, the spine is a multi-segmented body integrated into the quadruped with a genetic algorithm as the motion generator (92). The system incorporated finite element methods to model the spine. The motivation for using an articulated spine in these works addresses the physical *softness* of the interaction between humans and robots (in the cases of the humanoids Kenta and Kenji), the limited walking speed (in the quadruped SQ43), and more generally, the ability to perform a plethora of tasks and motions inside of the diverse environments robots operate. The use of the spine is also able to diffuse harsh forces by applying the load along its length rather than at a localized point.

GEO has a three degree of freedom spine (Fig. 2.17). Its control uses central pattern generators (CPG), postural reflexes, and forward models to adaptively tune the CPG's (86). The body was able to rotate in and out of the sagittal and transverse planes with a twist-slide

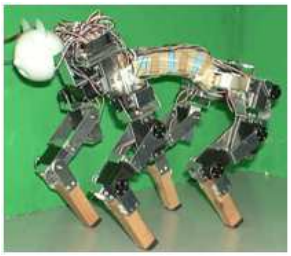

Figure 2.16 SQ43 Robot

mechanism. Other interesting experiments involved using the reflex controller to adjust the stability of the robot in response to different weights placed in various locations on the body. Since then, the group has moved on to CPG's for bipeds.

Figure 2.17 GEO Robot

Leeser at MIT's leg lab developed a planar quadruped robot with articulated spine (Fig. 2.18). The work looked at the role of the spine and trunk as providing three functions: increasing the effective leg length, storing / transferring energy, and providing auxiliary power to legs (84). Future applications were suggested using the spine as a way to control mass distribution in-flight for better foot placement when landing. Leeser also suggested an additional translational degree of freedom to mimic the inch-worm effect, including an extension of the body through the spine. This would allow for better acceleration of the forequarters of the body but was not included in this iteration.

The Whegs (Fig. 2.19) series of robots from Roger Quinn's group at Case Western uses a passively compliant, actively controlled body joint that allows the body to rotate in and out of the dorsal plane [(5), (14), (96)]. The robot is a six-legged, wheel-leg hybrid prototype moving into full production. Although this is a hexapod robot, it shows the simple and effective implementation of the articulated back in a physical system. The passive compliance in the axles allowed for additional mobility of the robot and gait changes with a timing mechanism that responded to a leg encountering an obstacle or variations in terrain (preflexive locomotion control system embedded in the mechanics of the robot).

An example of a multi-segmented, articulated robot with passive legs is the salamander robot (Fig. 2.20) moving between water and land using CPG's and reflex controllers to swim, crawl and walk [(24), (31), (111)]. One major difference between this classification

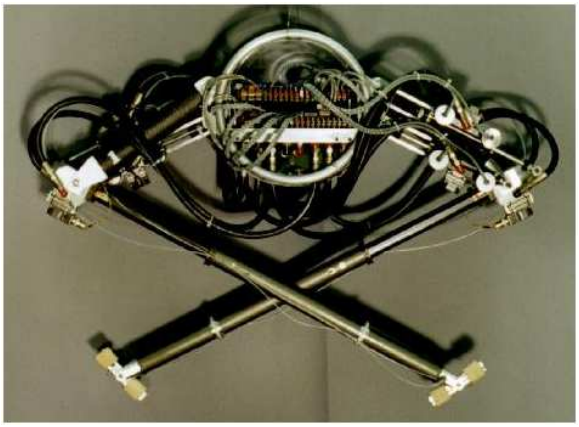

Figure 2.18 MIT's Planar Quadruped Robot with Articulated Spine

Figure 2.19 Whegs: Production-ready Robot from Roger Quinn's Group

of robot (serpentine) is the way in which the spine moves. In this case, a wave travels down the length of the robot, whereas in most mammalian systems, the entire spine is active in extension or flexion. The legs are passive and assist in the transition between gaits.

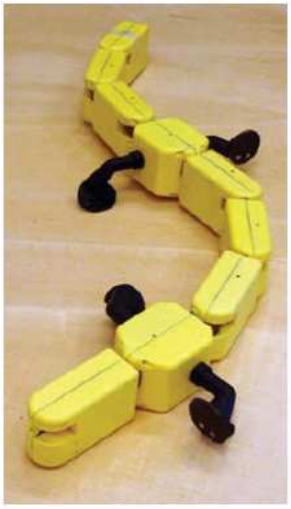

Figure 2.20 Salamander Robot

Along with the aforementioned Big Dog, Boston Dynamics' latest project is the construction of a biomimetic cheetah-inspired robot. The initial prototype will be developed over a 20 month period with an initial speed goal of 30 mph. The company says their

purpose in developing the robot will not necessarily be for field deployment, but rather to explore the possibilities of a high-speed quadruped robot. The project is funded by DARPA and the initial model is presented in Fig. 2.21. Another similar project from the Biomimetic Laboratory at MIT was discussed in 2009 and featured a lightweight, high-speed articulating quadruped robot (Fig. 2.22).

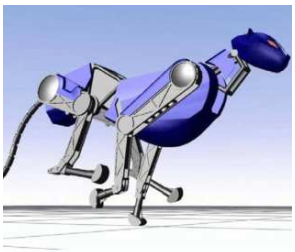

Figure 2.21 Boston Dynamics' Cheetah Robot

Figure 2.22 MIT's Cheetah Robot

In general, the overall motivation for the articulation in the robots is to mimic nature. The majority of these robots focused on developing controllers (most used a CPG or reinforcement learning technique) to enable a stable gait. These are still very relevant problems, however as technology moves forward, it is important to move forward in thinking. Big Dog has captured the public's eye with its eerie movements and astounding response to an intense perturbation (a kick from the side), but imagine it now with a flexible spine, moving like a cheetah, sprinting when needed and walking at other times. With the MIT and Boston Dynamics' cheetah robots in production, this future is not far off.

Modeling and simulation are the first steps to the creation of a successful prototype. The next section focuses on the models available, some of which were used to create the physical prototypes mentioned above. Most of the articulating robots, the exception being Leeser's at 3.6 m/s, were operated at low speeds. The goal of high speed locomotion may not be obtained with a rigid back. Understanding how articulation was incorporated in the past, lends insight to its integration in future systems.

2.2 Existing Models

Many of the physical robots were built upon principles guided by the researchers' work done in modeling and simulation prior to construction. The following section describes various analytical and computational models used to create the physical prototypes mentioned in the previous section and other models used to test various hypotheses. The models described below cover a large range of work divided into the following categories: computational and analytical models, operating speeds and implemented gaits, rigid and articulated modes, and lastly, the model application. The goal of this section is to provide the reader with an idea of the depth of the modeling work in this area, show the limitations of the available models, and where the current model addresses this deficiency. As such, the models will be addressed individually and their contribution to the critical aspects of the current work discussed.

2.2.1 Gaiting

Before the models found in describing literature and their relevance, general terminology for gaits [(7),(62)] is reviewed to provide background information, specifically within the context of high speed.

Gaiting is the coordinated movement of an animals' limbs in its simplest form or as described by Alexander (9),

Gait A gait is a pattern of locomotion characteristic of a limited range of speeds described by quantities of which one or more change discontinuously at transitions to other gaits.

For quadrupeds, the general selection of gaits from low to high speed progresses from symmetric gaits (walk and trot) to asymmetrical gaits (bound and gallop). Most cursorial animals exhibit these gaits depending on their operation speed. Symmetric gaits have paired footfalls equally spaced in time. During walking, the articulation in the back is demonstrably rigid and does not affect the gait in nominal ways. There are no flight phases during the walking gait and the paired legs are on the left and right sides of the body. The gait used at moderate speeds, trot, pairs cross-body limbs. Intermediate gaits exist between these but most work focuses on these two gaits in the low to moderate speed range. Two additional terms useful when discussing gait are *stride frequency*, the number of steps per unit time strides/s or s^{-1} and *duty factor*, the ratio of the time spent in stance over the total time.

The gallop is a gait used at high-speeds, with unequal footfalls. Since the system modeled in this work uses a planar model, the gallop is approximated by the bound gait. Both are considered asymmetric, however, the bound can be simplified by pairing the fore and hind legs. It is during these high-speed gaits, where the motion of the spine is most prominent. As with the lower speeds, variations exist; however, these are the high-speed gaits most often discussed.

Although observed only in rare cases in animals such as mule-deer and mountain goats, the in-phase gait known as pronk is often used in quadrupedal modeling. All four feet leave the ground simultaneously, causing the body to leap. There is no torso rotation, reducing modeling complications. Several models discussed here employ this gait.

Animals choose gaits within a range of speed to minimize energy (64). As animals transition from low to high speed, a non-dimensional value known as the Froude number reasonably predicts the transitions between gaits (7). The Froude number is an approximation for the ratio of the kinetic and potential energies of the system and is given in Eqn. 2.1.

$$F = \frac{v^2}{gl} \tag{2.1}$$

Here, v is the velocity of locomotion, g is gravity, and l is a characteristic length (usually the height of the hip joint from the ground). One reason for the energetic attractiveness of the gallop at high speeds is that the peak gravitational potential energy is very nearly in phase with the peak kinetic energy (29). A smaller variation in vertical height of the center of mass is also observed in galloping. In general, animals transition from walking to running gaits when the Froude number is between 2 and 3.

As shown in the work by Hoyt and Taylor, there is an energetically optimal gait for a range of speeds. One of the reasons, conjectured for the decrease in metabolic energy consumption at high speed with a gallop (64), is based on the number of legs in the return phase at any given time. The larger the number of legs in return (averaged over the stride cycle), the faster the speed. Song and Waldron (139) proved this for statically stable locomotion. The work of Gambaryan and Hardin (44) stated that the time taken to return a leg to its starting position is relatively constant; however, at higher speeds, there are mechanisms that allow an animal to have higher leg cycling frequencies. Two main ideas hypothesized are:

- When animals run fast, they fold the legs in as close to the hip/shoulder. This decreases the moment of inertia of the leg about the joint, increasing the natural frequency of oscillation (like a pendulum that has the string shortened).
- Elastic energy storage in the muscles act to rotate the leg forward or back about the hip/shoulder (like a torsional spring) and also increases the natural frequency of the

pendular motion.

Therefore, the coordinated movement of the segmented legs and spine, in conjunction with elastic energy storage mechanisms acting like springs, allow for greater stride frequencies. Stride frequency is one way to increase the system's speed but changes little in the preferred speed range (acting mostly at the transitions and lower speed). At high-speed, the system relies on the extension of the limbs and back to go beyond this, as suggested by Hildebrand's work (54).

Now that some of the definitions pertaining to gait are defined, the models and their applicability to the current work are discussed. With an energetic minima at high-speed using the gallop gait, models displaying these characteristics are the most pertinent.

2.2.2 Models

There are a variety of quadruped models and those presented here are organized based on the following characteristics:

Model Execution This topic refers to how the model is executed- is an existing simulation program used or did the work use analytical expressions to derive its results.

Speed / Gait The models are implemented at a range of speeds with one or more gaiting methodologies employed. High-speed models with bounding or gallop gaits are keenly inspected.

Torso Construction The focus of the work employs an articulating node in the torso. Most models use a rigid implementation. Rigid models provide the baseline against which the articulation is compared.

Model Implementation This classification refers to how the model is utilized- is its primary purpose as a skeleton for a controller, stability studies, or some other purpose. Any other metrics and their application to the work are addressed.

One of the seminal works in quadruped models is the work of Raibert (120). The model is analytic with a rigid torso. Its primary function was to provide an architecture for a controller, tested on a physical prototype. The top speed was 3 m/s (2.86 bodylengths/s). In addition to the actual robot, an important contribution of this work is the introduction of the virtual leg concept. This idea allows two separate legs to be represented by a single 'virtual leg'. The control is decomposed into three separate parts regulating the body's:

1. **Hopping Height**- Controlled by the leg thrust during the stance phase.
2. **Forward Running Speed**- Position feet during the flight phase to influence acceleration of the body during the next stance phase.
3. **Body Attitude**- Exert torques about hip during stance to keep body level.

These low level controls enabled trotting, pacing and bounding gaits for a rigid-legged, four-legged robot with only slight parameter variations in the model. The controller was demonstrated to display the various gaits on a tethered prototype with axially actuated legs and hip torques. Raibert's other work continued to enrich the modeling and implementation of quadruped controllers (121), with his current work centering around BigDog and the future Cheetah robot at Boston Dynamics.

Leeser's work builds off Raibert's original hopper research [(117), (118)] and the concept of a virtual monopod. The system is planar and composed of three segments with actuated joints. The controller is based on a three part methodology: control of the forward running speed, hopping height and body attitude. The results of the work show that the back can be used to augment the thrust provided by the legs. The back also effectively modulates the energy state of the leg spring. The work suggests that the flexible back can be used to modify the damping characteristics of the legs in the system. Leeser's computational model was used primarily for testing the controller and was built with dynamic modeling software called the Creature Library. The highest speed run at was 3.6 m/s, or 3.7 bodylengths/s with the total back measuring 0.98 m.

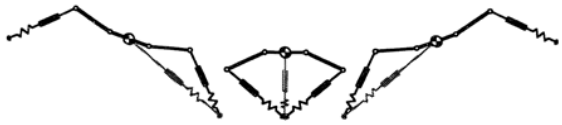

Figure 2.23 Leeser's Planar Quadruped Model

In the most basic sense, an articulating model can be constructed as shown in Fig. 2.24 taken from Alexander's paper (13). This simplified model has rigid legs and is planar. The front legs move together, as do the back legs. The trunk is constructed of two symmetric rigid sections hinged together for the articulated model and a single solid trunk for the rigid one. The purpose of this analysis was to look at a simplified system and compare the energy cost in the galloping versus rigid-backed model. The results of the analysis showed that the only difference between the two models was the kinetic energy due to the internal motion of the hinged bodies with respect to each other in the articulated model. All other system energies were consistent between the two models when comparing the models at the same speed, gait and ground force profiles. The results are intuitive, although do not corroborate with the experimental data (as demonstrated in (64)). During galloping, internal energy does increase in flexible-spined animals, but it would seem that the elastic strain

energy storage / transfer provided by the back muscles, balance or mitigate this increase in internal energy. This simple model does not take this into account.

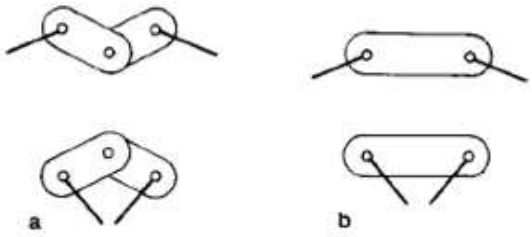

Figure 2.24 Alexander's 'Why Mammals Gallop' Model

Another important contributor to quadrupedal models is P. Nanua. His work on quadrupedal galloping [(98), (99), (100)] linked stride frequency, initial compression of the models' springy legs (linked to internal energy) and speed. The model is a rigid bar that has four compliant legs: two legs connected to a pin in the front and two connected via a pin in the rear. Each leg is modeled as a constant stiffness, massless spring [(98), (100)], with one model including the addition of a viscous damper and force actuator in parallel (99). For these systems, Nanua uses two free variables, u (horizontal speed) and E (total energy of the system), to describe the system. The focus of the work was to generate a control scheme to enable a stable gait for a given energy level and speed. The gaits investigated were the trot, bound and gallop. The speeds investigated were 2.78, 4.17, 6.94 and 11.11 m/s with stride frequencies of 1.25, 1.67, 2, 2.08 s^{-1}, respectively.

One of the simulations in (98) incorporates a torsional spring into the model. The spring operates between the two halves of an articulated back. The leg springs are initially compressed and the body set at a constant speed (11.11 m/s, 4.13 s^{-1}). The initial angular velocity of the back segments is set to zero and the back angles are symmetric, $\theta_{1,i} = \theta_{2,i}, \theta_{1,i} = 4.75^{\circ}$. The initial compression and stiffness are varied to search for a stable solution, which the author was unable to find based on the conditions specified.

The model demonstrated in the work by Nanua and Waldron (100) is a 2D model with a rigid beam. Two massless spring legs are attached in the front and back. For a periodic solution to the trot system, two initial conditions y_i and u_i are selected, where y_i is the initial vertical displacement and u_i is the initial horizontal speed. In order to find a unique solution, experimental data was used to fix y_i at a given speed. A 680 kg horse with a leg length of 1.5 m and a non-dimensionalized spring stiffness $K_{leg} = 14$ was used to set the stride frequency at 100 min^{-1} for a speed of 15 mph (from (55)).

The first set of experiments look at running each model at a fixed speed (2.78, 4.17, 6.94 and 11.11 m/s) with the same energy level obtained by running the trot at 2.78 and 4.17 m/s and the gallop at 6.94 and 11.11 m/s. At trotting speeds, stride frequency of the

trot has the least energy requirement, and at gallop speeds, stride frequency of the gallop has the least.

The second experiment forced the simulations to follow the speed-stride frequency curve of Heglund. The energy levels were calculated and plotted against speeds. They also did the experiments using a dog with a similar procedure. Their conclusion stated, even without back flexion, choosing an appropriate gait for a particular speed had an energetic advantage.

Another set of models, based on horses, is provided by Herr. His work [(58),(59)] describes a ten DoF model, with two DoF per leg, one back joint and one neck joint. The mass is distributed in a realistic manner based on morphological data. The foot is modeled as a point contact with the compliant ground (modeled using springs and dampers so slip on initial contact does not occur). Ideal linear springs are used to simulate the limb, back and neck behavior during stance. The controller does a number of things during the stance and aerial phases, but generally comes down to regulating thrusting / braking torques at the shoulder and knees to maintain a system galloping at constant speed. The results reasonably predict a horse trotting and galloping when compared to experimental data. With the use of the morphological data as driving parameters for the system, postural stability is an emergent system characteristic. Unique to this model is the non-symmetric placement of the back articulation. The simulation is run at 5.2, 6.8, and 7.4 m/s. The torso length is estimated (48) to be 0.97 m, assuming a mass of 140 kg, resulting in speeds of 5.36, 7.01 and 7.63 bodylengths/s.

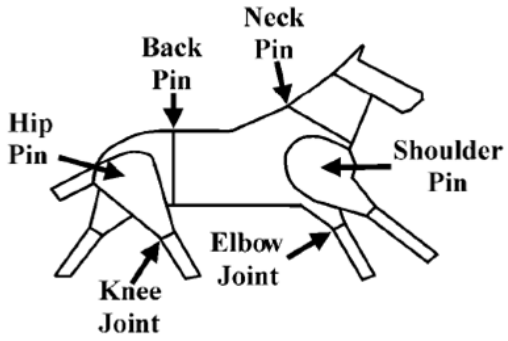

Figure 2.25 Herr's Galloping Horse Model

The next model of interest is from Berkemeier's work (18) and Neishtadt and Li's (101). The model observed the stability properties of a quadruped running in place (no forward velocity). The body is a rigid, two degree of freedom model with two massless legs consisting of a spring, damper and position-controlled actuator. The main difference between the two models is Berkemeier includes gravity in the formulation of the equations of motion. The angular speed of the torso ranged from 1.5 rads/s to 10 rads/s. Two periodic solutions

were obtained, corresponding to the bound and pronk gaits. The bound was stable, provided the dimensionless body inertia was less than one. The pronk's stability is related to height and inertia. The major contribution of the study displayed how body inertia is a critical design parameter.

Schmiedeler's model [(130), (132)] uses a five DoF model with a rigid trunk and massless legs. The work gives a mathematical explanation for the gait changes in the quadruped model, as related to the effective drag of the system. In this case, the effective drag is the component force of gravity acting transversely on the body as it is moving uphill. The conclusion of the work shows animals select in-phase gaits with large stride periods as drag increases because it allows the legs to be positioned properly relative to the trunk for efficiently generating thrust. The gallop and its variations are featured in (132), but (130) describes the range of gaits from walk to gallop, as well as the many different gaits in between. The 33 kg model with a torso length of 0.6 m was investigated at 2.37 to 5.14 m/s (3.95 to 8.57 bodylengths/s). The main goal of (130) was to design a compliant leg for a prototype galloping quadruped robot based on the effective leg stiffness determined by the previous gaiting studies.

The work presented by Zou and Schmiedeler in (152) demonstrates bounding with a model similar to Berkemeier's. The model runs in place and is planar with massless legs, incorporating a spring and damper in parallel. The primary difference between the models is the asymmetric placement of the center of mass on the rigid torso. The model is passively stable when the dimensionless moment of inertia of the body is less than $1-\beta^2$, where β is a dimensionless measure of the asymmetry. The model runs in place but has a center of mass that is weighted more towards the front legs, presenting a more biologically realistic mass distribution. The primary purpose of the model is to analyze how the center of mass placement affects the stability and dynamics of a simple quadruped model.

Schmiedeler et al. 's work in 2001 (131) presents a study on a simulated galloping gait from a biological perspective, followed by the implementation on a prototype to test the results. The model consists of four legs: each leg consists of an upper and lower mass. There is a torque at the hip actuating the upper leg mass and linear actuator in series with a spring / damper combination actuating the lower leg mass. A direct adaptive fuzzy controller is used to control the speed and height. The inputs to the controller are the state at top of flight and those desired at the next top of flight. Therefore, the height, velocity, pitch and pitch rate are the inputs with the outputs being the leg touchdown angles and leg thrusts. The proof of concept is in a single leg design followed by later work in (103), presenting the entire design of the robotic system.

The next set of models are related to a five DoF system and were used in tandem with the Scout II robot to develop stable running gaits.

Poulakakis et al. presented an analytical model used for the analysis of the Scout II robot (115). The model is composed of three bodies- two legs and one torso. A linear spring/damper system models the leg compliance during the stance phase. Initially, the model was employed with simplified conditions to demonstrate stable bounding gaits up to speeds of 1.3 m/s (for the torso length of 0.55 m, 2.36 bodylengths/s). Their second goal was to experimentally validate the model; therefore, additional complexity relevant to the robotic system, including models for the motor driving the system, the battery, amplifier, actuator and gearbox units, were added to improve the correlation between the physical robot and the model. The model was also used to implement and test a simple controller based on methodology similar to Raibert's in (120) and was unique in its open loop leg positioning control law

Other research done by Poulakakis et al. [(114), (116)] focused on identifying the conditions necessary for the generation of passive running cycles and studying their stability properties. The work uses the self-stabilization properties in the spring-loaded inverted pendulum (SLIP) in order to aid in their search. Their work demonstrated globally fixed points at higher speeds require flatter touchdown angles (119). The paper presents studies on convergent forward speeds and subsequent investigations on those speeds' relation to the touchdown angle. From these observations, two feasible variations on the bounding gait were shown mathematically, as well as experimentally observed on the Scout II quadruped robot. These correspond to the front leg moving away from the body (inner branch) or towards the body (outer branch). In each of these gait variations there exists a stable region where the model does not need control. The work emphasizes the notion of self-stabilization as an aid in the design of simple and robust controllers for complex motions like bound.

The SLIP model was studied by Cavagna et al. (29) and others [(22), (38), (63), (77)] as a simple way to describe fast locomotion in animals. The inverted pendulum description of walking was also investigated. Both of these models describe behaviors observed via a series of experiments where humans and animals walked, hopped, trotted or ran across a force platform. Blickhan further studied the behavior (22) with a massless spring connected to a point mass, while Mochon and McMahon extended the inverted pendulum concept to ballistic walking (95). From the SLIP model observations, a necessary and sufficient condition for the existence of fixed points is a symmetric stance phase- the liftoff angle is equal to the negative of the touchdown angle. Speeds investigated in the single point mass connected to a massless spring ranged from 5.5 to 7.0 m/s.

The model presented by Hyon et al. in (65) has a rigid torso with springy telescopic legs rotating about the torso with hip springs. Their legs have mass, but no knees, and all springs are linear. The results showed two types of gait (including a stance and flight phase), neither of which were passively stable for the quadruped model. A simple controller was used to stabilize the bound gait. The speed for simulations was set at 2 m/s (4 bodylengths/s).

Silva's model (135) is constructed with *n*-legs (equally distributed on both sides of the body) with two degrees of freedom per leg (hip and knee). The trunk of the system is divided into *n*-segments and a linear spring-dashpot system is adopted for the intra-body compliance. The foot-ground interaction of the model is handled by two methodologies-exact force-deflection relationships or approximate models of ground deformation based on soil mechanics. The controller for the system utilizes a fractional order and proportional controller for the gait planning. Their results showed that the system response was reasonable for a hexapod configuration. Subsequent studies characterized additional metrics such as gait efficiency (136) and system stability (137).

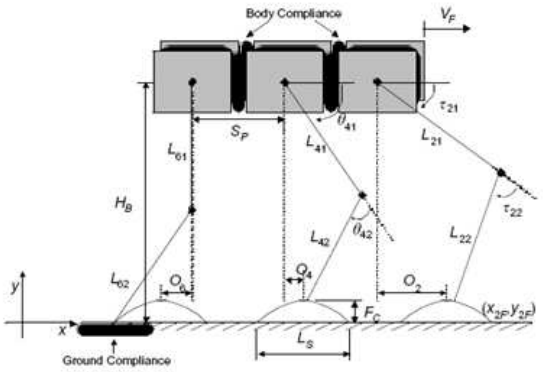

Figure 2.26 Silva's Multi-Legged Compliant Model

The last major group of models of relevance for this research are variations on the Formal'sky et al. work from (39), used as the template for the baseline model of the current research. More detail on the model will be addressed in the next section but is briefly given here for completeness.

Formal'sky et al. present a rigid model with knees (39). The legs and rigid torso have mass and the system ballistically traverses from one stance phase to the next through the use of fixed points. There is no flight phase in the model; however, the use of passive-dynamic step phases with impulsive transitions and construction of fixed points to set a cyclic gait are the crux of the model created herein. The speeds investigated are 1.5 to 4.0 bodylengths/s.

Muraro et al. (97) followed up on the work of Formal'sky (39) by seeking optimal cyclic reference trajectories based on including actuator characteristics in the model. The actu-

ated joint evolution is chosen as a polynomial function of time with the coefficients as the optimization parameters. The costs used for the optimization are torque cost (integral of the torque norm) and energetic cost (absolute value of the integral of work done by external forces). Both are calculated for a fixed displacement of one meter. Their studies show that the bound is the least efficient gait at slow speeds, with the trot showing the best results (the speed varied from 0.1 to 1.3 m/s, 0.27 to 3.58 bodylengths/s). The walk permits the fastest motion with the same actuators.

Work by Aoustin et al. in (15) used the model from (97) to test a control strategy on a robotic platform called SemiQuad (Fig. 2.14). The control strategy uses the previously determined passive trajectories as reference for the actuators at the hips / knees. During the single support phase, reference trajectories are computed for three of the joint angles as polynomials, and a proportional derivate controller is used to track these preset paths. The speeds for the simulations and experiments ranged from 0.0125 to 0.0133 m/s (0.03 to 0.04 bodylengths/s).

Another group used a similar model to (39) but included a flight phase. Furusho et al. (43) used the model to create a control strategy using three modes: position control mode, velocity control mode and free rotation mode. The robot was able to use the controller in combination with its sensors and actuators to realize the bound gait (noted as bounce in the paper). The simulations and trials were run at 2 m/s (2.86 bodylengths/s) and employed on the physical robot Scamper.

Model (Primary Author)	Max Speed Investigated (bodylengths/s)
Poulakakis	2.36
Raibert	2.86
Furusho	2.86
Muraro	3.58
Leeser	3.70
Hyon	4.00
Formal'sky	4.00
Nanua	7.41
Herr	7.63
Schmiedeler	8.57

Table 2.1 Max Speeds of Quadruped Models

The models presented here cover the key research done in the area of quadrupedal modeling. Table (2.1) lists the max speeds for which quadruped models have been investigated. Although there are some models that operate at high speeds with a rigid back (Nanua, Herr and Schmiedeler), there are no analytical models that quantify the energetic consequences of employing an articulation at high speed. The work presented here fills this void by devel-

oping and analyzing a high-speed, bounding articulated model (running at speeds of 10.0 to 15.0 bodylengths/s) compared to a similar system with a rigid back. The construction of these models, and their subsequent analysis, are presented in the following chapters.

Chapter 3
Model Description

This chapter presents the development of the rigid and articulated quadruped models, including all assumptions, bounds and constraints. Various local and global optimization methods were employed, first to find admissible gaits and second, to minimize the energetic cost within the biological constraints supplied. A pseudo-code diagram can be found in Appendix A for visual reference.

The methodology, associated constraints and objective functions used to obtain admissible and optimized gaits are described. With an understanding of the model development, its limitations and assumptions, the subsequent results of the simulations conducted for optimization, presented in the next chapter, are justified and given the necessary background to present a meaningful analysis.

3.1 Dynamics

The equations of motion of the system, including initial conditions, constraints and assumptions, determine the dynamics of the system. General aspects of both models are discussed (gaiting, virtual leg, impulsive transitions, equations of motion, constraints), followed by individual discussions on the rigid and articulated models.

3.1.1 Gaiting

A gait is defined as the timing and sequencing of an animals' legs as it moves from one place to another. From Hoyt and Taylor's work (64), an energetic minimum exists at an animals' naturally selected gait within a speed range. For high-speed, the gallop is the chosen gait. Using the cheetah as the biological archetype, the gallop is deconstructed into various phases. Hildebrand's work (61) provides a visual breakdown of the cheetah's stride and is shown in Fig. 3.1.

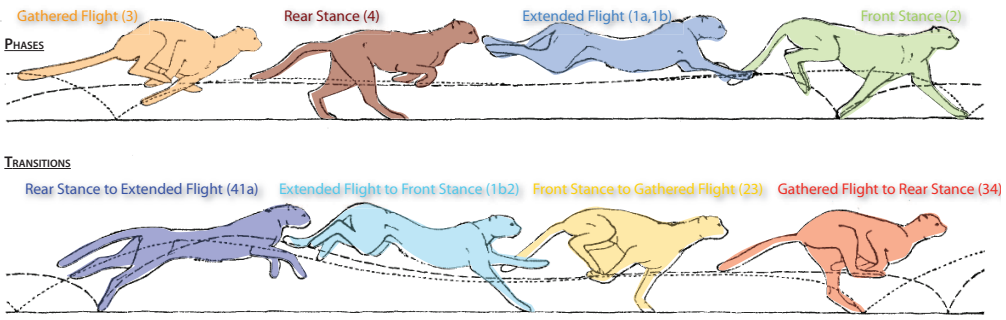

Figure 3.1 Hildebrand's (61) cheetah stride images

The top and bottom portions of the image are divided into the phases (top half of the image) and the transitions (bottom half of the image). The top left position of Fig. 3.1 shows the cheetah in the gathered flight phase, where the feet are tucked under the body. The next image to the right, shows the start of the rear stance phase leading up to the launch phase (this phase is the power stance phase). Following the launch phase is the extended flight phase. During this phase, the body is stretched out to its full extents. After the extended flight phase, the front stance phase begins. This phase has a double step out that helps to minimize the energy at impact (127) and is the braking stance phase. From these descriptions, the system is broken down into four primary phases, beginning with the start of the launch phase, referred to as rear stance:

- ***4***: System is in rear stance and is preparing for take-off.
- ***1a,1b***: The system is in flight and fully extended.
- ***2***: The rear legs move forward in preparation for the next phase.
- ***3***: The rear legs cross over the front in order to position the rear legs under the body while the body is in flight.

One full cycle is taken to be the system at the top of the extended flight phase, to the next consecutive top of the extended flight phase. The extended flight phase is denoted by the alphanumeric labels of *1a, 1b* from the definition of the full gait cycle. The first portion, *1a* is the ascending part of the trajectory, while *1b* is the descending part of the trajectory. The split in the extended flight phase is necessary to provide an additional impulsive transition. More details are provided in the next section.

3.1.2 Impulsive Transitions

The bottom half of Fig. 3.1 shows the transitions, which represent the change between the phases. The first image shows the transition from the rear stance phase to the extended

flight phase- the animal is launching into the air and entering the extended flight phase. The next transition occurs between the extended flight phase and the front stance phase. The last transition is between the gathered flight phase and the rear stance phase. An additional transition for modeling purposes occurs at the midpoint of the extended flight phase. This transition is necessary to bring the legs back underneath the body in preparation for the front stance phase. Without active torques during the flight phases, the system needs a mechanism to reverse the direction of the legs and a mid-flight impulsive transition fulfills that task. The impulsive transitions are denoted by the following alphanumeric labels:

- ***41a***: Transition from the rear stance phase to the first half of the extended flight phase.
- ***1a1b***: Transition at mid-flight of the extended flight phase.
- ***1b2***: Transition from the second half of the extended flight phase to the front stance phase.
- ***23***: Transition from the front stance phase to the gathered flight phase.
- ***34***: Transition from the gathered flight phase to the rear stance phase.

Leveraging the work of Mochon and McMahon (95), the model uses ballistic trajectories during the flight phases. This implies that, given an initial set of positions and velocities, the system moves through a time t from point A to point B with the only force applied due to gravity. Since the system moves across a flat, level surface, the energy lost at impact with the ground needs to be replaced to maintain a cyclic gait. A cyclic gait is one in which the system, starting at a set a of positions of velocities, returns to the same set of positions and velocities at the end of one complete stride. Energy can be injected into the system through the actuation of the joints either continuously (active torques and forces) or as a 'whack' to the system (impulsive torques and forces). Both types are used in the models developed for this research. At the above noted transitions, instantaneous impulsive forces and torques can be applied to transition the system from the end velocity state of the prior phase (*before impulse*) to the desired initial velocity state at the start of the next phase (*after impulse*). Using instantaneous impulsive actuations has been shown to be a valid approximation for phase transitions (2) and is a common technique employed for injecting energy into ballistic systems [(39),(81),(130)].

The phases and transitions of the cheetah gallop were mapped to the models used here, as shown in Fig. 3.2, using the rigid model as the example system, recognizing that the articulated model follows the same gait phases and transitions.

The various forces and torques applied during the impulsive transitions are shown in Fig. 3.3 for example front stance, rear stance and flight phases. For the rear stance, only the rear foot can have an impulsive force and ankle torque, while for the front stance, the converse is true (the front foot has the impulsive force and ankle torque). The mid-flight

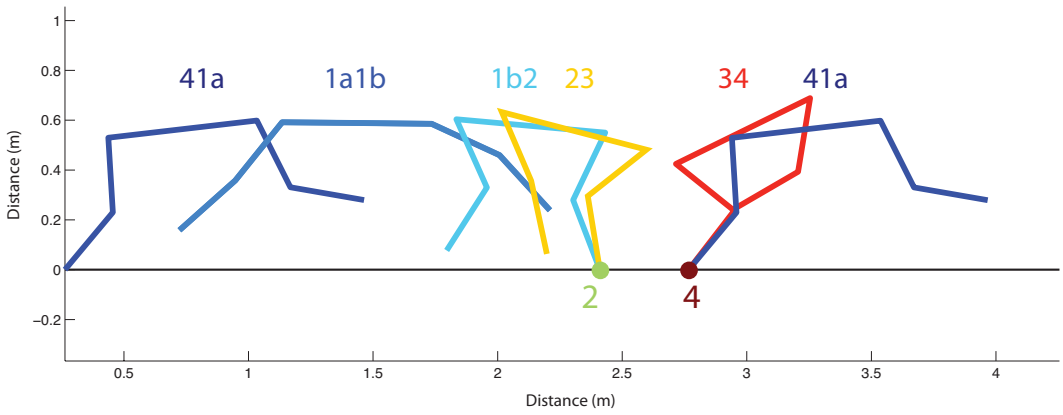

Figure 3.2 Phase transitions and stance phases over the duration of the entire gait

impulsive transition has no impulsive forces or ankle torques.

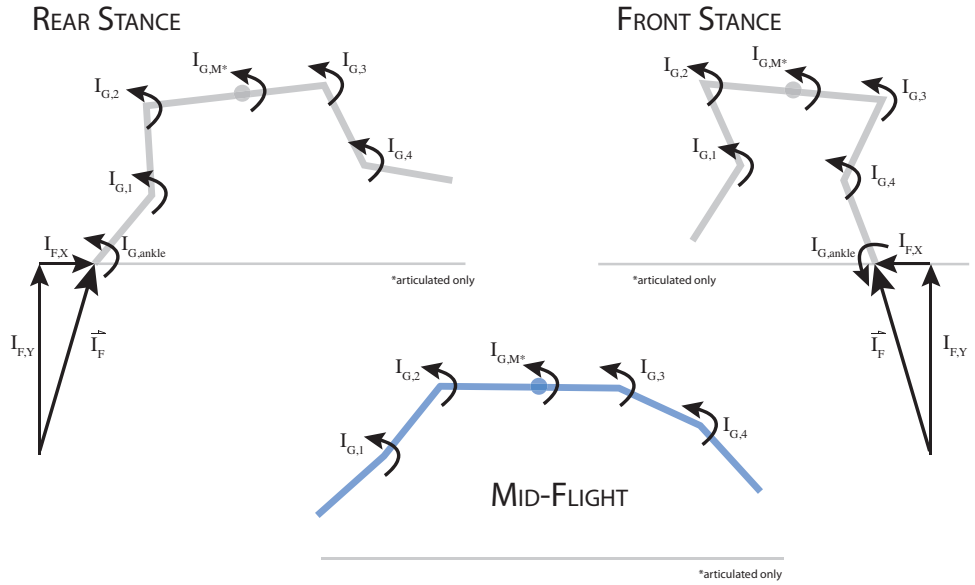

Figure 3.3 Impulsive forces and torques at the phase transitions

3.1.3 Virtual Leg Simplification

Although the inspiration for this research, the cheetah, is a quadruped, a simplification involving coupled pairs of legs can be effectively used to describe an approximation of the gait. The four jointed legs of the system are combined into two coupled pairs using the virtual leg construct. The virtual leg construct was introduced by Marc Raibert (122) to simplify the control and dynamics of a multi-legged system. The premise of the virtual leg

stems from observations on animal gaiting behavior. When an animal selects an in-phase gait (also known as a symmetric gait), studies of the gait patterns show limbs moving together in distinct couplings. When the limbs act in unison, they can be combined into a single virtual leg, thereby simplifying the construction of the model from a four-legged system into a two-legged one.

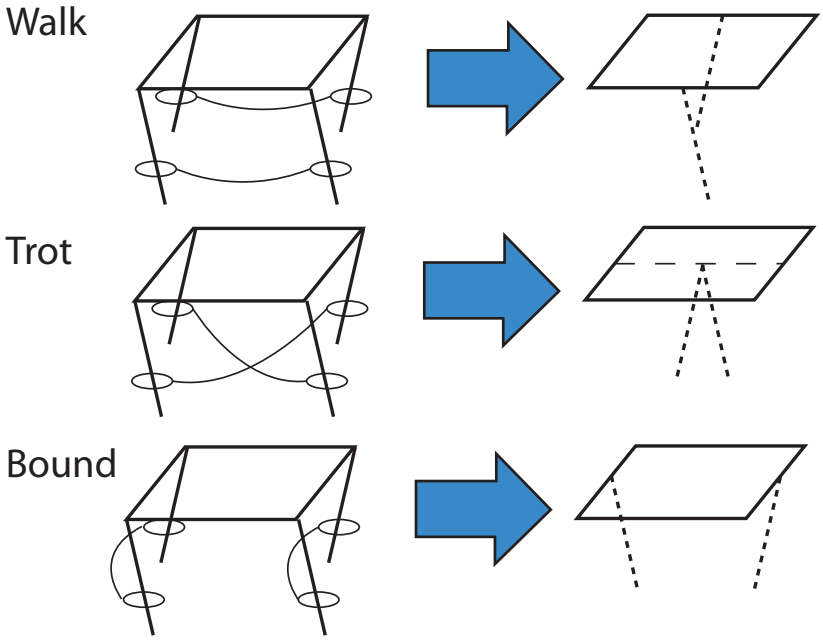

Figure 3.4 Virtual leg coupling for the walk, trot and bound

With the virtual leg construct, the gaits are defined using the pairs shown in Fig. 3.4: the walk couples the limbs on either side of the sagittal plane (the left fore-hind limbs and the right fore-hind limbs), the trot couples the left fore-limb / right hind-limb together and the right fore-limb and left hind-limb, and the bound couples the limbs on either side of the transverse plane- the fore limbs and the hind limbs. Fig. 3.5 describes the planes used to couple the limbs.

At high speeds, the bound is a simplification of the rotary gallop, the typical running gait of the cheetah and greyhound. Most of the phases listed in Sect. 3.1.1 are approximated well by the virtual leg simplification (additional evidence is provided in Sect. 3.1.8.1), with the exception of the front step-out. Condensing the step-out motion to a single front stance phase increases the energy lost at collision (127) and the time spent in stance. The biological approximation of this simplification is a front leg amputee quadruped gallop. Despite its limitation of a single foreleg, such an animal is able to achieve fast running speeds (*www.tripawds.com*), providing some biological feasibility to the simplification of the front step-out.

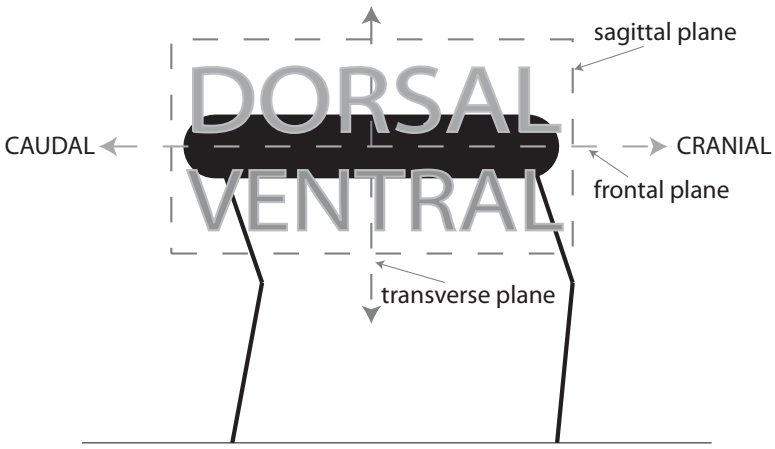

Figure 3.5 Description of reference planes

3.1.4 Equations of Motion

The general form of the equations of motion defining the overall dynamics of both systems is given in Eqn. 3.1.

$$A(\vec{q})\ddot{\vec{q}} + B(\vec{q},\dot{\vec{q}}) = D_G(\vec{q})G + D_1(\vec{q})F_1 + D_2(\vec{q})F_2 \tag{3.1}$$

$$A(\vec{q})\ddot{\vec{q}} + B(\vec{q},\dot{\vec{q}}) = D_G(\vec{q})G + D_1(\vec{q})F_1 \tag{3.2}$$

$$A(\vec{q})\ddot{\vec{q}} + B(\vec{q},\dot{\vec{q}}) = D_G(\vec{q})G + D_2(\vec{q})F_2 \tag{3.3}$$

$$A(\vec{q})\ddot{\vec{q}} + B(\vec{q},\dot{\vec{q}}) = 0 \tag{3.4}$$

Here, A represents the mass matrix and B contains all of the centrifugal, Coriolis and gravity terms on the left-hand side. The D's on the right-hand side are the coefficient matrices for the (impulsive) forces and torques, where the subscript 1 applies to the rear foot and subscript 2, to the front foot. The state variables (represented by q) are the seven (rigid model) or eight (articulated model) independent measures used to define the location and orientation of the planar system. The G's are the (impulsive) torques and F_1 is the (impulsive) force on the rear foot and F_2 is the (impulsive) force on the front foot.

3.1.5 Rigid Mode: Description and Verification

The rigid model is based on the work of Formal'sky, Chevallereau and Perrin, (39). A brief description of the work conducted in (39) is recounted here to provide a foundation for the rigid model. The general model parameters are given in Table 3.1.

These dimensions and masses are similar to those of a medium-sized dog and are about

Model Parameter	Variable	Value
Lower / upper leg masses	m_1, m_2	2.25 kg
Torso mass	m_3	15 kg
Lower / upper leg lengths	l_1, l_2	0.3 m
Torso length	l_3	0.6 m
Lower / upper leg inertias	I_{l1}, I_{l2}	0.0173 $kg \cdot m^2$
Torso inertia	I_{l3}	0.4625 $kg \cdot m^2$

Table 3.1 Rigid model parameters from (39)

half the dimensions and a third of the mass of the BigDog robot.

Formal'sky (39) used two phases to construct the various gaits- front stance and rear stance with an instantaneous double support transition. The first phase is in rear stance (starting at time $t = 0$ and ending at time $t = T$) and the second phase is in front stance. The phases are linked by an instantaneous double support (starting at time $t = T$ and ending at time $t = 2T$). Bounding at low speed was one of the gaits simulated (1.2 - 2.1 m/s or 2 - 3 bodylengths/s).

As depicted in Fig. (3.6), $q = [x, z, \theta, \alpha_1, \alpha_2, \alpha_3, \alpha_4]$ is the state variable vector, where x and z are the respective horizontal and vertical positions of the center of the torso, θ is the angle of the torso with respect to the horizontal axis, α_1 is the angle of the bottom half of the hind leg with respect to the top portion of the leg, α_2 is the angle of the top half of the hind leg with respect to the perpendicular of the torso, α_3 is the angle of the top half of the fore leg with respect to the perpendicular of the torso, and α_4 is the angle of the bottom half of the fore leg with respect to the top portion of the leg. For this system, clockwise is positive for rotations, with x positive moving from left to right on the page and z positive moving from bottom to top on the page.

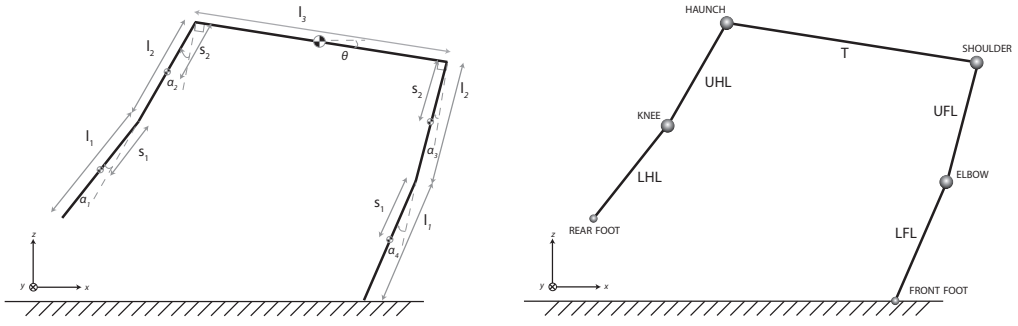

Figure 3.6 Rigid model generalized coordinate description

The equations of motion were symbolically generated using Mathematica and the resultant expressions were transferred into MATLAB to solve for the forward dynamics. The equations of motion were solved numerically using the ODE45 integrator with the initial

positions as specified in Table 3.2, the initial velocities set by the fixed point analysis (Sect. 3.2.1) and an event function which stopped the integration routine if foot/ground contact occurred.

Variable	t = 0	t = T	t = 2T
θ	0°	0°	0°
α_1	-10°	$-\alpha_2(0)$	-10°
α_2	-20°	$-\alpha_1(0)$	-20°
α_3	$-\alpha 1(0)$	$-\alpha 1(T)$	$-\alpha 1(0)$
α_4	$-\alpha_2(0)$	$-\alpha 2(T)$	$-\alpha_2(0)$

Table 3.2 Rigid model test case initial conditions

The resultant ground reaction force time histories for the bound gait at 1.2 m/s are provided in Fig. 3.7. The force follows trends of low-speed, inverted pendulum system - an inverted parabola that peaks as the system vaults over the planted foot.

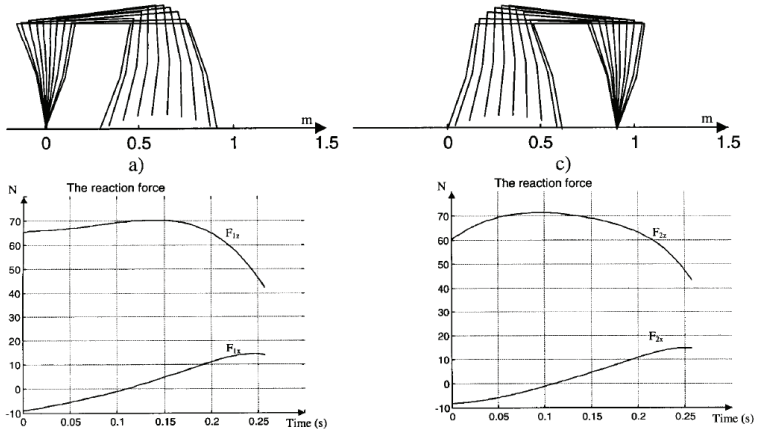

Figure 3.7 Formal'sky (39) force results for the bound at 1.2 m/s

The model was verified using MSC.ADAMS, a commercial, general purpose multi-body dynamics software package. The model is constructed based on the given parameters (moments of inertia, masses, and initial body translational and angular velocities). See Appendix C for information on the ADAMS model construction process. Results from the 1.2 m/s simulations are shown in Figs. 3.8 and 3.9. Agreement between the two models was observed at all speeds investigated.

3.1.6 Articulated Model: Description and Verification

The articulated model is the same as the rigid model of the previous section, except for the addition of a single node of articulation in the torso. This node, placed at the midpoint, divides the torso into two equal length, equal mass bodies. The articulated model parameters

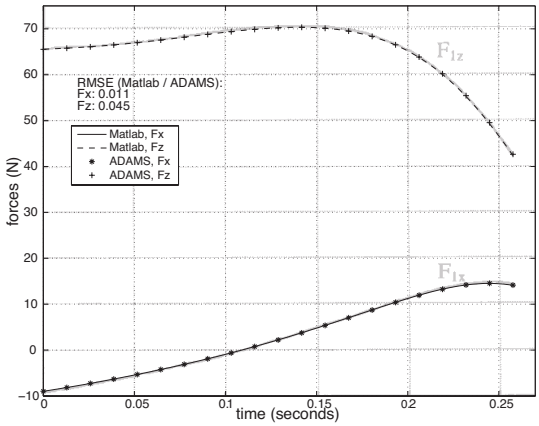

Figure 3.8 Comparison of rigid model results using MATLAB and ADAMS for rear stance, 1.2 m/s with (39)

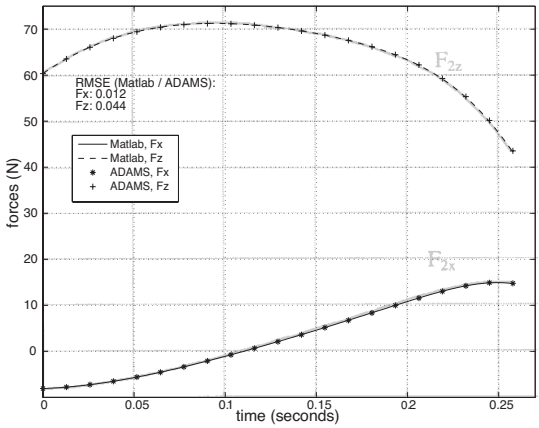

Figure 3.9 Comparison of rigid model results using MATLAB and ADAMS for front stance, 1.2 m/s with (39)

are provided in Table 3.3.

Model Parameter	Variable	Value
Lower / upper leg masses	m_1, m_2	2.25 kg
Torso masses	m_3	7.5 kg
Lower / upper leg lengths	l_1, l_2	0.3 m
Torso lengths	l_3	0.3 m
Lower / upper leg inertias	I_{l1}, I_{l2}	$0.0173\ \text{kg}\cdot\text{m}^2$
Torso inertias	I_{l3}	$0.0578\ \text{kg}\cdot\text{m}^2$

Table 3.3 Articulated model parameters

The vector of generalized coordinates are given by the state vector $q = [x, y, \theta_1, \theta_2, \alpha_1, \alpha_2, \alpha_3, \alpha_4]$. The horizontal and vertical position of the torso joint is specified by x, y, θ_1 is the angle with respect to the horizontal of the caudal portion of the body, θ_2 is the angle with respect to the horizontal of the cranial portion of the body, α_1

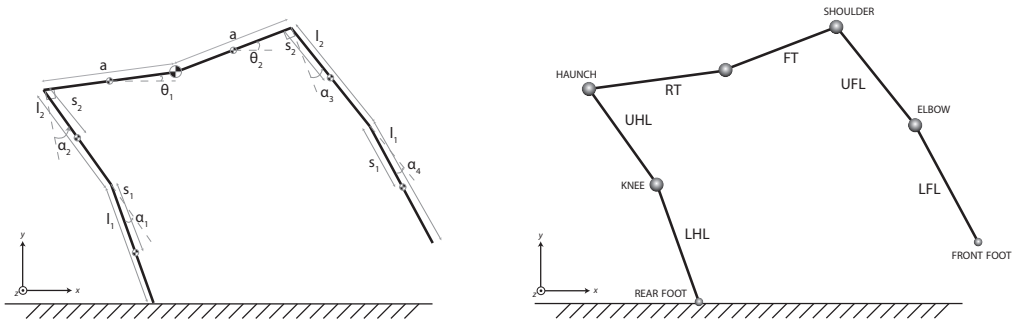

Figure 3.10 Articulated model general description

is the angle of the distal, caudal portion of the leg with respect to the proximal portion of the hind limb, α_2 is the angle of the proximal portion of the hind leg with respect to the perpendicular of the caudal torso, α_3 is the angle of the proximal portion of the foreleg with respect to the perpendicular of the cranial torso, and α_4 is the angle of the distal portion of the foreleg with respect to the proximal foreleg.

As a test case, the initial positions in Tab. 3.4 and initial velocities set by the fixed point analysis (Sect. sect:fixps) were input into the ODE45 integrator in MATLAB to determine the ground reaction forces during the rear and front stance phases.

Variable	t = 0	t = T	t = 2T
θ_1	0°	0°	0°
θ_2	0°	0°	0°
α_1	-10°	$-\alpha_2(0)$	-10°
α_2	-20°	$-\alpha_1(0)$	-20°
α_3	$-\alpha 1(0)$	$-\alpha 1(T)$	$-\alpha 1(0)$
α_4	$-\alpha_2(0)$	$-\alpha 2(T)$	$-\alpha_2(0)$

Table 3.4 Articulated model test case initial conditions

To validate the articulated model developed in MATLAB, an articulated model was constructed using ADAMS. Figs. 3.11 and 3.12 show foot force time histories from both the ADAMS and MATLAB models for a speed of 1.2 m/s. Excellent agreement between the force time histories is evident.

3.1.7 Foot contact

When the foot is in contact with the ground, several different constraints and requirements need to be met. Discussions follow regarding a no-slip constraint, friction cone bound, compressive foot contact force limit, and a bound on the allowable foot torque.

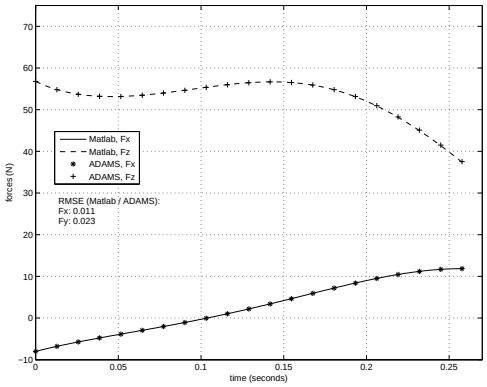

Figure 3.11 Comparison of articulated model results using MATLAB and ADAMS for rear stance at 1.2 m/s

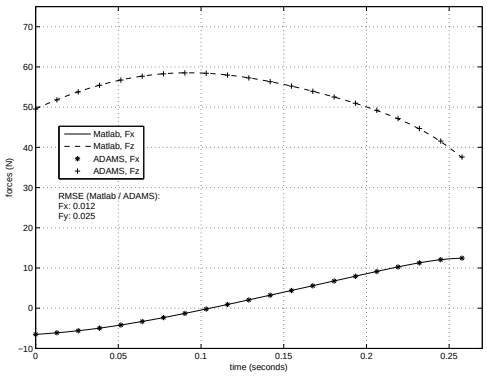

Figure 3.12 Comparison of articulated model results using MATLAB and ADAMS for front stance at 1.2 m/s

3.1.7.1 No-slip Constraint

During the support phases of the systems, the equations of motion reduce to a subset of Eqn. 3.1. This is accomplished by 'locking' the foot to the ground at contact and rewriting the equations of motion. The degrees of freedom of the systems are reduced by two. The front and rear stance equations are given by Eqn. 3.5, for $i = 1$ and $i = 2$ respectively.

$$A(\vec{q})\ddot{\vec{q}} + B(\vec{q},\dot{\vec{q}}) = D_G(\vec{q})G + D_i(\vec{q})F_i \tag{3.5}$$

For the rigid model, $\vec{q},\dot{\vec{q}},\ddot{\vec{q}}$ and G are 1 x 5 vectors, A,B and D_G are 5 x 5 matrices, D_i is a 2 x 5 matrix and F_i is a 1 x 2 vector. For the articulated model, $\vec{q},\dot{\vec{q}},\ddot{\vec{q}}$ and G are 1 x 6 vector, A,B and D_G are 6 x 6 matrices, D_i is a 2 x 6 matrix and F_i is a 1 x 2 vector. Additional information on the construction of these matrices is provided in Appendix B.

3.1.7.2 Compressive Foot Force and Friction Constraint

During any ground-foot contact, the ground reaction force in the vertical direction must be compressive for a physically realizable system (the foot is pushing against the ground). The results presented in Figs. 3.8 and 3.9 follow the inverted-pendulum trend for a low-speed gait (29). At higher speeds, the foot force positivity becomes more of an issue because the initial velocities of the stance phases increase. The compressive vertical force is a requirement during the stance phases and at the impulsive transitions.

The friction constraint bounds the ratio between the horizontal and vertical forces, also known as the *friction cone*. Friction coefficients from 0.5 to 0.8 have been used by others [(17), (67), (80)]. In this research, the friction coefficient was set to 0.65 for all simulations.

3.1.7.3 Foot/Ankle Torque

A foot/ankle torque between the foot and ground was added to the model, which was found to increase the stance duration, permitting a wider range of feasible solutions. This additional torque helped to somewhat mitigate the loss of the multi-legged step-out (as described in Sect. 3.1.3) due to the virtual leg simplification. There is also a biological motivation for including a foot torque. The canine's metatarsophalangeal joint connects biarticular muscles from the pelvis to the ankle, exerting a fairly significant ankle torque (149) that enables the toe-off motion exhibited during high-speed running. The value attributed to the extensor muscle joint torque is approximately 80 N·m. Multiplying this by typical durations of the stance phases from the simulations performed in this research gives an approximate impulsive ankle torque of 4 to 4.8 N·m·s.

Another method for approximating a foot / ankle torque bound uses the stance phase duration and maximum vertical force from the simulation results. A typical canine paw is about 0.05 m long (104) and the maximum vertical force during stance varies from 250 N to 350 N. Assuming no horizontal force contribution to the foot torque, results in a range of impulsive torque ankle values from 0.63 to 1.05 N·m·s for stance times ranging from 0.05 to 0.06 s (typical stance durations). Consequently, a foot torque upper bound was set to 2 N·m·s for both the rigid and articulated models.

3.1.7.4 Foot Velocity Minimization

Simulations of the models as described exhibited extremely large sensitivities to the placement of the front foot at the transition between the extended flight and front stance phases. In particular, large impulsive ground reaction forces, both compressive (admissible but

infeasible), and tensile (inadmissible and infeasible) were observed. To minimize these impulsive forces, a horizontal foot velocity minimization routine was included at the extended flight to front stance phase transition. Reducing the velocity of the foot to match the ground speed can mitigate the energy lost at impact [(21),(60),(61)] and when combined with the mid-flight impulsive torques, mimics the early retraction phase noted in high-speed cursorial locomotion [(59), (60)]. Since the flight phase is ballistic, the initial height and configuration angles at the end of the extended flight phase determine the foot velocity at touchdown. A linear interpolation was employed to solve for the height of the torso midpoint at the mid-flight transition to set the horizontal foot velocity to within 10% of a zero horizontal foot velocity. The value of 10% was chosen through trial and error and visual inspection of the simulated gaits, enabling a sufficient amount of solutions to proceed to the next phase while generating biologically feasible motions.

3.1.8 Impulsive Transition Bounds

As discussed in Sect. 3.1.2, the transitions between the velocities of the end of one phase and the velocities at the start of the next phase are accomplished through a balance of instantaneous impulsive forces and torques.

3.1.8.1 Force bounds

In the search to find a reasonable gait (one that meets all of the desired requirements and specifications), limits on the impulsive forces are included to frame the problem within a biological perspective. The discussion below provides references and background information for bounds on impulsive forces.

To estimate the impulsive vertical force bound, one can look at commonly reported values of the maximum vertical ground reaction force or impulsive force measures from biological experiments. From [(20), (73), (83), (105), (145), (146)], the maximum ground reaction vertical force for animals and humans is most commonly cited at 2 to 3 times the average body weight. The impulsive forces are represented by Eqn. 3.6.

$$I_F = \int F dt \tag{3.6}$$

Under the assumption of a step pulse force time history, the impulsive force is given as $I_F = F \cdot \delta t$, in which F is the maximum value of the force, and δt is the pulse time duration. With the total mass of both models as 24 kg, the maximum force is 706 N, with a

corresponding maximum impulsive force of 42.4 N·s (assuming a $\delta t = 0.06$ s, the average stance duration from the simulations). It is worth noting that these impulsive force bounds are in agreement with Schmiedeler's impulsive model in (130).

Walter and Carrier (143) recorded impulsive forces of galloping dogs with masses ranging from 23.3 to 34.2 kg and speeds from 8.4 to 10.2 m/s. The measured maximum impulsive vertical force was 90 BW·ms for a single hind leg, where the units are body weight milliseconds. The hind legs have a coupled impulsive value of 180 BW·ms, respectively. For a 24 kg animal, this is an impulsive force of 42.34 N·s. Bryant (27) recorded a maximum vertical impulsive force of 26.5 N·s for a single hind leg in a dog of mass 27 kg, galloping at a speed of 6.9 m/s, giving a maximum coupled value of 53 N·s.

In summary, for this research, a value of 50 N·s is selected as a reasonable bound on the magnitude of the impulsive forces.

3.1.8.2 Mid-flight Impulse

$$A(\vec{q})\ddot{\vec{q}} + B(\vec{q},\dot{\vec{q}}) = D_{I,G}(\vec{q})I_G \tag{3.7}$$

During the flight phases, there are no active torques or ground reaction forces as shown in Eqn. 3.4. Hildebrand (60) observed in his work with cheetahs that the forelimbs begin to move backwards prior to contact with the ground during the extended flight phase. Adding the impulsive torques in the middle of the extended flight phase, reverses the counterclockwise progression of the legs. This brings the foot in line with the shoulder, preparing for the next phase and reducing the impact with the ground, as suggested in Sect. 3.1.7.4. Another way to look at this is during the extended flight phase, the legs are opening up and out in both the front and rear portions of the body. Without any applied joint torques during the extended flight phase, the model would continue to open up, which is an infeasible trajectory. Consequently, mid-flight impulsive torques, represented by I_G (a 1 x 4 vector for the rigid model and a 1 x 5 vector for the articulated model) in Eqn. 3.7, were added to engender a more biologically realistic model by reversing the opening of the legs. After the impulsive torques at mid-flight are applied, the legs transition to a closing movement, bringing them down and in, underneath the body. This movement is clearly substantiated by observations of the biological system. There are no impulsive forces at mid-flight since the model is not in contact with the ground.

3.1.9 Active Torques

To ensure physically realistic solutions during the stance phases, a constant torque, herein referred to as an active torque, was activated on the joints connecting the legs to the torso. Active torques during stance phases are biologically realistic and expanded the feasible solutions found during the gait optimizations. The active torques are applied at the shoulder during front stance and at the haunch during rear stance. The inclusion of this torque is corroborated by other researchers studying biological systems and quadrupeds [(20), (47),(79),(82),(83)].

For model simplicity, only one joint torque, with a constant value, is activated in each of the stance phases. Adding the active torque proved necessary for the high-speed gaits. As the speed of the system increases, the ground reaction force drops when modeled using a purely ballistic model (39). The active torques have been limited (60 N·m) based on previous work (98) and physical experiments (148). Initially, the shoulder torque magnitude (active during the front stance) was set at 45 N·m while the haunch torque magnitude (active during the rear stance) was set at 60 N·m.

3.2 Optimization

With the equations of motion for the various phases fully defined, the dynamics of each phase are determined by a fixed point optimization. After the trajectories during each phase are set, the impulsive torques at the transitions are minimized, enabling a complete gait cycle consisting of the descending part of the extended flight phase, the front stance phase, the gathered flight phase, the rear stance phase and the ascending part of the extended flight phase. Once the full gait is defined, the initial foot placement and angular configurations are varied until a simulation converges to a reasonable gait for a given step frequency and speed. The last step in the process uses the cost of transport (CoT) to optimize the gait with respect to energy costs. Due to the large search space and nonlinearity of the problem, evolutionary algorithms are used to find a valid gait and then further refine and optimize the gait.

Several topics are addressed in this section, including a description of the fixed points and their function, what optimization technique is employed, how to generate the optimization seed, initial conditions, comparative metrics, additional bounds, the objective function construction and challenges encountered.

3.2.1 Fixed Points

A fixed point is the set of angular velocities that allows the system to move between one set of angles to another. The Newton-Raphson method is used to find the appropriate set of velocities between the start configuration (A) and end configuration (B) of a phase. In order to set the trajectory for a phase, a fixed point must be found. This section describes the general procedure for finding this fixed point and how it was incorporated in the current set of models.

$$\vec{q_B} - \vec{P}(\vec{q_A}, \vec{\dot{q}}) = 0 \tag{3.8}$$

The general form of the fixed point is presented in Eqn. (3.8). The vector $\vec{P}(\vec{q}, \vec{\dot{q}})$ is the resultant vector of positions after running the equations of motion with the start configuration, $\vec{q}$, and the initial guess, $\vec{\dot{q}}$. The fixed point is the set of velocities ($\vec{\dot{q}}$) that allow the system to get from the configuration at A ($\vec{q}_A$) to the configuration at B ($\vec{q}_B$). The method used to solve for the fixed points is the Newton-Raphson method. The solution procedure starts with an initial guess ($\vec{\dot{q}}$), then constructs the partial derivative by looking at the system states after a small δt has passed. The partial derivative is subsequently used to construct a line passing through $\vec{q}$ and $\vec{P}(\vec{q}, \vec{\dot{q}})$. The guess is adjusted until $\vec{q} = \vec{P}(\vec{q}, \vec{\dot{q}})$ or the difference between the $\vec{P}(\vec{\dot{q}})_{desired} - \vec{P}(\vec{\dot{q}})_{actual}$ is within the specified tolerance.

$$\vec{\dot{q}}^{k+1} = \vec{\dot{q}}^{k} - \nabla\vec{P}(\vec{\dot{q}}^{k})^{-1} \cdot \vec{P}(\vec{\dot{q}}^{k}) \tag{3.9}$$

If the initial guess is close to a desired solution, the system will converge. The range in which this convergence occurs varies but is known as the basin of attraction. In the simulations conducted for this investigation, the large range of values and sensitivity of the systems to the initial conditions, necessitated the construction of an automated fixed point routine within the evolutionary algorithm. A check was used to exit the routine if a solution was unstable. Instability in this instance was determined by the change in the velocity vector. If the differences continued to increase, rather than decreasing within the specified tolerance, then the solution was deemed unstable and the fixed point routine would end. A new initial guess was selected and the program continues until either a suitable solution is found or all points are exhausted and a new point is attempted.

The automated fixed point subroutine consists of two portions. The first part of the routine loops through an existing table of previously acceptable fixed points. These are fixed points initially found by trial and error when searching for a converged set of velocities over one given phase. Each phase has its own table of acceptable fixed points. To prioritize the search, the fixed points and their initial angular configuration are arranged according to

the sum of the squared differences of the angular configuration currently under evaluation and then each fixed point is attempted to see if it is within the basin of attraction (providing a converged solution).

If all fixed points in the list have been exhausted, a secondary procedure is called. This procedure attempts to find the fixed point on its own, using the most likely candidate from the first routine and decreasing the phase duration. If a fixed point is found, the phase duration is increased until the actual phase duration is reached. The new fixed point is added to the table, otherwise, the simulation exits and looks for another feasible solution. With this procedure, a large number of fixed points were accumulated for the fixed point reference table.

3.2.2 Simulated Annealing

The large number of variables and the problems' susceptibility to getting mired in local optima led to the use of a global optimizer to search for valid gaits. Global optimizers search through multiple basins of attraction, whereas local optimizers tend to locate a minimum in the nearest basin of attraction to the initial seed. Although the possibility of finding more and better solutions increases with a global optimizer, there are disadvantages. The largest impediments to a global optimizer is the time necessary to cover the search space adequately and convergence.

Typically, evolutionary algorithms best are used for nonlinear, global optimization problems. Amongst the evolutionary algorithms, the simulated annealing (SA) was chosen for the gait optimization studied herein.

3.2.3 Seed and Initial Conditions

As with any evolutionary algorithm, starting with an appropriate seed enables the optimizer to narrow the search space and converge more quickly. The seed for the simulated annealing algorithm consists of the angles at the start of each way point and the initial foot placement at touchdown of the extended flight phase. The term *way point* is used as the description of the kinematics at the start of a phase (the set of angles defining configuration A). There are four main way points, specifying the angles at the start of the four gait phases: extended flight, front stance, gathered flight and rear stance. The fifth way point is the set of angles at mid-flight. The other variable is the first foot plant location.

For the rigid system, the full number of variables is 26 and for the articulated, 31. Initially, to reduce the complexity of the system, symmetric boundary conditions (39) were

used. The angles were set by using the images from Hildebrand's work, scaling these to find appropriate limb lengths, and extracting the resultant angles and foot placement. Using symmetry enabled a reasonable range of gait trajectories to be found quickly. This symmetry constraint was subsequently removed to open the search space. Once the seed was chosen, the dynamics of each phase were computed by integrating the equations of motion using the initial conditions: the angles and foot placement set by the user and the velocities determined by the fixed point analysis. The prescribed kinematics and solved dynamics define the motion of the system during a phase. If all contact forces are positive, all friction cone values are less than 0.65, all impulsive ankle torques are less than 2 N·s and the horizontal foot velocity at the extended flight to front stance transition is less than 0.5 m/s, the resultant force and torque information is passed to the objective function to determine the fitness of the solution.

3.2.4 Cyclic Gait

A cyclic gait occurs when the gait is repeatable. Mathematically, a cyclic gait is defined when the difference between the angular velocities (and positions) of a single instance in the gait and those of the next repeated instance are zero. The gait cycle starts at the top of the extended flight phase and ends at the next top of the extended flight phase. Therefore, the final check in the simulation compares the angular velocities at the start of the gait cycle (the beginning of the descending part of the extended flight phase) to the angular velocities at the end of the gait cycle (at the end of the ascending part of the extended flight phase, immediately after the mid-flight impulsive torques have been applied). Since the full stride transition occurs in the middle of the extended flight phase, the ballistic trajectory dictates the horizontal and vertical velocities of the system. The height of the body at the start of the extended flight phase is set by the acceptable solution for the foot velocity minimization. The sum squared difference of the angular velocities determines if the solution is promoted to the next stage, where the objective function is calculated and sent to the optimizer. A tolerance of 0.01°/s was used as the upper limit in the maximum difference for allowable solutions.

3.2.5 Optimization Bounds

As noted above, the simulated annealing algorithm is a good choice for a bounded nonlinear optimization. Bounds on the variables (angles and foot placement) needed to be carefully specified for effective optimization. The initial phase of the optimization searched for a

viable gait. During this initial search, the bounds on the angles were fairly large- starting at $\pm 40^\circ$ and decreasing to $\pm 20^\circ$. Then, as the simulations progressed (and the symmetric boundary conditions were released), the angular bounds were reduced and varied from $\pm 2.5^\circ$.

The other optimization variable was the foot placement after the extended flight phase (δ_{foot}). The foot placement after the gathered flight phase was set by the speed and stride frequency relationship, and so was not considered as a variable. Because the model had to continually move forward for feasible motion, the horizontal position of the second foot has to be greater than the horizontal position of the first foot placement. The speed, step frequency, and initial foot plant explicitly define the second foot plant, therefore, the first foot plant is bounded- it has to be less than the total step length for the system to make reasonable forward progress.

3.2.6 Objective Function

Optimization algorithms require at least one objective function whose value is minimized (or maximized). Two objective functions were employed in this research, one to guide the gait selection optimization, and a second using cost of transport (CoT) to maximize gait efficiency, once a reasonable gait was found.

3.2.6.1 Gait Selection

The gait selection objective function underwent several variations in order to find the right balance of competing variables. Eqn. 3.10 shows the final objective function used to find a suitable gait.

$$SM = \Sigma I_{G,i}^2 + c_1 \cdot (I_{F,x}^2 + I_{F,y}^2) + c_2 \cdot (I_{F,x}/I_{F,y}) + c_3 \cdot I_{F,y,max} + (G_i \cdot t_{stance})^2 \qquad (3.10)$$

The subscript i corresponds to the joint ($i = 1:5$ for the rigid model and $i = 1:6$ for the articulated model). $I_{G,i}$ is the impulsive torque at joint i; $I_{F,x}$ and $I_{F,y}$ are the horizontal and vertical components of the impulsive forces and G_i is the active torque joint i (noting that only the haunch and shoulder joints have any non-zero active torque values). The variables c_1, c_2 and c_3 are weights on the sum of the squares of the impulsive forces, the friction cone weight and the weight of the impulsive vertical force, respectively. These weights were set based on trial and error and have values assigned via a step function. For example, if the sum of the squares of the impulsive forces is less than 50^2, then $c_1 = 0.1$. If it is greater,

then $c_1 = 0.5$. The friction cone ratio is the relationship between the horizontal and vertical forces (see Sect. 3.1.7.2). The value is weighted based on the friction limit- if the value is less than 0.65, then $c_2 = 0.1$, otherwise $c_2 = 500$. If the vertical impulsive force is negative, then a large penalty is incurred ($c_3 = 10^3$), otherwise $c_3 = 0$.

3.2.6.2 Gait Optimization

After a reasonable gait was found, the energetics of the system were analyzed to optimize the system for a given speed and stride frequency. The cost of transport (CoT) is a common metric used to evaluate legged systems [(12),(29),(54),(71),(106)] and provides a fair comparison because it is a non-dimensionalized measure of the total work done by the system to move through one full gait cycle.

The CoT is the amount of work as specified by Eqn. 3.11 necessary to move a weight over a unit distance and is given by Eqn. 3.12. Note that, since the system returns to the same height at the start and end of the cycle, the change in potential energy is not included in the total work equation.

$$W_j = \Sigma[1/2 \cdot m_i(\vec{v}_{ai,i}^{\,2} - \vec{v}_{bi,i}^{\,2}) + 1/2 \cdot I_i(\vec{\omega}_{ai,i}^{\,2} - \vec{\omega}_{bi,i}^{\,2})]$$

$$W_{total} = \sum_{j=1}^{5} |W_j| + |\Delta KE_{FS}| + |\Delta KE_{RS}| \tag{3.11}$$

$$\frac{W_{total}}{m \cdot g \cdot SL} \tag{3.12}$$

The subscript i in the equations refers to the body, *ai* is *after impulse* and *bi* is *before impulse*, m_i is the mass of body i, $\vec{v}_i$ is the component vector of body i's center of mass velocity, I_i is the moment of inertia of body i and $\vec{\omega}_i$ is the angular velocity component of body i. The subscript j references the impulsive transition. The other terms in the total work equation (ΔKE) are the change of the kinetic energy over the stance phases, where the active torques are turned on. The subscripts describe the phase- *FS* denotes front stance and *RS*, the rear stance.

3.2.7 Challenges

There were many challenges during the development of the models. While working through these, many lessons were gleaned. For instance, the ankle torque was a physically realistic

aspect of the biological system not initially captured in the modeling (due to the use of the point foot). Moreover, its inclusion reduced the simulation convergence time significantly. Another instance involved the active torques. Without the addition of these torques during stance, the number of converged solutions was much smaller and often not biologically realistic. It also has a physical corollary and is a sensible model addition.

As expected, the articulated model, with its additional degree of freedom, has a much larger configuration space in which a valid gait could be found. Once a gait was found for the rigid model, very little change to the objective function was observed; whereas with the articulated model, there was more room for the simulated annealing algorithm to optimize the solution based on the chosen objective function. However, enforcing the cyclic gait was also more difficult than anticipated with the articulated model. Adjustments were made to ensure start and end conditions were matched, including a subroutine to optimize the available joint torques. The rigid model was able to minimize the error between the mid-flight velocity jumps much better than the articulated model.

This chapter presented all of the necessary and appropriate constraints, bounds, simulation settings and parameters required to run both models, generate reasonable gaits and optimize those gaits. Understanding all of the pieces in the model, as well as the inherent limitations introduced through the various assumptions and constraints, provides a context for the interpretation of the results. The results, and a detailed analysis of their implications, are provided in the next chapter.

Chapter 4

Results and Discussion

This chapter presents the results from the gait generation and optimization. Using the models described in the last chapter, gaits for the rigid and articulated models were found and subsequently optimized. Speed and step frequency were the primary design parameters, incrementally varied and optimized. Since the rigid and articulated models demonstrate different trends, the results are addressed individually, followed by a comparison of the two. The outcomes of the many trials are evaluated and the effect of the spine's articulation on the energy demands analyzed.

For the purposes of optimization and comparison, a suitable measure is necessary. A common metric used when observing these types of systems is the dimensionless measure cost of transport (CoT) [(12),(29),(54),(71),(106)]. The cost of transport is the amount of work given by Eqn. 4.1 necessary to move a weight over a unit distance as shown in Eqn. 4.2.

$$W_j = \Sigma[1/2 \cdot m_i(\vec{v}_{ai,i}^{\,2} - \vec{v}_{bi,i}^{\,2}) + 1/2 \cdot I_i(\vec{\omega}_{ai,i}^{\,2} - \vec{\omega}_{bi,i}^{\,2})]$$

$$W_{total} = \sum_{j=1}^{5} |W_j| + |\Delta KE_{FS}| + |\Delta KE_{RS}| \tag{4.1}$$

$$\frac{W_{total}}{m \cdot g \cdot SL} \tag{4.2}$$

In Eqn. 4.1, W_{total} is the total work done on the system. The other variables are m, total mass (24 kg for both models), g is gravity and SL is the stride length, the total distance traveled from the top of flight to the next top of flight measured from the same location on the body. Although CoT is dimensionless, units of J/(N·m) are typically given. Typical values for biological systems range from 0.1 to 0.25 J/(N·m) [(59), (78), (147)], providing a general range for potential solutions.

The subscript i in Eqn. 4.1 refers to the i^{th} body, *bi* is the state just prior to the instantaneous impulsive transition (*before impulse*), *ai* is the state immediately after the

instantaneous impulsive transition (*after impulse*), m_i is the mass of body i, $\vec{v}_i$ is the component vector of body i's velocity, I_i is the moment of inertia of body i and $\vec{\omega}_i$ is the angular velocity component of body i. The subscript j references the impulsive transition. The other terms in the total work equation (ΔKE) are the changes of the kinetic energy over the stance phases, where the active torques are turned on. Subscripts *FS* and *RS* denote front stance and rear stance, respectively.

In order to understand the terminology regarding the organization of the full stride described in the following plots, the gait is broken down into pieces corresponding to their energetic contribution. These parts have impulsive torques and impulsive forces, acting at the instantaneous transitions, or an active torque, turned on during the stance phase, contributing to the total work of the system.

- ***41a***: Transition from the rear stance phase to the first half of the extended flight phase.
- ***1a1b***: Transition at mid-flight.
- ***1b2***: Transition from the second half of the extended flight phase to the front stance phase.
- ***2***: Front stance phase (active torque during forward stance phase).
- ***23***: Transition from the front stance phase to the gathered flight phase.
- ***34***: Transition from the gathered flight phase to the rear stance phase.
- ***4***: Rear stance phase (active torque during rear stance phase).

These transitions and stance phases are shown in Figs. 4.1 and 4.13, for the rigid and articulated models respectively, with each colored configuration representing a corresponding shared end / start of a phase. The active torques (*2, 4*) are turned on for the duration of the front and rear stance phases, whereas the others- *41a, 1a1b, 1b2, 23,* and *34*- are instantaneous impulsive transitions linking the ballistic flight phases (non-stance) to each other (*1a1b*) or the appropriate stance phase.

4.1 Results: Rigid Model

The rigid model consists of five bodies connected by frictionless pin joints. All simulations were run in Matlab using an evolutionary algorithm to initially find a reasonable gait and subsequently, further refine the solution to minimize the total work necessary for a full, cyclic stride.

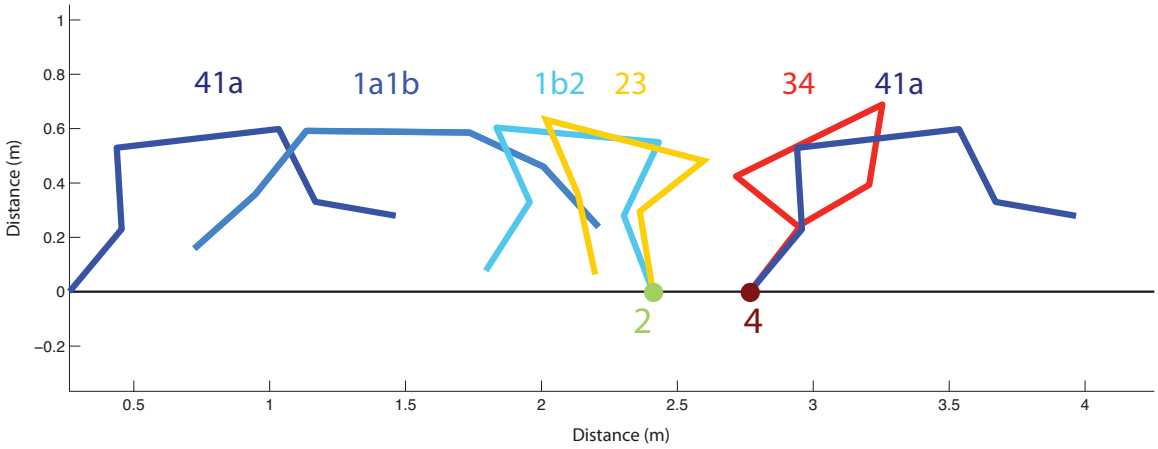

Figure 4.1 Phase transitions and stance phases of the rigid models' gait

4.1.1 Cost of Transport

In order to answer the question of how the spine affects a quadruped system at high speeds, a baseline model with a rigid spine was constructed. Many simulations were conducted for speeds ranging from 6.0 m/s to 9.0 m/s and stride frequencies ranging from 0.90 s^{-1} to 3.0 s^{-1}. The speeds were chosen based on the analysis of existing quadruped models (Table 2.1), most of which operated at slow speeds of 4 bodylengths/s. The models presented here attempt to fill this gap, with simulations running at speeds of 10 - 15 bodylengths/s. The primary metric for the gait optimization is the cost of transport.

All values of the CoT from the optimized speed and stride frequency trials are presented in Fig. 4.2. Different mechanisms are at work on either side of the stride frequency range investigated. Each set will be addressed separately to step through the various trends present.

There are two primary metrics at work in the CoT- the total work and the stride length. The CoT is proportional to the total work (Fig. 4.3) and inversely proportional to the stride length (Eqn. 4.2). The total work is driven by the changes in kinetic energy of the bodies, linked to the velocity jumps across the transitions. The impulsive forces (Fig. 4.4) and torques (Fig. 4.5) are the energetic inputs to the system, necessary to transition to the desired ballistic velocities at the start of the next phase. The haunch torque at the *34* transition is the maximum (Fig. 4.6), associated with the start of the phase that requires the largest angular reconfiguration.

For stride frequencies greater than 2 s^{-1}, the increase in CoT with increasing stride frequency is attributed to the rear stance phase (Phase 4). There is a large shoulder torque after the gathered flight phase to accommodate the amount of reconfiguration required (Fig. 4.7)

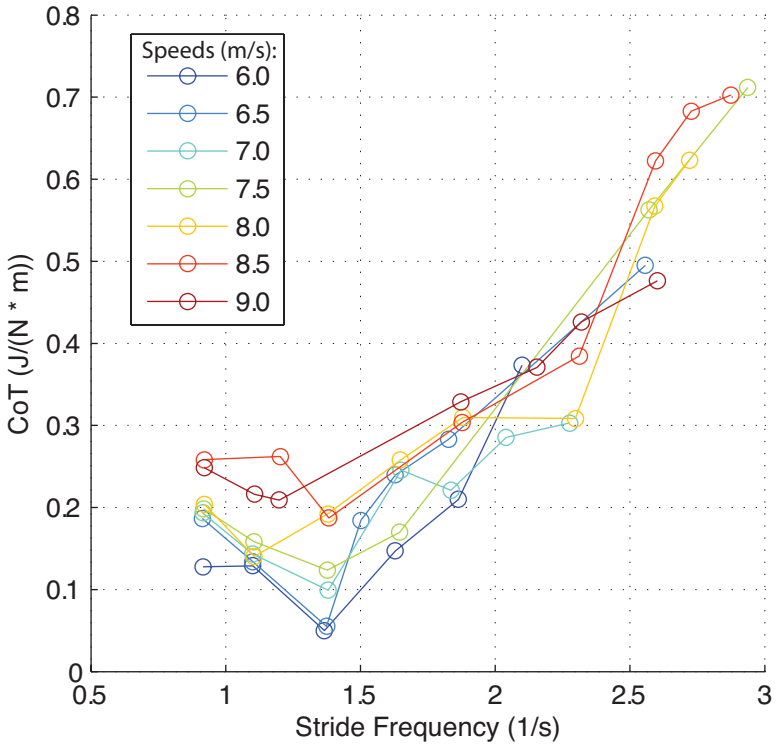

Figure 4.2 Cost of transport as a function of stride frequency

in the rear stance phase over a decreasing amount of time. The rear stance phase (Phase 4) has the highest ratio of angular change to time with the front leg accounting for the majority of this change, stretching from the tucked position under the body to a forward extension in front of the body. The gait has a more biological distribution between stance and flight phases (20% / 80%), and is typical of values seen in galloping greyhounds (141).

At the lower stride rates (2 s^{-1} and lower), the CoT reaches a minimum value near 1.4 s^{-1} and then begins to increase as stride frequency decreases. The gait in the low stride frequency region (less than 1.4 s^{-1}) is different than the expected biological gait. By lengthening the flight phases, the system is able to accommodate the long stride lengths (Fig. 4.8). These long flight phases lead to a gait similar to a kangaroo or a triple jumper. The impulsive torques start to increase rapidly after 1.4 s^{-1}, but are balanced by the long stride lengths resulting in a less dramatic increase in the CoT. The long flight phases are the primary cause for the sharp increase in the impulsive torques. In the low stride frequency range, a large impulsive torque occurs at the haunch and shoulder, while the high stride frequencies are dominated by the large shoulder torque. The torques at the lower stride rates are all working to adjust the body velocities at the pre- and post-gathered flight transitions.

In the range of stride frequencies evaluated, the CoT increases at the extents (high and

low stride frequencies). For the given gait, it is unlikely that the CoT will decrease at stride frequency values higher or lower than those investigated, as evidenced by the impulsive torques' parabolic relationship. Physically, the cost to move the system the long distances at the low stride frequencies starts to quickly overcome the benefit of the amount of ground covered. At the opposite end of the spectrum (high stride frequencies), the system is limited by its foot placement and the time available for configuration (speed is fixed). The search algorithm has increasingly more difficulty finding feasible solutions in this range.

In summation, the rigid system favors a low stride frequency with an optimal value of 1.45 s^{-1} for the ranges investigated. Although the gait demonstrated with these conditions is non-biological in nature, it emphasizes the awkwardness of the rigid back, underscoring the energetic preference of a long gathered flight phase to accomplish the crossover necessary to provide a smooth and continuous gait. Even though the gait is biologically unusual for a quadruped, the values for the CoT of the rigid system have a median around typical biological values, albeit at lower stride frequencies than a canine-sized galloping quadruped.

4.1.2 Total Work

The total work is the absolute value of the sum of kinetic energy changes of all bodies across the impulsive transitions and stance phases (Eqn. 4.1). It is proportional to the CoT and as a metric, it focuses on the energetics of the system without the influence of the stride length introduced with the CoT definition.

The minimum total work value occurs at the minimization of the velocity changes across all transitions. Across all speeds and stride frequencies, the majority of the energy is involved in moving the system through the rear stance phase and preparing for the extended launch phase. It is only at the very low stride frequencies that this trend shifts towards the gathered flight phase. Stepping through the gait time histories, fractional energy plots and internal work plots will clarify these relationships.

4.1.3 Maximum Impulsive Forces

An analysis of the energetic components provide a better understanding of the physical limitations affecting the system. There are three main components changing the kinetic energy of the system: 1) impulsive forces, 2) impulsive torques, and 3) active torques. The potential energy affects the instantaneous energy, but has zero contribution overall since the system returns to its original position at the end of the gait cycle.

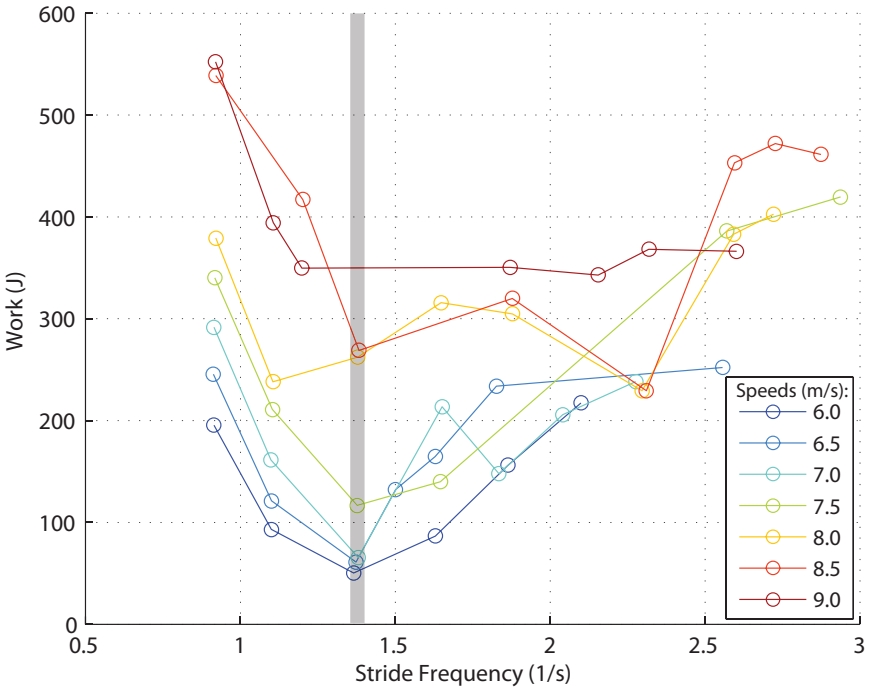

Figure 4.3 Total work as a function of stride frequency

The maximum vertical impulsive force is the primary force of interest. With the friction cone constraint in place (see Sect. 3.1.7.2), the horizontal impulsive force will always be less than the vertical force. The maximum vertical impulsive forces plot in Fig. 4.4, shows a large variation (20 - 135 N·s) over the range of stride frequencies investigated. The forces are increasing at stride frequencies less than 2 s^{-1} and approach an asymptotic minimum at those greater than 2 s^{-1}.

At the low stride frequencies, the system has a long gathered flight phase, necessitating a large vertical impulse to propel the system into the air. There is also a correspondingly large impulse on landing. At the other end of the spectrum, with increasing stride frequency, the center of mass trajectory becomes flatter, reducing the vertical impulsive forces necessary to move the system. The gray line superimposed on Fig. 4.4 indicates the stride frequency of the minimum CoT and is used as a reference for observations when applicable.

4.1.4 Maximum Impulsive Torques

As mentioned in the stride frequency and CoT discussion, the impulsive torques are determined by the disparity between the velocities at the end of a phase and the initial velocities required at the start of the next phase. Fig. 4.5 displays the maximum impulsive torques

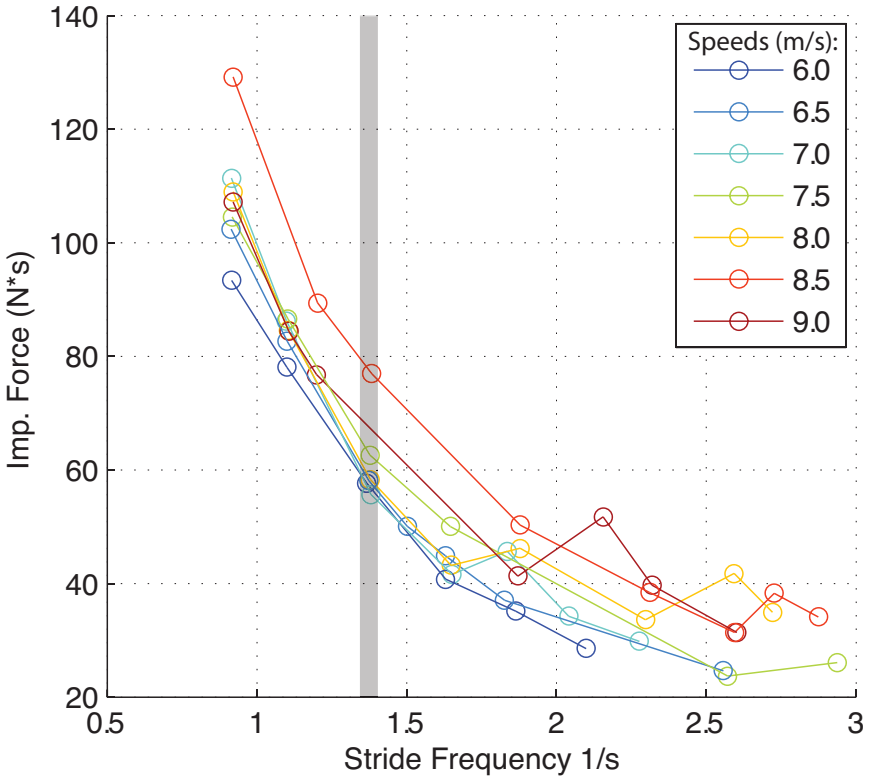

Figure 4.4 Maximum vertical impulsive forces across all phases and joints

over the course of the entire gait cycle (all phases, all joints).

The maximum impulsive torque values are generally increasing above a stride frequency of 2.25 s^{-1}, as well as below a stride frequency of 1.45 s^{-1}, although at the lower stride frequencies, the increase is much sharper than at the higher stride frequencies. The torques range from 10 to 20 N·m·s, and are the primary method for the system to match the velocities desired.

The gray line on the plot indicates the minimum CoT's stride frequency. The maximum impulsive torques corresponding to this line show the last set of values before the sharp increase the torques and represents the ideal stride frequency that minimizes the velocity changes at the transitions. The joints and transitions responsible for these large torques will be discussed in the next section.

With increasing speed, the impulsive torques get larger. As the system moves faster, the time available for a phase is decreased (at a constant stride frequency), necessitating a larger torque to accomplish a similar reconfiguration in a shorter amount of time. The reconfigurations are nearly the same since the way points change little between speeds.

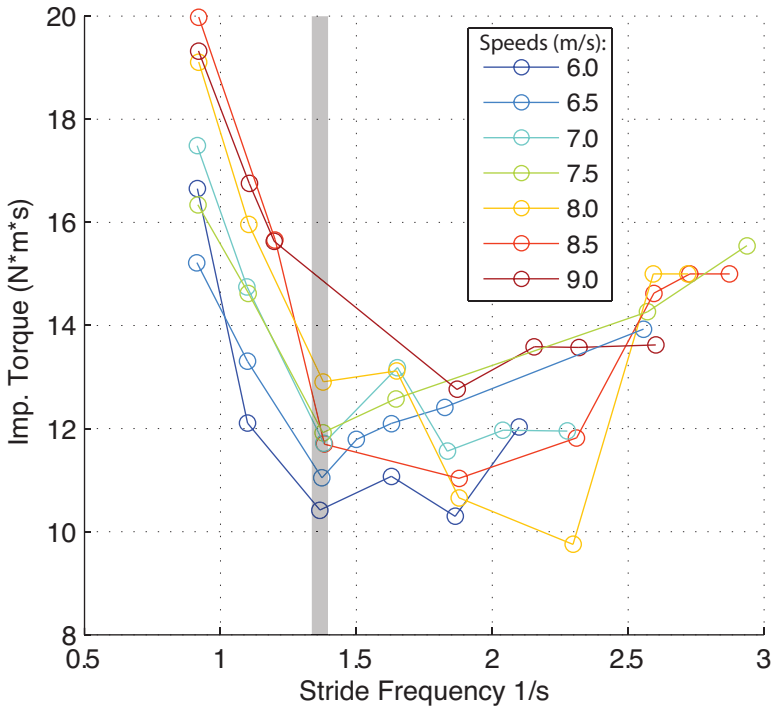

Figure 4.5 Max impulsive torques across all phases and joints

4.1.5 Impulsive Torques by Joint

Fig. 4.6 presents the scatter of the impulsive torque magnitudes as a function of stride frequency for the joints of primary interest, the haunch and the shoulder. The other joints are not included since the torques are smaller and are relatively constant across stride frequencies. The colors represent the speed and the symbols signify the phase transition.

At low stride frequencies, the maximum impulsive torque occurs in the transition just prior to the launch phase- *34* transition- in the haunch. The shoulder joint at the *23* transition has a similar magnitude. Both values occur at the lowest stride frequencies. The gray curved arrows pointing to the left show the general trend of the haunch and shoulder torques at these transitions, starting low at the high stride frequencies and reaching their maximum at the lower ones. The large haunch torque after the gathered flight phase is pushing the hips forward, while the shoulder torque before the gathered flight phase is acting to pick up the front of the body, rotating the body from nose down (before gathered flight) to nose up (after gathered flight).

The arrow pointing to the right shows the trend for the shoulder torque at the *34* transition. The torque is a maximum at the highest stride frequency investigated, then decreases in the middle range and increases slightly at the low stride frequencies. The haunch and shoulder torques at the *34* transition are opening up the body to prepare for launch into

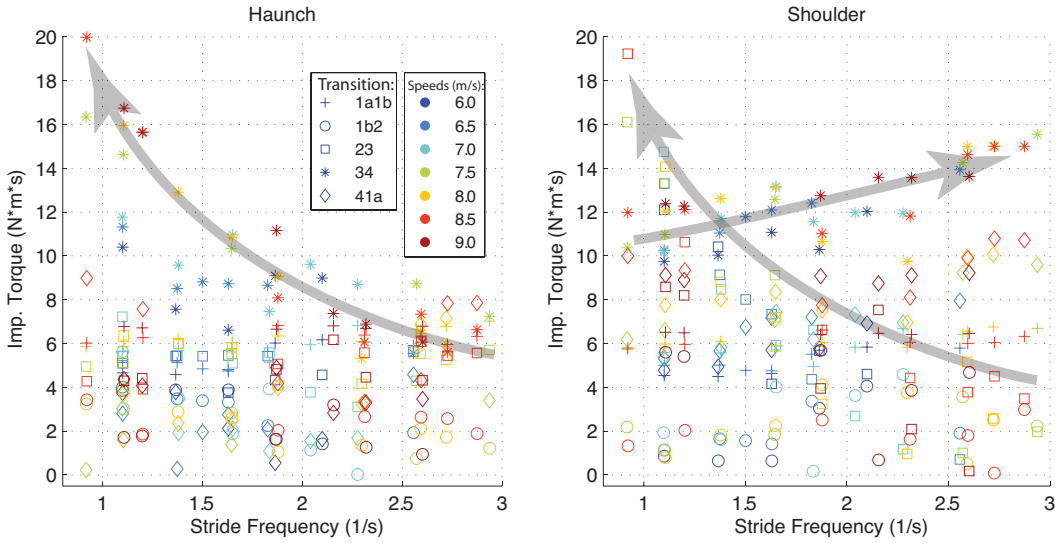

Figure 4.6 Impulsive torques at the haunch and shoulder for all impulsive transitions as a function of stride frequency

the extended flight phase. The magnitudes are linked to the amount of reconfiguration occurring in the rear stance phase. Since the stance durations are about the same for the two stride frequencies (0.064 s and 0.072 s, for 2.9 s^{-1} and 1.6 s^{-1} respectively), the velocities at the start of the rear stance phase (after impulse) are similar between the two cases, with the exception of the lower front leg. The velocities of the front leg at the lower stride frequencies are significantly lower, reducing the internal work and lowering the CoT value.

4.1.6 Reconfiguration

To clarify how the impulsive torques are acting on the bodies, Fig. 4.7 shows the configurations for transitions *34* and *41a* at the example stride frequencies of 1.6 s^{-1} and 2.9 s^{-1}. The corresponding signed impulsive torques at the start of phase 4 (the *34* transition) are indicated on the diagrams. The angular velocity signs follow the convention of positive, counter-clockwise rotation. The impulsive torques and forces are acting on the bodies to transition the system from the before-impulse velocities to the desired after-impulse velocities. The figure clarifies how the bodies are moving in relation to each other and whether the selected limb pair is either opening or closing. Both the shoulder and haunch torques are large, necessary for the desired reconfiguration to prepare for launch into the extended flight phase. This is the dominant transition at the intermediate and high stride frequencies, shifting to the *23* transition at the lower stride frequencies, corresponding to the pre-launch

of the gathered flight phase.

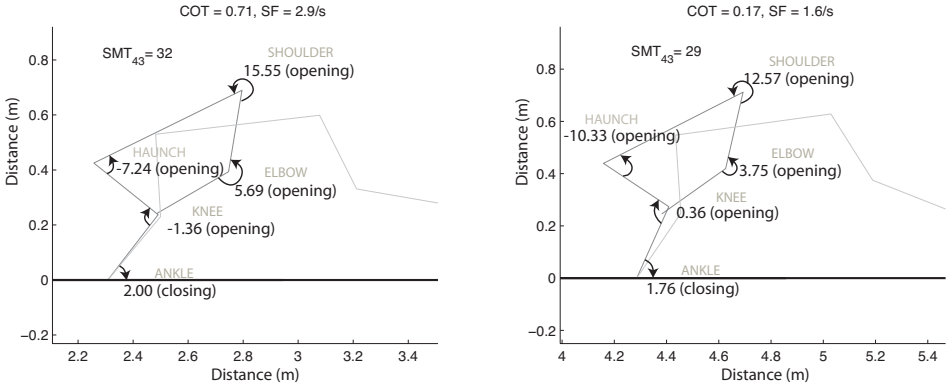

Figure 4.7 Impulsive torques at *43* transition, 7.5 m/s at high (2.9 s^{-1}) and low (1.6 s^{-1}) stride frequencies

4.1.7 Gait Time History

To visually inspect how the gaits differ across the range of stride frequencies, a representative speed of 7.5 m/s is investigated. The trends are similar for the other speeds. Fig. 4.8 shows a range of stride frequencies to better illustrate how the system is behaving by capturing a single frame after a δt, creating a time / position history of the system in a single image. The figures are zeroed to the hip location at the top of flight. At the lower stride frequencies, the rigid model displays a gait similar to a long jumper, with a lengthening gathered flight phase. In general, with a decrease in stride frequency, the rigid system increases the time in flight, with the majority occurring in the gathered portion.

4.1.8 Fractional Energy Plots

Evaluating which part of the gait has the largest contribution to the total energy change provides an understanding of the increase in CoT. The impulsive torques for each transition and the active torques during stance phases are plotted as a fraction of the total change in energy for all speeds and stride frequencies in Fig. 4.9.

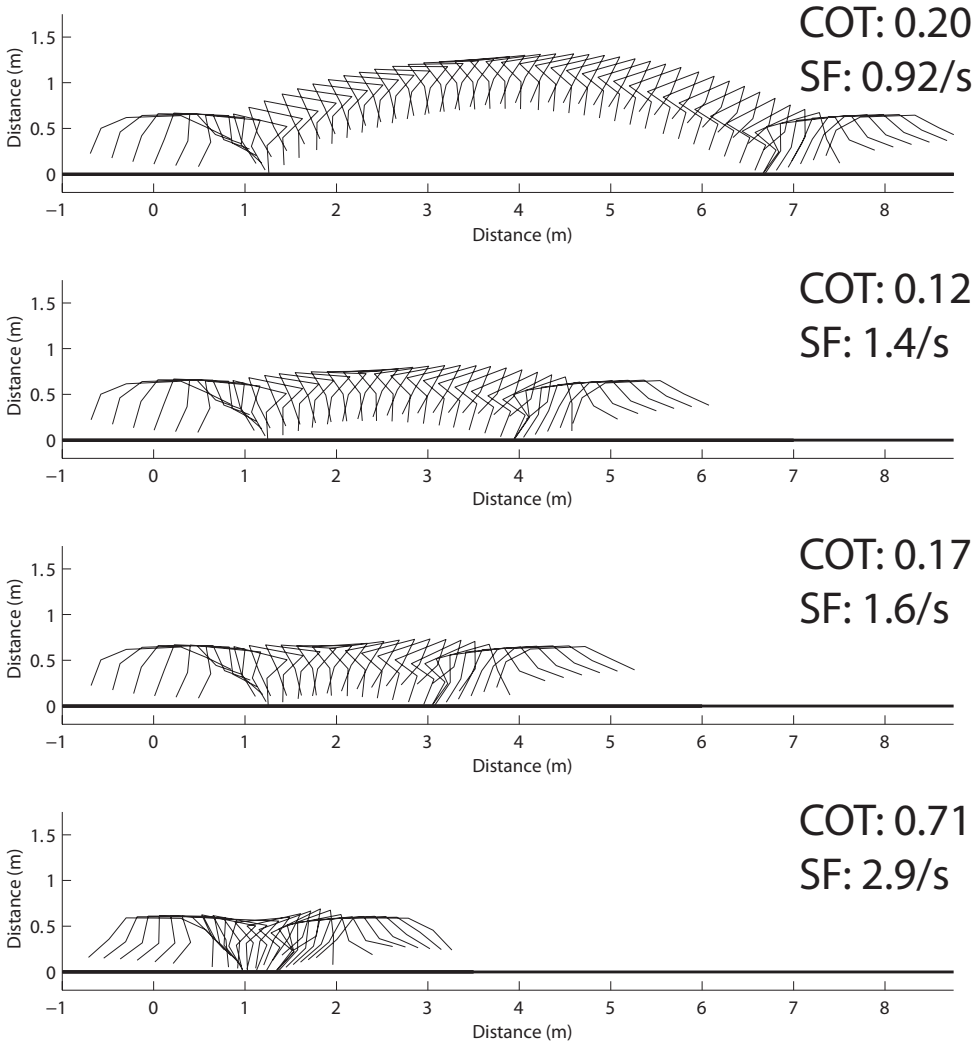

Figure 4.8 Stick figure plots at 7.5 m/s

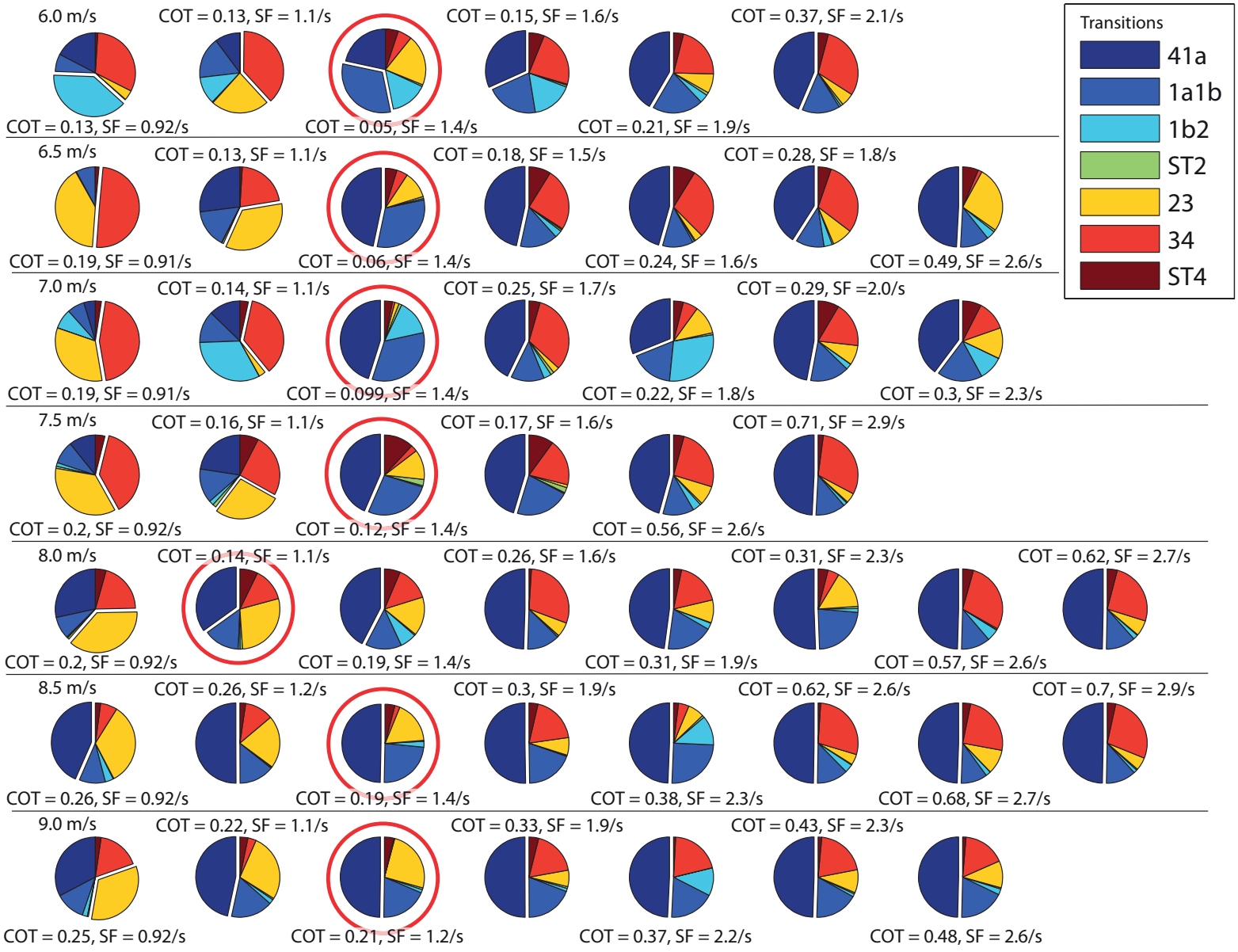

Figure 4.9 Fractions of energy changes for all speeds and stride frequencies, with red boxes denoting minimum CoT for each speed

The dominant phase, evident in the majority of the fractional energy contribution charts, is the impulsive transition prior to the extended flight phase (*41a*). Biologically, this is the primary propulsion portion of the gait cycle and is expected to have the highest contribution. At the lower stride frequencies, the *23* and *34* transitions tend to contribute a large fraction of the total energy as these bound the gathered flight phase, where the largest distance is covered, requiring large torques and forces for launch and landing.

4.1.9 Potential and Kinetic Energies

Although these charts give a simple overall picture of the fractional energies, it is useful to view the changes of the absolute energy over time. To visualize how the energy changes over the total duration of the gait cycle, the changes in potential energy (*PE*) and kinetic energy (*KE*) are plotted in Fig. 4.10. The plots are zeroed to the start of the extended flight phase.

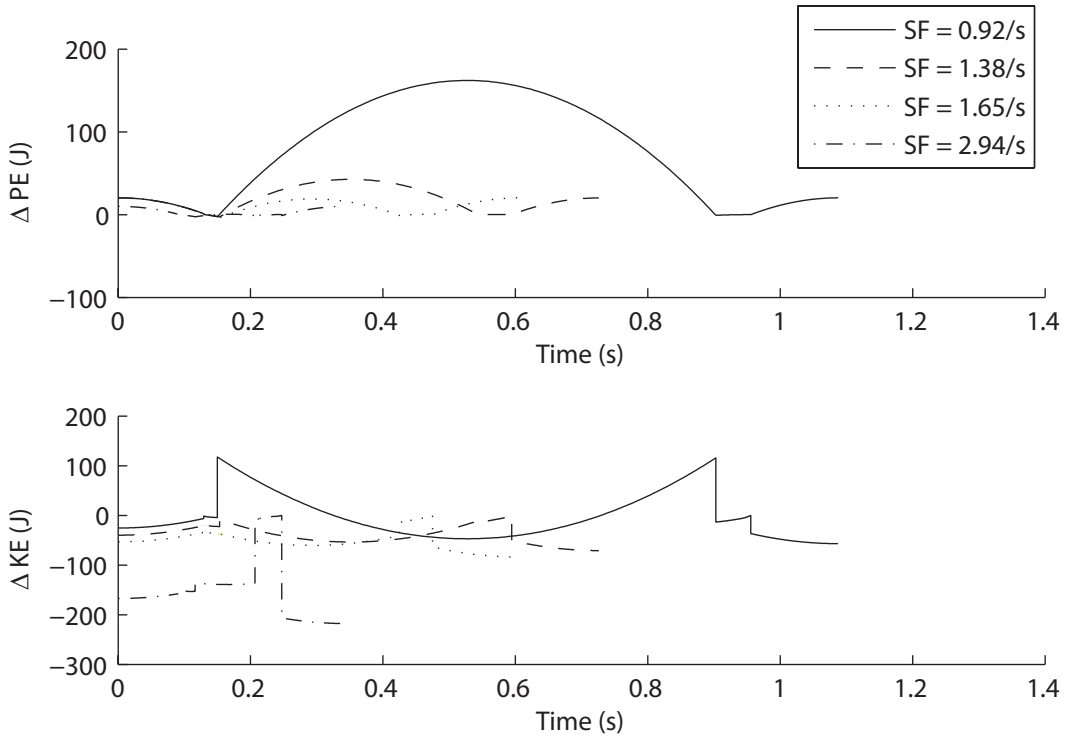

Figure 4.10 Change in *PE* and *KE* over the total time of one gait cycle

Summing the absolute values of the changes in the kinetic energy plot gives the total work, providing a visual representation of the time history of the changes in energy over the full gait cycle. The potential energy plot shows a decreasing amplitude as the stride frequency increases. At the lower stride frequencies, the impulsive force is greater due to

the high vertical leap in the gathered flight phase and is reflected by the large changes in the center of mass height (change in potential energy). At the higher stride rate, the maximum impulsive force decreases, mostly due to the lack of the long, gathered (ballistic) flight phase, the presence of which necessitates a trajectory with enough height to cover the large distance, shown in the time-lapse stick figures of Fig. 4.8.

In the kinetic energy plot, the legs of the higher stride frequency system are moving quicker and the acceleration (then subsequent deceleration) of the rear stance phase is the origin of the large energetic cost. This plot will be discussed in more detail in the next section.

4.1.10 Kinetic Energy in Detail

The final energy plot, Fig. 4.11, in this section details the kinetic energy changes, starting with the instantaneous kinetic energy change plot from the internal work section, the fractional energy charts appropriate for the four stride frequencies used to investigate trends in more detail and lastly, the translational and rotational kinetic energies for the individual bodies. All of these are for 7.5 m/s. All other speeds can be found in the appendix but follow similar trends to those described in the 7.5 m/s.

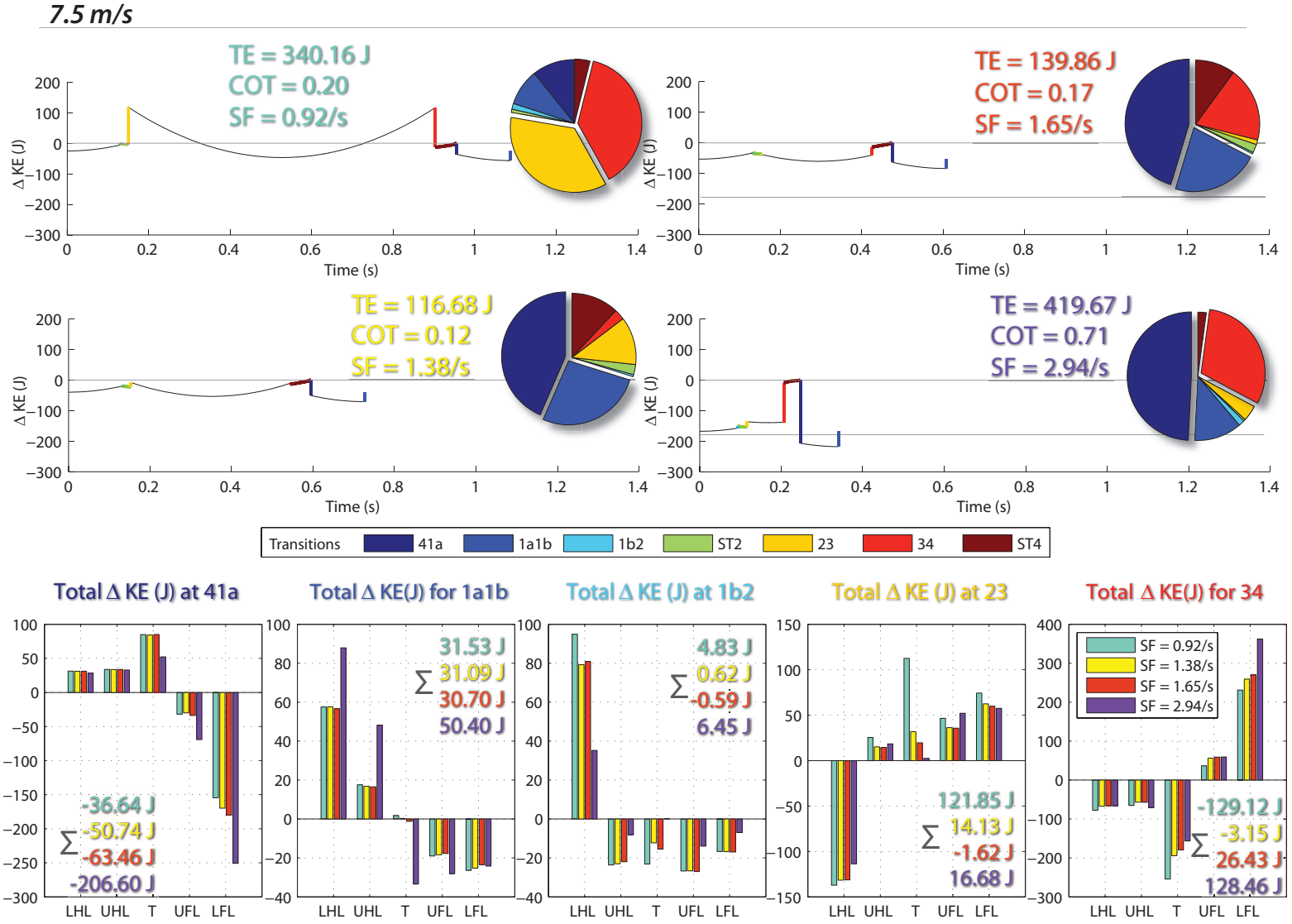

Figure 4.11 Kinetic energy changes in detail for 7.5 m/s

The first plot is the instantaneous change in the kinetic energy as a function of the total stride duration. The colors overlaid on top of the curves correspond to the transitions and stance phases that contribute to the total work. The colors correlate to the fractional energy plots, displayed in the next level of the plot. The fractional energy is a relative measure but provides a visual corollary to the kinetic energy plots. The final set of plots in this group displays the translational and rotational changes in kinetic energy for the *34* transition (left set of bar graphs) and the *41a* transition (right set of bar graphs). The main components of the energies to be investigated in detail are the largest impulsive torque transition (*34* transition) and the largest fractional energy contribution (*41a* transition).

Each curve corresponds to one pane of the gait time history plot. The high stride frequency curve (SF = 2.94 s^{-1}) has the shortest time duration. The total change in energy of the system (TE) (also the total work) is the highest of all four sampled values (TE = 419.67 J). This coupled with the short stride length results in a high CoT value (0.71). From the fractional energy plots, the large contributions of the *41a* and *34* transitions are evident. These are reflected in the kinetic energy plot, with the system accelerating to the start of the rear stance phase and then decelerating to the start of the extended flight phase. The acceleration / deceleration caused by the large amount of reconfiguration happening in a short time span is driving the high energetic cost of this gait.

The final set of bar plots in Fig. 4.11 displays the change in translational and rotational kinetic energies at the *34* transition (bar plots on the left) and at the *41a* transition (bar plots on the right). The bar plots are organized by limbs, with the abbreviations standing for the lower hind leg (LHL), upper hind leg (UHL), torso (T), upper fore leg (UFL) and lower fore leg (LFL). The trends are similar across all stride frequencies- the lower hind leg, upper hind leg and torso have velocities closing the body, while the upper fore leg and lower fore leg are opening up, moving away from the ground. Although the rotational change in kinetic energies are much smaller in magnitude than the translational, some of the rotation of the bodies is tied into the translational energies. The sum of each bodies' translational and rotational change in kinetic energies are then summed over all bodies to give the total work for that particular phase. This value is found to the right of the corresponding legend entry.

Returning to the discussion on the high stride frequency (SF = 2.94 s^{-1}), the lower fore leg at the *34* transition is moving much quicker than the other limbs, driving the high energy value (TE = 128.46 J) in this transition. At the next transition, *41a*, the deceleration of the lower fore leg is driving the high energy value (TE = -206.60 J). The change in the kinetic energy plot shows this on a global scale, while the bar plots show the limb or limbs responsible for the high energetic cost.

The middle two stride frequencies (SF = 1.38 s^{-1}, SF = 1.65 s^{-1}) show the flatter profiles necessary for a low CoT. As the change in the velocities at the transitions become smaller, the discontinuities in the kinetic energy plot are reduced. If the acceleration / deceleration of the limbs is properly balanced, the total change in energy is reduced. For the value nearest the ideal stride frequency (SF = 1.38 s^{-1}), the total energy at the *34* transition is very small (TE = -3.15 J). At the *41a* transition, energy needs to be injected to get the system airborne, although at all stride frequencies, the change in kinetic energy is negative, reflecting a slowing of the leg rotations.

At the other end of the stride frequency spectrum (the lowest stride frequency, SF = 0.92 s^{-1}), the energetic costs are driven by the *23* and *34* transition. In the *23* transition, the primary body driving the change in the kinetic energy is the torso. The changes are driven by the rotation from nose down to nose up, the large vertical / horizontal motions associated with the leaping body into the gathered flight phase, and the subsequent deceleration into the rear stance phase.

Although the gait discovered may not be the absolute global optimum, it represents an energetically efficient trajectory with minimal velocity changes across the transitions. The high and low stride frequencies demonstrate the issues at the extents from the high speed necessary for the rear stance phase at SF = 2.94 s^{-1} to the large amount of energy required to accomplish the very long gathered flight phase at SF = 0.92 s^{-1}. The best balance between velocities occurs between the end of the long gathered flight phase and the start of the rear stance phase in the gait at SF = 1.38 s^{-1}.

4.1.11 Best Cost of Transport

Fig. 4.12 displays the best possible CoT values as a function of speed across the range of stride frequencies investigated. These values occur between stride frequencies of 1.2 and 1.45 s^{-1}. The increase in the CoT at the very low stride frequencies is due to the increased impulsive torques. These start to increase below a stride frequency of 2 s^{-1}, although the CoT doesn't start to increase until a lower stride rate because of the linear change in the stride length with decreasing stride rate, delaying the CoT increase.

However, as discussed previously in Sect. 3.1.8.1, there is a biological limitation imposed on the system. Setting a peak maximum vertical impulsive force of 50 N·m·s and using a linear interpolation from the data, these impulsive-force limited CoT values are included in Fig. 4.12, designated by the red circles in the plot (listed as "Fit" data in the legend). The new values shift up, indicating an increase in the physically acceptable CoT. In general, the CoT is parabolic, with a minimum at 6.5 m/s, becoming more costly with

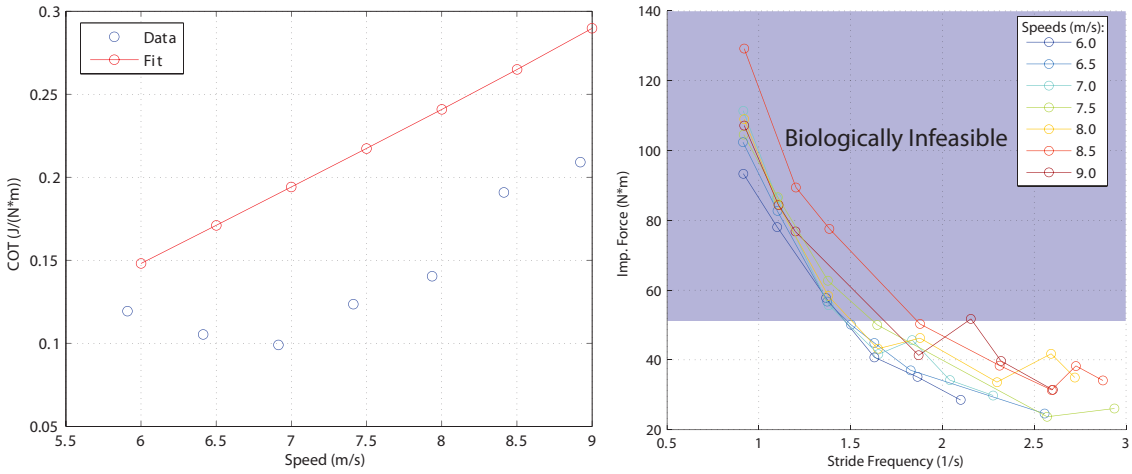

Figure 4.12 Best cost of transport values as a function of speed

higher speeds, driven by the increase in the maximum impulsive torque. Using the data fit[1], the trend is linear with respect to speed.

In summary, the rigid system favors a low stride frequency at all speeds to minimize the cost of transport, until the impulsive torques increase faster than the decrease in stride length. The rear stance phase drives the higher energetic cost at the high stride frequencies and the transitions before and after the gathered flight phase dominate at the low stride frequencies. The system is best suited for lower speeds and lower stride frequencies, within the bounds of reasonable impulsive force values.

4.2 Results: Articulated Model

The articulated system was simulated using Matlab with an evolutionary algorithm for the optimization. Simulations were conducted to first find a reasonable gait, and secondly, to optimize the gait. The results of these simulations are presented, focusing on the relationships between speed, stride frequency and cost of transport (CoT).

The gait is broken down into parts based on their energetic contribution. These parts have either an impulsive (transition) or active torque (stance phase) component, contributing to the total work of the system.

- ***41a***: Transition from the rear stance phase to the first half of the extended flight

[1]Parabolic fits were created for the stride frequency / impulsive force relations and the corresponding stride frequency for an impulsive force of 50 N·m·s was interpolated. This value was then used in the parabolic fit for the stride frequency / CoT data to find the expected CoT value.

phase.

- ***1a1b***: Transition at mid-flight.
- ***1b2***: Transition from the second half of the extended flight phase to the front stance phase.
- ***2***: Front stance phase (active torque during forward stance phase).
- ***23***: Transition from the front stance phase to the gathered flight phase.
- ***34***: Transition from the gathered flight phase to the rear stance phase.
- ***4***: Rear stance phase (active torque during rear stance phase).

These transitions and stance phases are shown in Fig. 4.13, with each colored configuration representing one of the states described above.

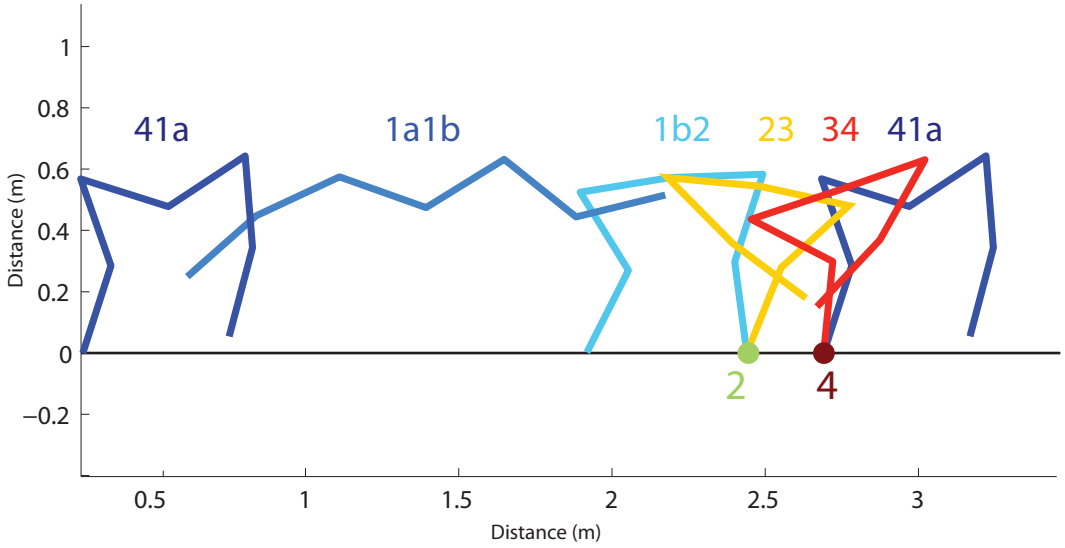

Figure 4.13 Phase transitions and stance phases of the articulated models' gait

4.2.1 Cost of Transport

Fig. 4.14) presents the optimized results of the speed and stride frequency trials for the articulated system. The speed and stride frequencies investigated range from 6.0 m/s to 9.0 m/s and 2.2 s^{-1} to 4.5 s^{-1}, respectively.

For the range of speeds and stride frequencies investigated, the articulated system shows a minimum in the stride frequency range of 2.8 to 3.3 s^{-1}, close to the biologically favored 2.83 strides/s (54) for systems of a similar size. The system showed better convergence characteristics at the higher stride frequencies and faster speeds, compared to the rigid model. The following subsections provide detailed analyses of the mechanisms associated with the CoT variations.

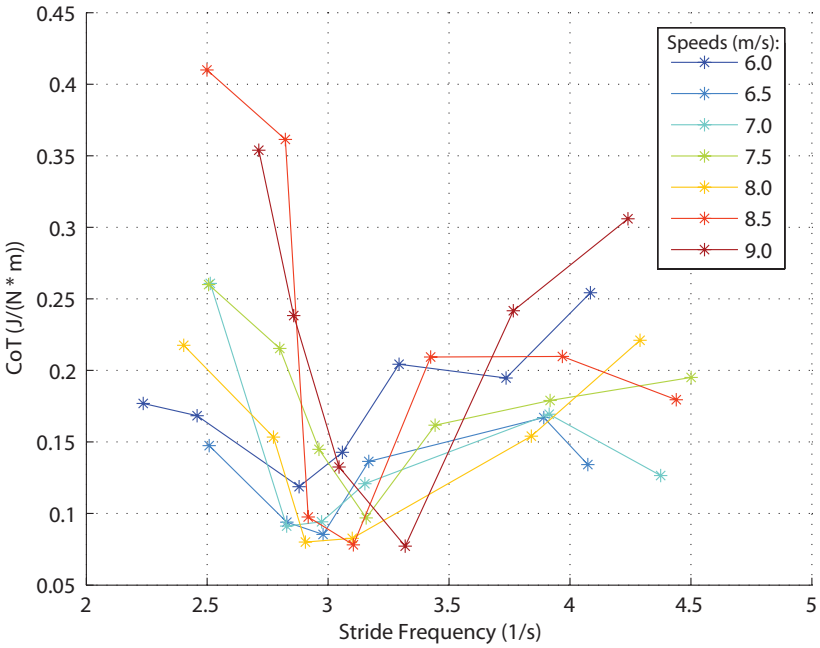

Figure 4.14 Cost of transport as a function of stride frequency

4.2.2 Total Work

The total work is the absolute value of the sum of kinetic energy changes of all bodies across the impulsive transitions and stance phases (Eqn. 4.1) and is proportional to the CoT.

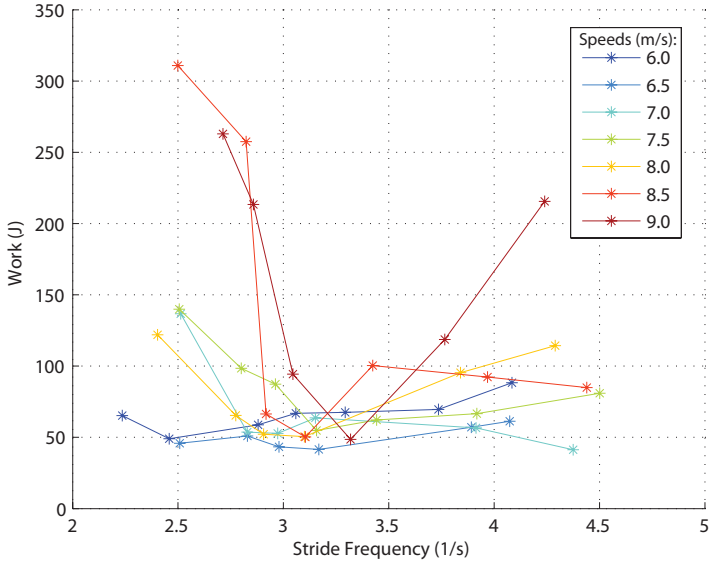

Figure 4.15 Total work as a function of stride frequency

Fig. 4.15 shows the relationship of the stride frequency to the total work of the system. The total work is flatter than the CoT plot with the exception of speeds 8.5 and 9.0 m/s. The majority of the total work contribution is attributable to the deceleration over the duration of the rear stance phase. Other trends are present but are related more to the shape of the gait, rather than speed or stride frequency relationships. As such, they will be addressed in the following subsections.

4.2.3 Maximum Impulsive Forces

Fig. 4.16 displays the maximum value of the vertical impulsive force for all simulations and all phases.

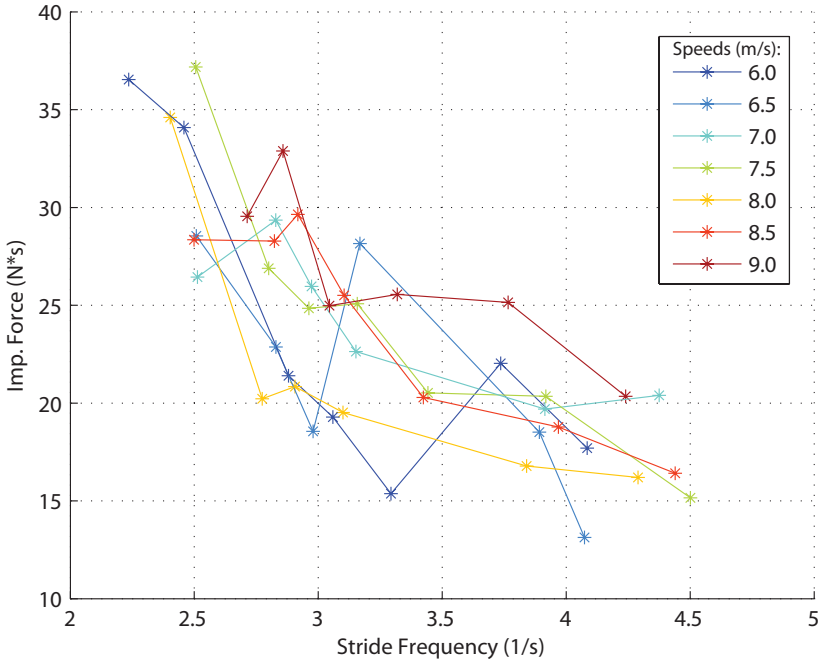

Figure 4.16 Maximum vertical impulsive force across all phases and joints

The points are fairly scattered but the general trend is a decreasing vertical impulsive force with increasing stride frequency. The shorter the stride length, the shorter the flight phases and the less amount of propulsion necessary to get the body into the air. The shorter stride length also provides a better range for the foot placement, to balance the transitions between phases.

4.2.4 Maximum Impulsive Torques

The impulsive torques, along with the impulsive forces, are transitioning the body between phases by instantaneously adjusting the velocity at the joints. The maximum absolute value of impulsive torques across all phases and joints are shown in Fig. 4.17.

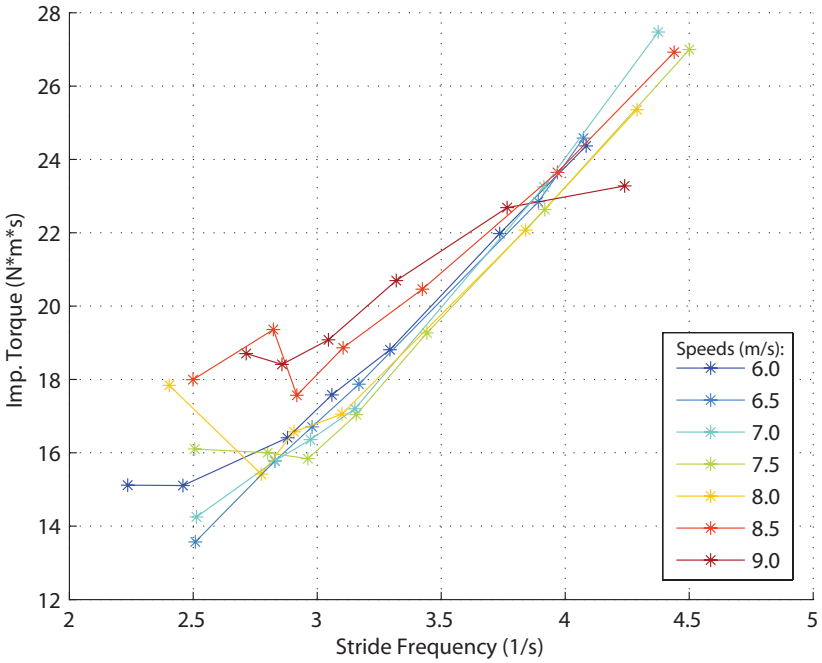

Figure 4.17 Maximum impulsive torques across all phases and joints

Very nearly all of the speeds collapse onto a single line with a slope of 7, increasing with increasing stride frequency. All of these values are from the back joint with the majority of the maxima occurring at the front stance to flight transition (*23*). It is only at stride frequencies greater than 3.75 s^{-1} that the maximum back torque occurs at the mid-flight transition (*1a1b*). At these very high stride frequencies, the stride length is shorter, and consequently, the flight phases are shorter. With the short flight phase and the body still opening up at mid-flight, the back torque reaches a maximum. Imagine doing a jumping jack- there is not enough room for the body to have a more gradual increase to its fully extended position and both legs are swinging up and out. The large mid-flight back torque prevents the back from collapsing.

At stride frequencies less than 3.75 s^{-1}, the *23* transition is driving the maximum back torque. The functionality is the same, just with the gathered flight phase. During this phase, the rear leg is crossing over the front leg, however, the back stays relatively flat. The large torque just before this phase is preventing the system from collapsing as the haunch pushes the rear leg forward to plant it for the rear stance phase. In both cases, the back torque is

acting like a contracting abdomen muscle rather than a flexing back.

4.2.5 Impulsive Torques by Joint

Fig. 4.18 presents the scatter of the impulsive torque magnitudes as a function of stride frequency for the back, haunch and shoulder joints. The other joints are not included since the torques are smaller and are relatively constant across stride frequencies (5 N·m·s or less). The colors represent the speed and the symbols signify the phase transition.

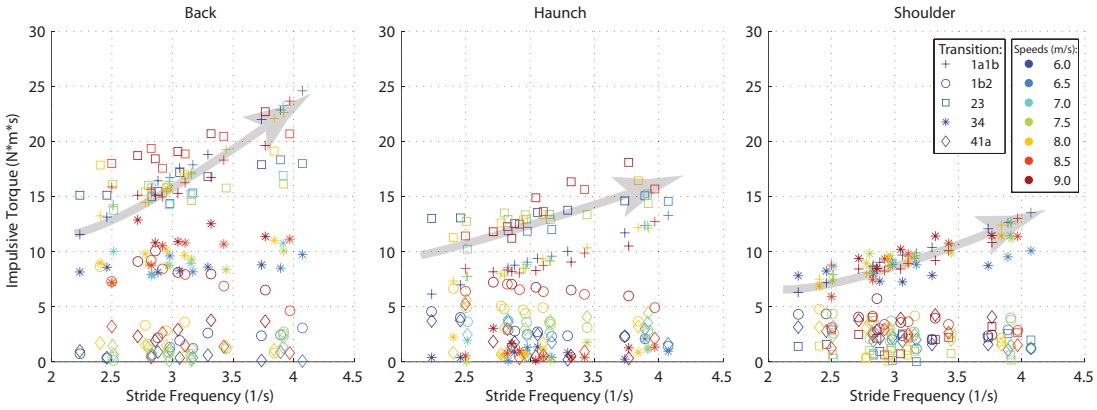

Figure 4.18 Impulsive torques at the back, haunch and shoulder joints for each transition as a function of stride frequency

The maximum torque is in the back joint for every simulation. The two phases clustered together at these maximum values are the mid-flight transition (*1a1b*) and the front stance to gathered flight transition (*23*). Although the absolute values of the torques are displayed, both of these back torques are similar to the contracting of the abdomen rather than the flexing of the back. At the lower stride frequencies, the *23* transition is higher, but switches to the *1a1b* transition at the higher stride frequencies (based on the clustering). Overall, the cluster of values is increasing with higher stride frequencies. The other transitions for the back are also banded, but remain relatively constant.

The next highest joint is the haunch, with the maximum occurring in the *23* transition, followed by the *1a1b* transition. Both of these bands are growing with increasing stride frequency, showing a similar trend to the back joint. This seems to indicates that the back and haunch are working synchronously to make the necessary adjustments to meet the initial velocity requirements of the next phase. All other transitions (*1b2*, *34* and *41a*) show a decreasing trend with increasing stride frequency.

The high torques at the *23* transition in the back and haunch joints are caused by the launch into the gathered flight phase. The back is fairly flat during this phase, flattening

out during the forward stance phase. The activation of both joints implies a synchronicity between similar muscle groups- the back torque is acting to prevent the back from collapsing and the haunch is pushing the rear leg over the front leg to get ready for the rear stance phase.

The shoulder torque is not as high as the other two joint torques and its highest cluster of values are the gathered flight phase to rear stance transition (*34*) and mid-flight transition (*1a1b*). Both groups are increasing with increasing stride frequency. All other transition torques are decreasing with increasing stride frequency. The higher values of the shoulder in the *34* transition are due to the rear stance reconfiguration in preparation for the launch into the extended flight phase.

The back, haunch and shoulder are all highly active during the mid-flight transition (*1a1b*). With the articulation in the back, the system can easily collapse on itself if the torques are not properly balanced. At the rear stance to extended flight transition (*41a*), the body begins to open up, the rear leg opening with respect to the hip and the front leg opening with respect to the shoulder. With both legs opening for the body to reach its full extension, the two halves of the back are quickly collapsing towards each other (think of the letter 'V' collapsing to the letter 'I'). At mid-flight, to prevent this motion continuing through the second half of the phase and to begin bringing the rear and front legs back underneath the body, a very large torque at the back joint is necessary, followed by large, albeit smaller, torques in the haunch and shoulder. All three of these large impulsive torques are preventing the legs from swinging beyond the realistic limits of the joints and the back from collapsing in on itself.

4.2.6 Gait Time History

To visually inspect how the gaits differ across the range of stride frequencies, a representative speed of 7.5 m/s is investigated. The gaits for all other speeds are similar. Fig. 4.19 shows a range of stride frequencies to better illustrate how the system is behaving by capturing a single frame after a δt, creating a time / position history of the system in a single image. The figures are zeroed to the hip location at the top of flight.

The extended flight phase is the dominant portion of this gait. There is very little change in the overall structure of the gait, with the majority of the stride frequency variation accomplished through the foot placement rather than any significant changes in the angular orientation of the limbs.

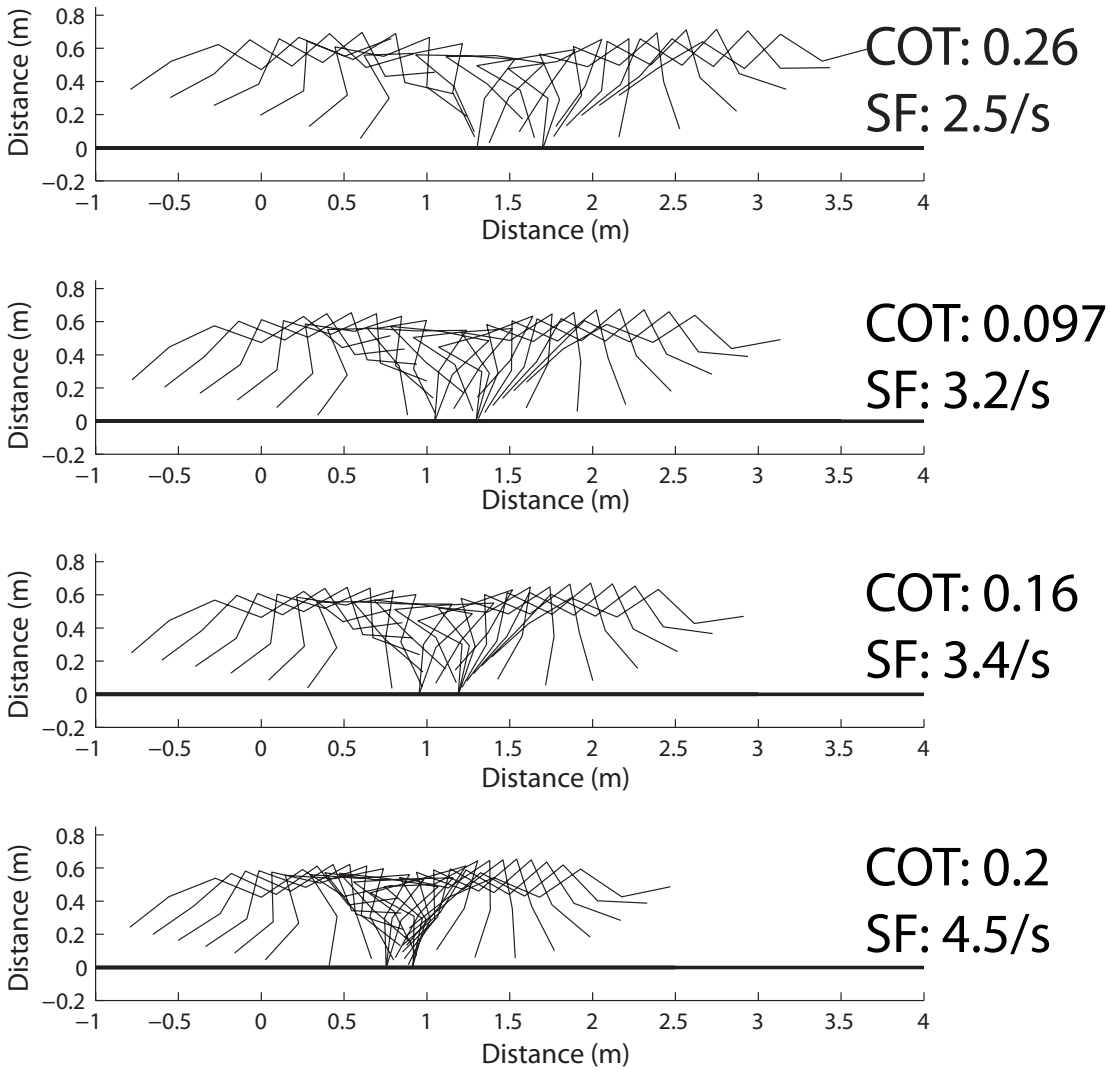

Figure 4.19 Stick figure plots of 7.5 m/s

4.2.7 Fractional Energy Plots

The impulsive torques for each transition and the active torques during stance phases are plotted as a fraction of the total change in energy for all speeds and stride frequencies in Fig. 4.20. The offset piece in each subplot represents the phase with the maximum contribution to the total change in kinetic energies.

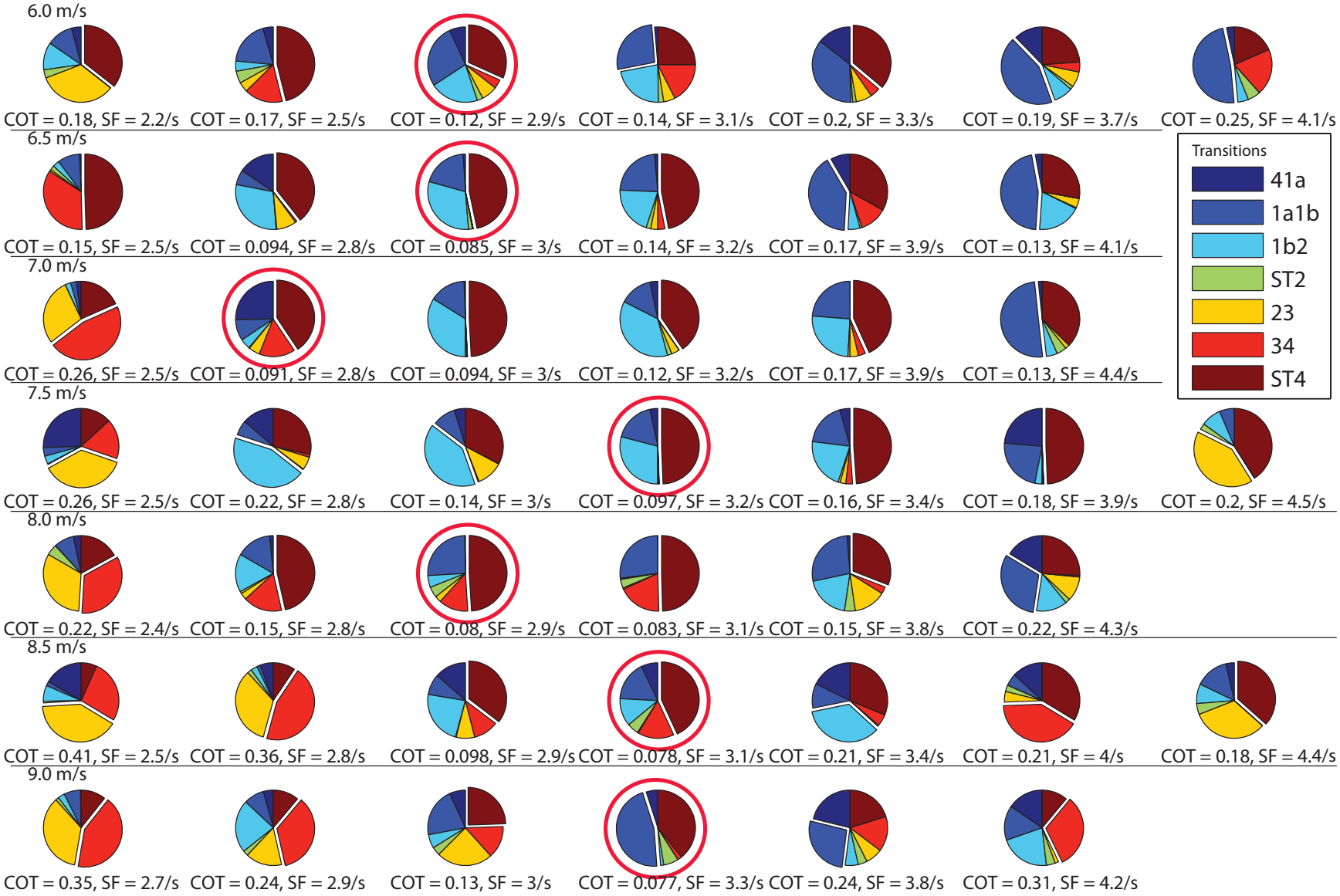

Figure 4.20 Fractions of energy changes for all speeds and stride frequencies, with red boxes denoting minimum CoT for each speed

The major component of the fractional energy for the minimum CoT values is the rear stance phase. From a biological viewpoint, the expected phase for the majority of the energy contribution would be the *41a* transition- the beginning of the launch into the extended flight phase. Although many of the articulated simulations have the rear stance phase as the primary contributor to the total work, rather than having all of the power at the pre-launch transition and relying on the flight phase to accomplish all the reconfiguration, the phase leading up to the launch (Phase 4) and the articulation provide the necessary mechanisms to match the desired speeds to propel the system into flight. The transition from rear stance to flight is very efficient, closely matching the speeds at the end of the stance phase to those necessary for the extended ballistic trajectory.

4.2.8 Potential and Kinetic Energy

The changes in potential energy (*PE*) and kinetic energy (*KE*) are plotted in Fig. 4.21. The plots are zeroed to the start of the extended flight phase.

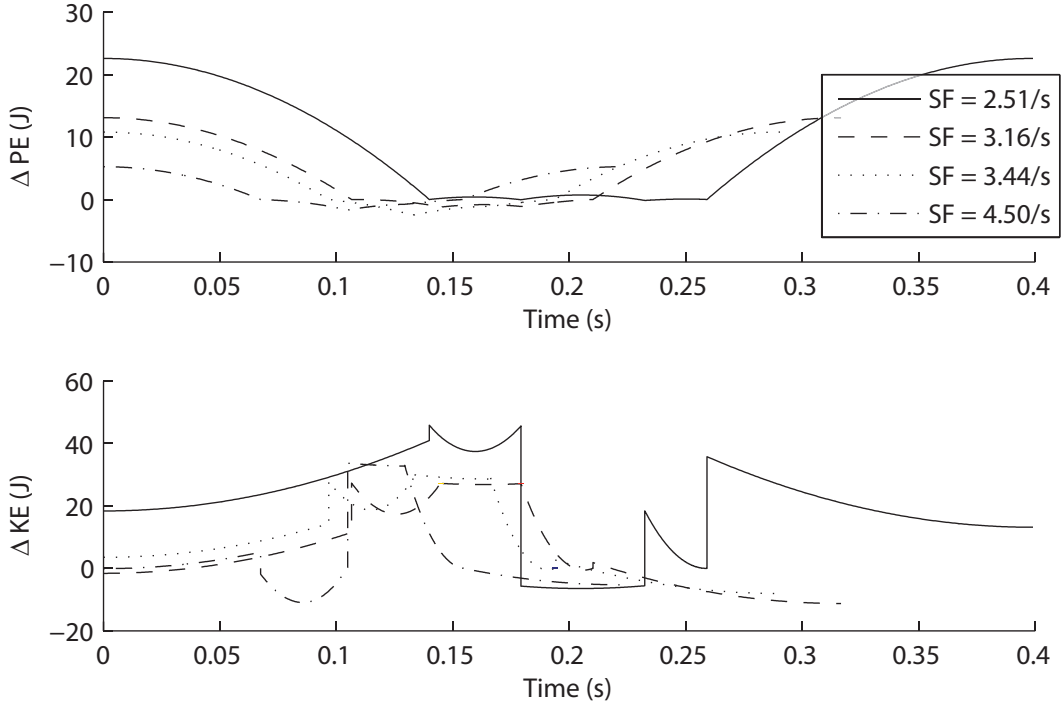

Figure 4.21 Change in *PE* and *KE* over the total time of one gait cycle

The first plot shows the instantaneous potential energy of the system. With increasing stride frequency, the center of mass trajectory decreases in amplitude, correlating to the reduction in the maximum impulsive force with increasing stride frequency. As a general

observation, the extended flight phase takes up the majority of the total time for a single stride with a 25% / 75% between stance and flight phases.

The change in kinetic energy will be discussed in more detail in the next section. The plot shows the change in the sum of the translational and rotational kinetic energies at any instant in the stride cycle.

4.2.9 Kinetic Energy in Detail

The plots in this section detail the kinetic energy changes, starting with the instantaneous kinetic energy change, the fractional energy charts, and the translational kinetic energies of the individual bodies at 6.0, 7.5, and 9.0 m/s.

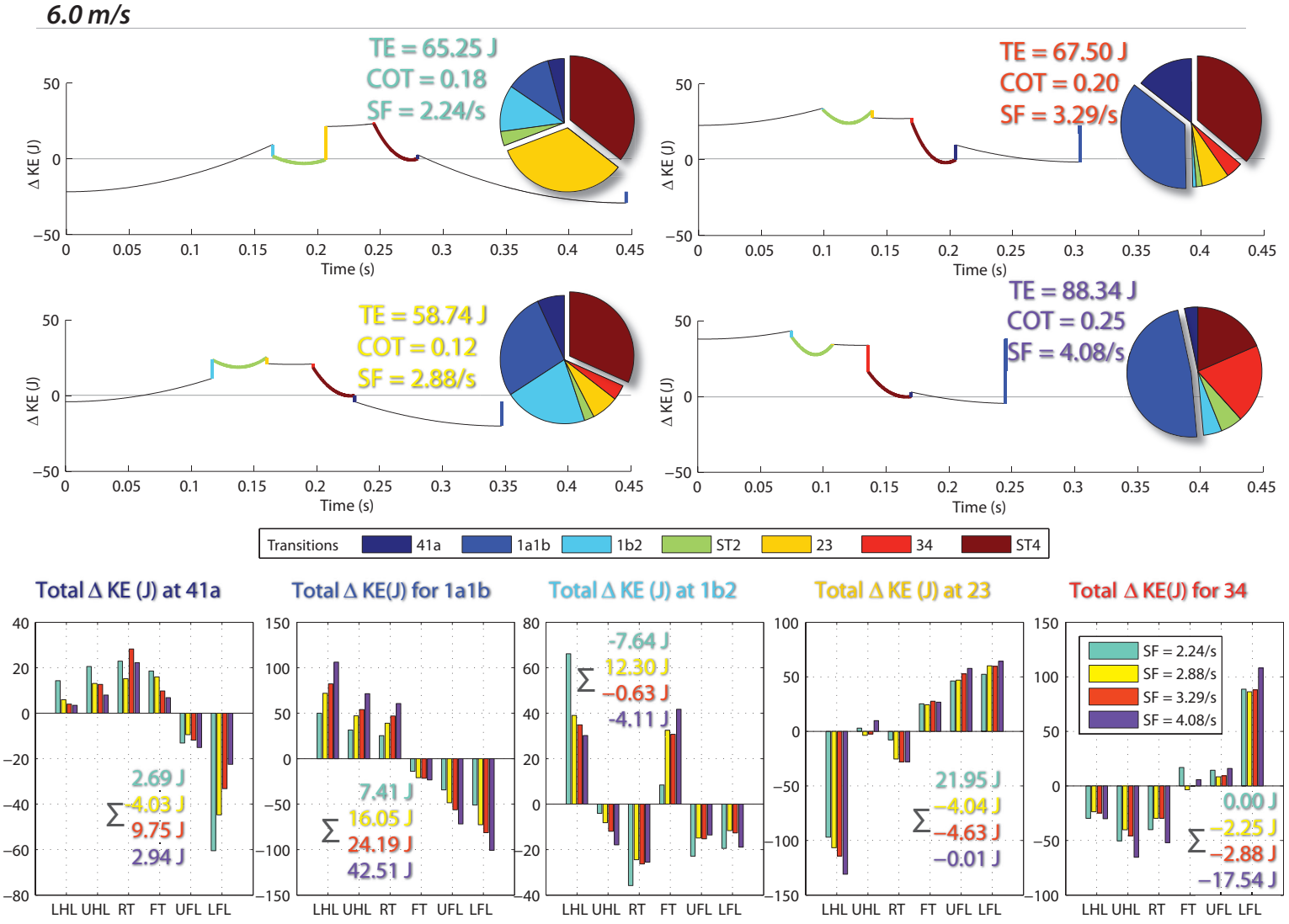

Figure 4.22 Kinetic energy changes in detail for 6.0 m/s

The initial speed scrutinized is 6.0 m/s in Fig. 4.22. The first plot on the page shows the change in kinetic energy. The colored overlays correspond to the transitions and stance phases. At the lower stride frequency (2.24 s^{-1}), the system accelerates from the front stance into the gathered flight phase, followed by a deceleration over the rear stance phase. These accelerations / decelerations constitute the majority of energy changes increasing the total work.

The pie charts next to the kinetic energy time history plots display the fractional energies of the observed stride frequencies. At the highest stride frequencies, the mid-flight transition dominates. This correlates to the contraction of the abdomen to start bringing the extended limbs underneath the body. At the lower stride frequencies, the rear stance phase is prominent. Overall, it is an important feature in this gaiting methodology and is a driving cost in many of the optimized gaits. The time spent in front stance, gathered flight and rear stance are almost the same.

The final set of bar plots show the translational changes in kinetic energy for all of the transitions. The bar plots are organized by limbs, with the abbreviations standing for the lower hind leg (LHL), upper hind leg (UHL), rear torso (RT), front torso (FT), upper fore leg (UFL) and lower fore leg (LFL). The rotational kinetic energy changes are included only for the phase 4 stance phase (ST4), since for the other phases, they are small and tied in with the translational change in kinetic energies. The sums of the changes in both translational and rotational kinetic energies are included on the plot.

Besides the rear stance phase, the other transitions contributing to the energetic cost are the mid-flight transition for all bodies, the front stance to flight transition for the lower hind leg and the flight to rear stance transition for the lower fore leg. At mid-flight, the rear half of the body is not able to balance out the motion of the front half of the body, creating a large change in the velocities at mid-flight. These are also the most difficult to match since the impulsive torques are the only means available to adjust the velocities, whereas all other phase transitions have a set of impulsive forces to assist in adjusting the velocities.

The lower hind leg in the front stance to flight transition (*23*) in all stride frequencies is slowing down (even though it is crossing over the body during the gathered flight phase) because of the large amount of reconfiguration it goes through during the front stance phase. The low stride frequency has the most difficulty finding a balance between the velocities at this transition. The large haunch torque at the *23* transition acts to slow down the rear leg.

The lower fore leg in the flight to rear stance transition (*34*) is undergoing a large amount of reconfiguration, most noticeably at the highest stride frequency when the stance time decreases. The large impulsive torque at the shoulder is accelerating the leg outward from underneath the body in preparation for the launch into the extended flight phase.

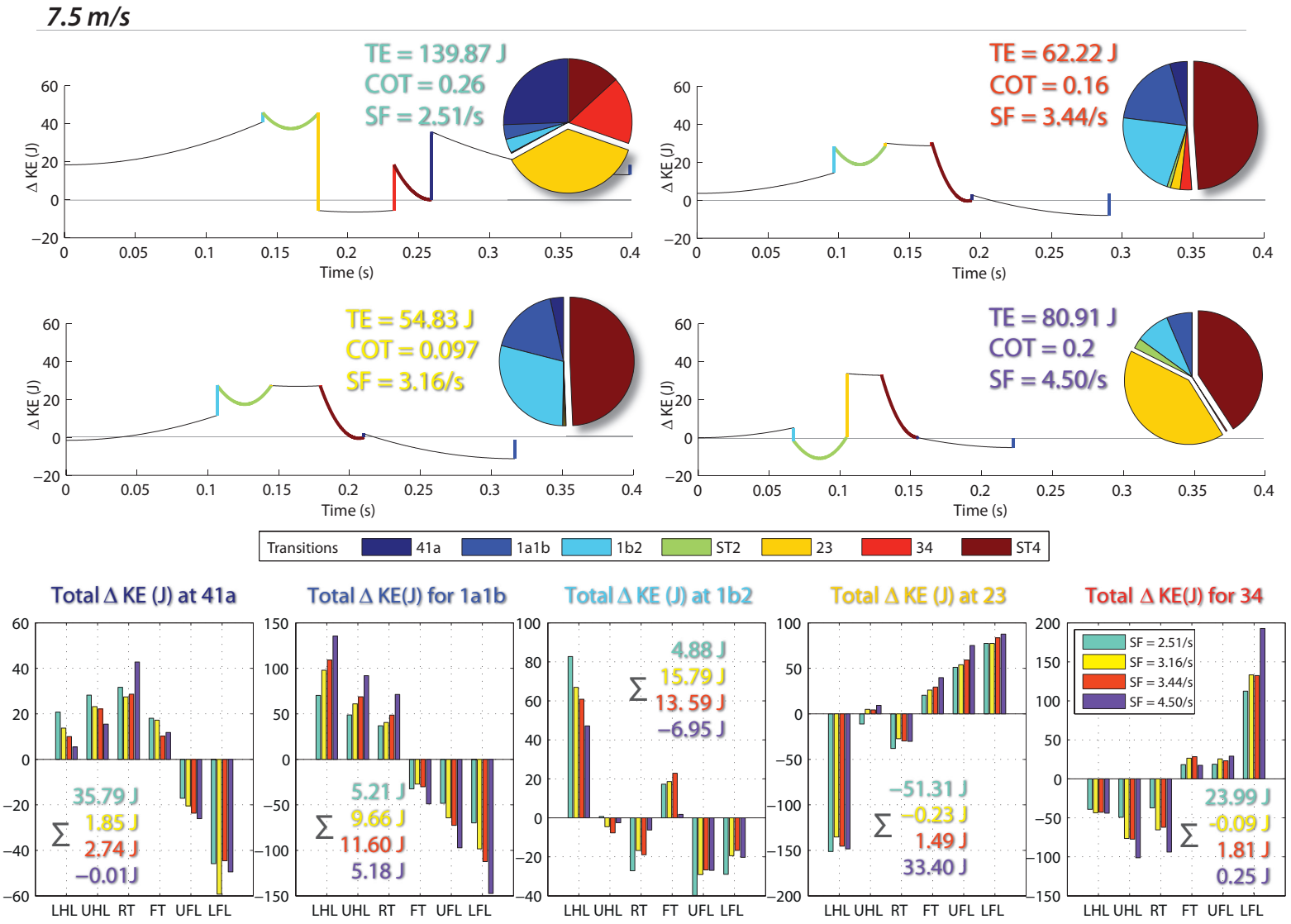

Figure 4.23 Kinetic energy changes in detail for 7.5 m/s

Fig. 4.23 presents a detailed analysis of the kinetic energy changes for 7.5 m/s. With the exception of the 2.51 s^{-1} stride frequency, the rear stance phase dominates. Walking through the stride frequencies individually can provide insight into the particular disjoints causing the higher energy costs.

At the low stride frequency, the *23* and *41a* transitions dominate the energetic cost. Much of this is tied in with the deceleration from the front stance phase into the gathered flight and the subsequent accelerations in the rear stance phase and stance to flight transition. The rest of the stride frequencies are heavily weighted by the deceleration in the rear stance phase.

The high cost at the lowest stride frequency is tied to the lengthening of the gathered flight phase. The system slows down when entering this phase. The better stride frequencies have a shorter gathered flight phase.

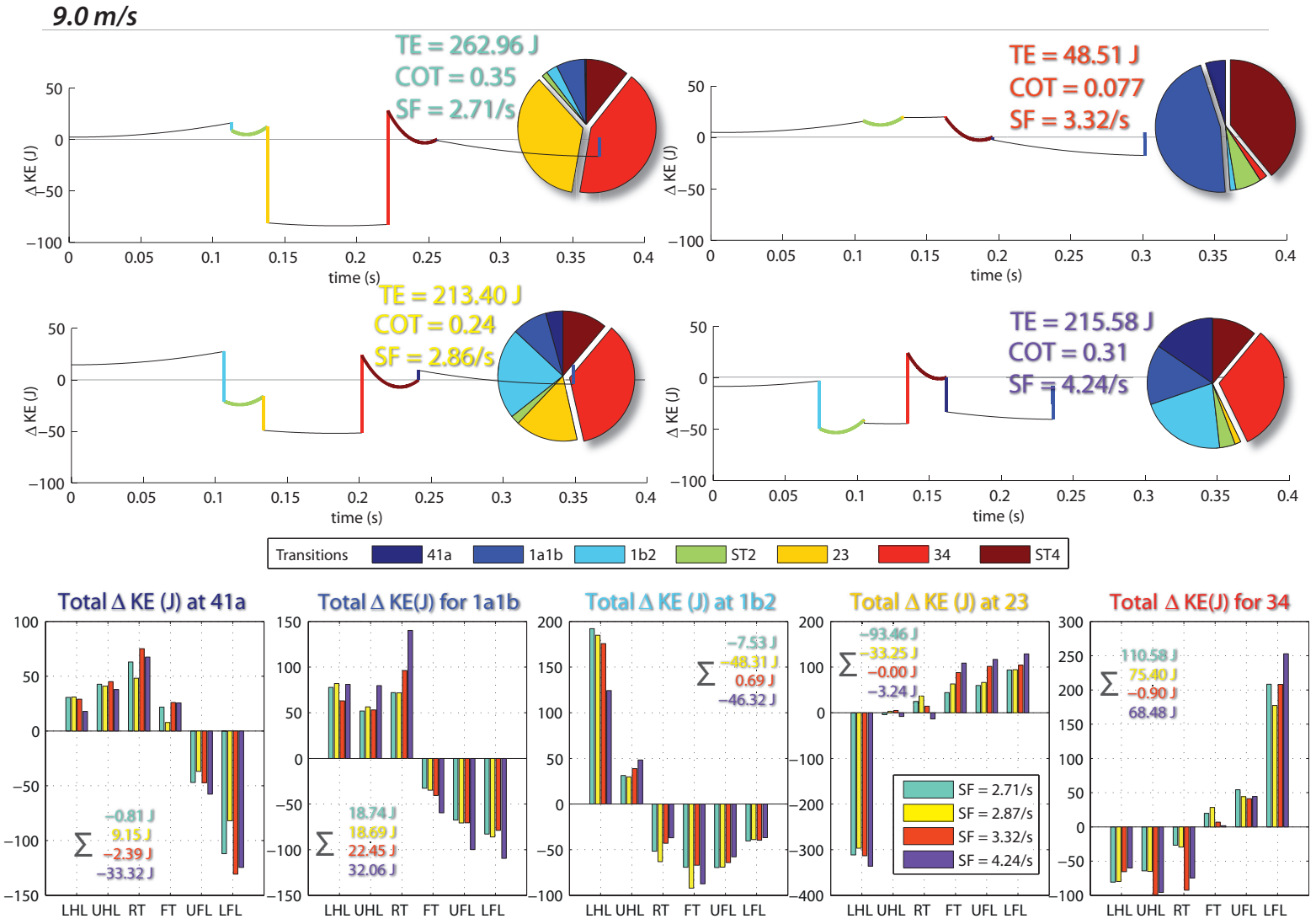

Figure 4.24 Kinetic energy changes in detail for 9.0 m/s

For the 9.0 m/s, the large energetic costs occur at several of the transitions, most following trends previously discussed. The poor velocity matching at the transitions (a lot of speeding up and slowing down between phases) is magnified at the higher speed, causing large discontinuities that drive up the total work value.

The majority of the total work at the low stride frequency features the *23* and *34* transitions, bracketing the slower gathered flight phase. The long gathered flight phase becomes more prominent at the high speed / low stride frequency as the system attempts to cover the dictated distance by increasing the flight phases. The system slows down substantially at the start of the gathered flight phase, and then has to reaccelerate for the last part of the total stride. The best value (3.32 s^{-1}) has a much shorter gathered flight phase, providing a better balance over the transition with less deceleration. This behavior worsens with the slower stride frequencies, as both flight phase durations increase.

4.2.10 Active Torques

The active torques are turned on during the stance and were initially put in place to keep the simulation in the stance phase for a longer period of time. For the initial set of optimizations, the active torques were set to a constant value (Sect. 3.1.9). Once acceptable solutions meeting the specified constraints were discovered, a clear trend began to emerge with the articulated fractional energies. The rear stance phase was continuously showing up as a dominant energetic cost.

After some initial experiments, it was clear that the active torques played a critical role in the energetics of the articulated system. Both the shoulder and haunch torque were tuned by hand to find a constant value that provided the system with better performance characteristics. The benefits of tuning the active torques is most visible at high speed. An example of one set of a converged set of optimized simulations varying the active torque is shown in Fig. 4.25 for 9.0 m/s.

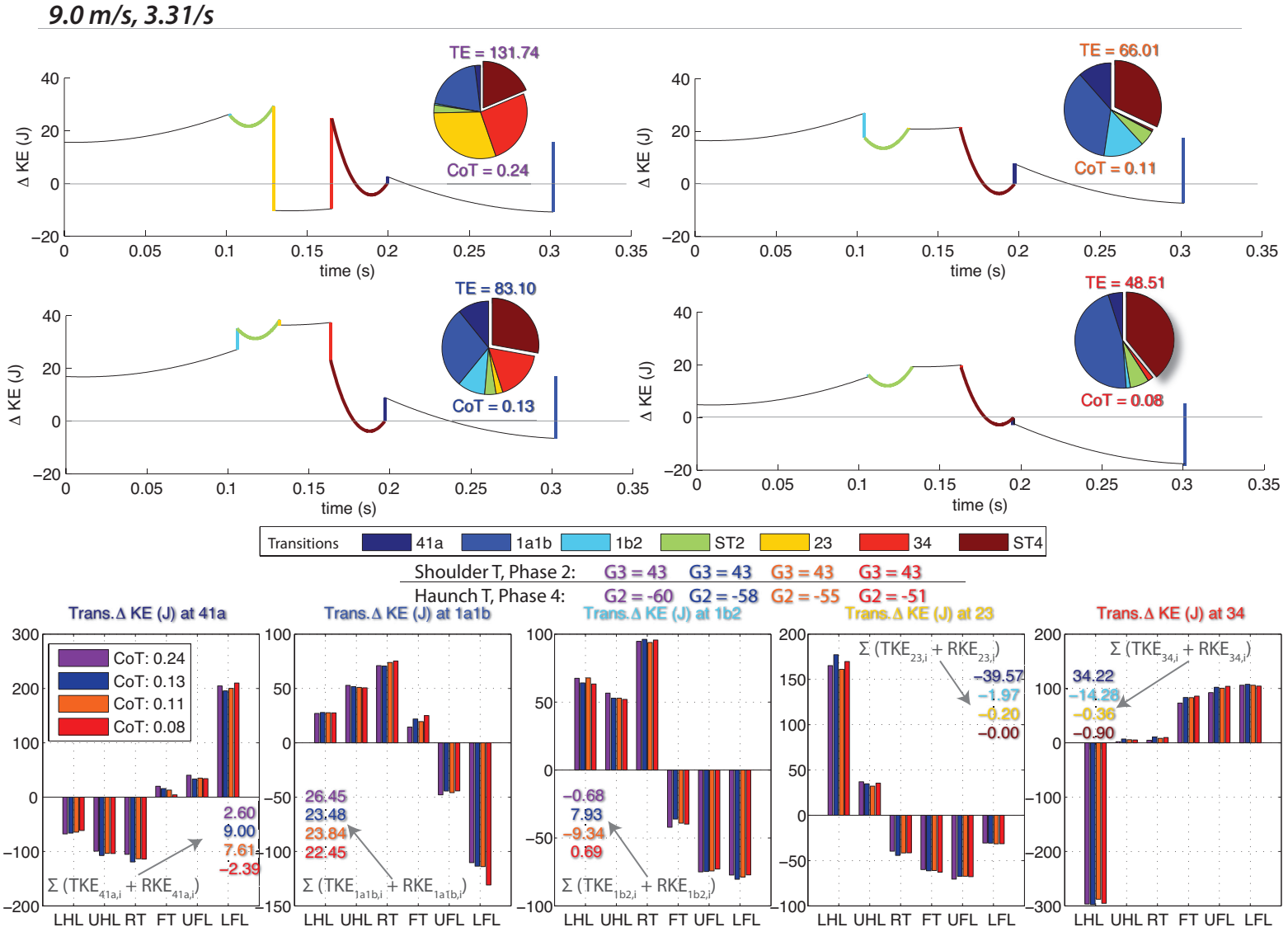

Figure 4.25 Kinetic energy details when varying active torques at 9.0 m/s

Overall, the shape and duration of all phases remains relatively constant over all trials. This is to be expected since the changes to the angular values are very small. The most noticeable difference in the kinetic energy plot is in the gathered flight phase. Using the largest haunch torque (60 N·m), the system decelerates upon entering the gathered flight phase. The first decrease of the haunch torque reduces the deceleration into the flight phase by a significant amount. After the initial drop, the other changes to the active torque fine tune the transitions.

The best torque match for the system reduces the *1b2*, *23* and *34* transitions to a nearly seamless matching of speeds over those transitions. At *1b2*, the loss of kinetic energy from the front half of the body (FT, UFL and LFL) is transferred to the rear portion of the body (LHL, UHL and RT) at impact. At the *23* transition, the back leg (LHL, UHL) is swinging across the front part of the body, getting ready to plant the rear foot for the *34* transition. At the rear foot plant, the momentum of the rear leg swinging through the front stance and gathered flight phases is transferred to the front part of the body, as the body starts to unfold itself in preparation for the extended flight phase. The closer to zero the sum of the change in torques is across the transition, the more efficient the transfer of energy between the bodies at impact / flight, reducing the total work of the system. The tuned values found here minimize these transitional changes quite effectively. Adjusting the active torques by less than 20% resulted in a three-fold decrease in the CoT.

4.2.11 Best Cost of Transport

Fig. 4.26 plots the best CoT value as a function of speed for all stride frequencies investigated. The scale of the plot ordinate skews the results slightly. As discussed in the last section, it is possible to nearly eliminate the change in kinetic energy associated with three of the phase transitions- *1b2*, *23* and *34*- through adjustment of the haunch torque. The 8.0 and 9.0 m/s plots confirm this, and the 8.5 m/s points in this same direction. From these observations, it may be possible to reduce the CoT values in the slower speeds, unless there is another constraint at these speeds such as a limitation on the foot placement at the lower speeds.

4.3 Comparison of the Rigid and Articulated Systems

Now that both models and their underlying trends have been addressed, a comparison between the two systems is made and the effect of the addition of the articulated spine on the

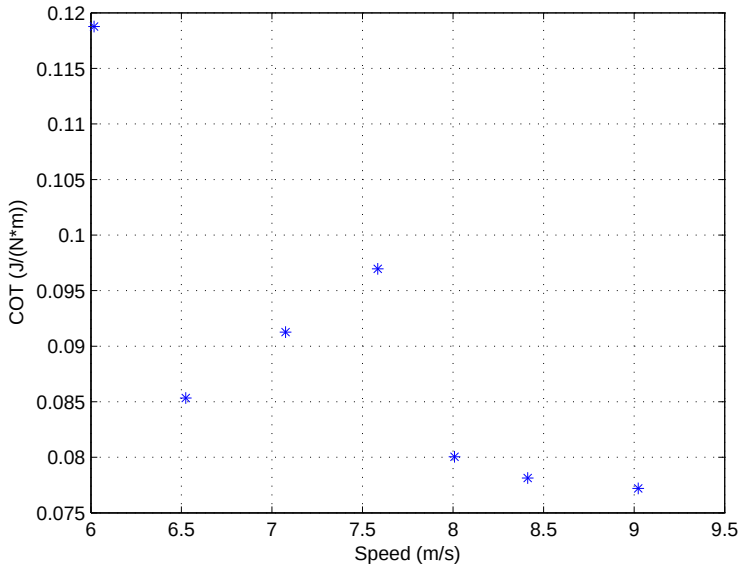

Figure 4.26 Best cost of transport values as a function of speed

energetics of the system is evaluated.

4.3.1 Best Cost of Transport

Fig. 4.27 overlays the best CoT values from the rigid and articulated models, as a function of speed. The optimal values for the rigid model occur at a stride frequency of 1.4 s^{-1}, while the articulated model favors stride frequencies between 2.8 to 3.3 s^{-1}. The CoT is proportional to the total work of the system and inversely proportional to the stride length. The rigid system takes advantage of this by using as large a stride length as possible, while the articulated favors a shorter stride length, reducing the maximum height reached during the flight trajectory while using the back articulation to achieve the necessary leg reconfiguration.

While each system found a minimal CoT for the various speeds investigated, there is a penalty to pay. In the rigid model, the vertical height of the center of mass increases with the longer stride length accomplished through a long gathered flight phase. The long flight phase drives up the impulsive forces. Such an increase can be detrimental to a system and, as discussed in Sect. 4.1.11, a biological limit is imposed, with the resultant CoT values shown in Fig. 4.27) as the gray circles connected by the line. Although the articulated system keeps its impulsive forces below the maximum values as suggested in the literature (Sect. 3.1.8.1), the maximum impulsive torques are much larger than those in the

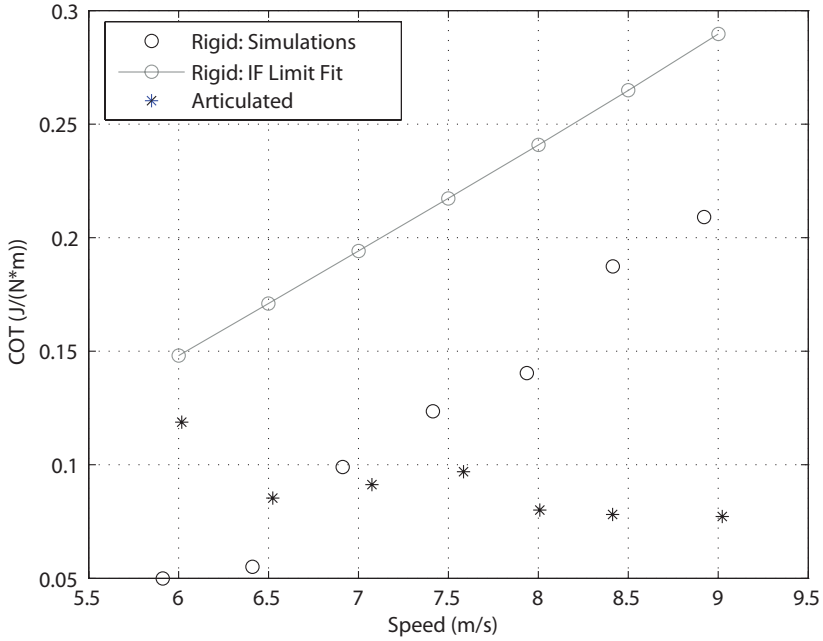

Figure 4.27 Best cost of transport values as a function of speed for both models

rigid system, all of which are related to the back (or more biologically correct, abdomen) torques.

4.3.2 Model Robustness

While less quantitative than other metrics analyzed, model robustness was a key tool in determining the favorable ranges for each system. This measure is related to the number of converged solutions passed on to the optimizer.

The number of feasible solutions for the rigid model at higher stride frequencies, obtained from the optimization methodology employed, was substantially smaller than the number of solutions obtained for the articulated model. Most solutions at new speeds or stride frequencies were found using the seed from a nearby speed or stride frequency. At the higher stride frequencies, the solutions did not converge and were therefore not pursued. At the opposite end of the spectrum, the low stride frequencies converged in less than 100 iterations.

The articulated model, with its extra degree of freedom, has a larger configuration space, allowing more opportunities for converged solutions, and later optimized gaits. The articulated optimization fell into three separate bands of solution. The first set of solutions had CoT values larger than the rigid converged solutions. After running the simulations at

increasing speeds, better foot placement was obtained for the articulated model. This set of solutions converged onto the best rigid values (second band of solutions). The third band came with the tuning of the active torques and dropped the high speed articulated values much smaller than the rigid. The same phenomenon witnessed with the rigid when running simulations at the higher stride frequencies, was also observed in the articulated when pushing the stride frequencies below 2.5 s^{-1}.

4.3.3 Gait Comparison

As discussed above, the rigid model favors low stride frequencies, while the articulated model favors high stride frequencies. To visually inspect the difference in the gaits at their preferred stride frequency, a time history of both the rigid and articulated gaits are presented in Fig. 4.28. The median speed of 7.5 m/s is presented as an example speed. The only significant difference in the configuration time histories at different speeds is the foot placement since the angles vary only slightly with speed.

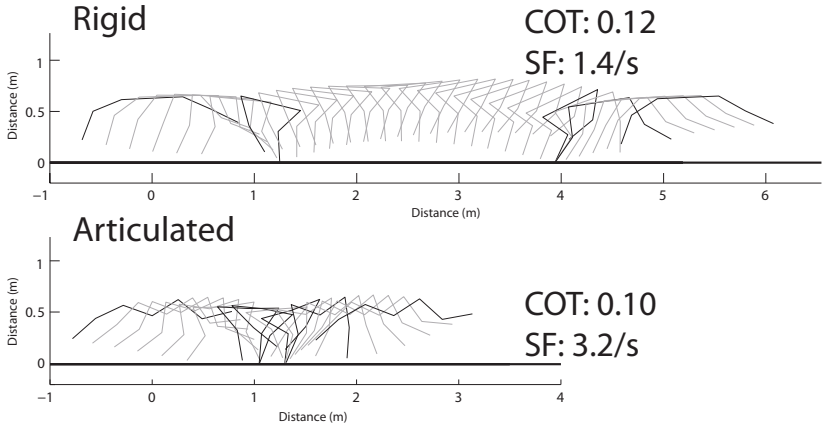

Figure 4.28 Time history of rigid and articulated model gaits at 7.5 m/s

The rigid model has a much longer gathered flight phase, traversing the long distance dictated by the low stride frequency. The articulated model, besides the angle in the back, differs primarily in its use of a very short gathered flight phase. The majority of the distance (small at the higher stride frequencies) is covered through the extended flight phase. Both choices correspond to the observed trends of the low impulsive forces at high stride frequencies and low impulsive torques at low stride frequencies.

4.3.4 Potential and Kinetic Energies

Comparison plots for the low (6.0 m/s), medium (7.5 m/s) and high (9.0 m/s) speed optimized values are presented in the figures below. The first plot, Fig. 4.29), compares the optimized values of the rigid and articulated models at 6.0 m/s. The total energy changes in the articulated model are only slightly larger than those for the rigid model (59 J versus 50 J), but the rigid model's CoT is less than half the articulated model's value. The long stride length makes up for the deficit. The interesting trend in the rigid model's change in kinetic energy curve is the very short stance phases, that are nearly matched to flight phases. The rigid model's potential energy curve looks like the trajectory of a pogo stick, similar to the gaiting of a kangaroo. The largest contribution to the energy is the mid-flight transition for the rigid. The articulated model follows similar trends as at other speeds, but the short stride length and slow speed count against the system.

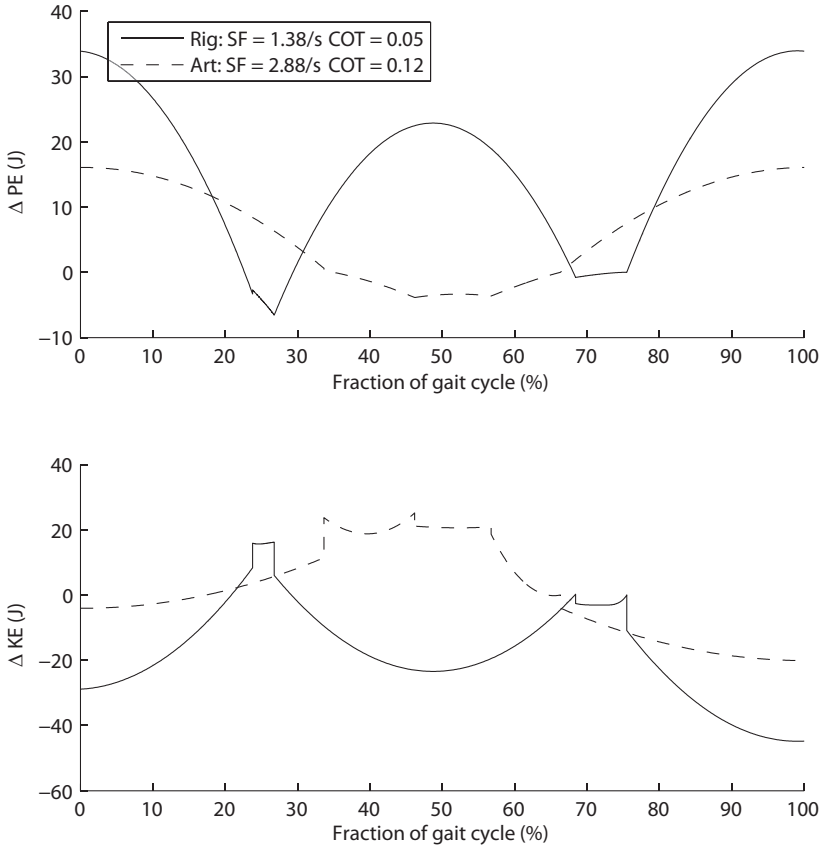

Figure 4.29 Instantaneous change in potential and kinetic energy for best gaits at 6.0 m/s

Fig. 4.30 corroborates the observations of the impulsive forces. The figure presents the instantaneous changes in potential and kinetic energies as a fraction of the total gait cycle for the optimized gaits of the rigid and articulated models at 7.5 m/s.

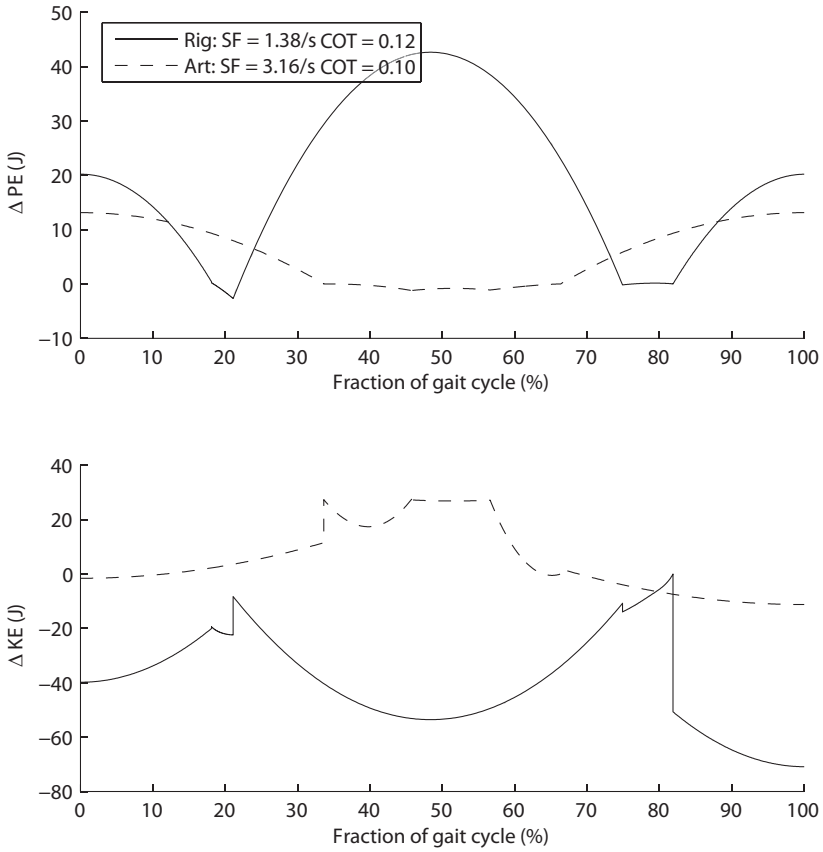

Figure 4.30 Instantaneous change in potential and kinetic energy for best gaits at 7.5 m/s

As shown in the time history of the gaits, the center of mass has a much lower trajectory at the high stride frequency (articulated model) than that of the low stride frequency (rigid model). The large change in the potential energy of the center of mass over the stride cycle for the rigid is responsible for the large vertical impulsive forces. The forces are necessary to enable the system to leap into the air.

The second plot presents the change in the kinetic energy over the fraction of the stride cycle. The rigid model (solid line) has a much shorter set of stance phases (as a fraction of the total time). The system accelerates at the start of the gathered flight phase, necessary to cover the long distance, then accelerates through the rear stance phase. This phase has the largest angular change and a short amount of time to complete it. The system slows down at the start of the extended flight phase. If the system was able to take advantage of the energy from the rear stance phase, the transition would be more efficient.

The low total work values for the articulated model stem from the better foot placement options provided by the joint in the back. The additional degree of freedom in the spine allows for smoother transitions without the sharp increase or decrease at the junctions be-

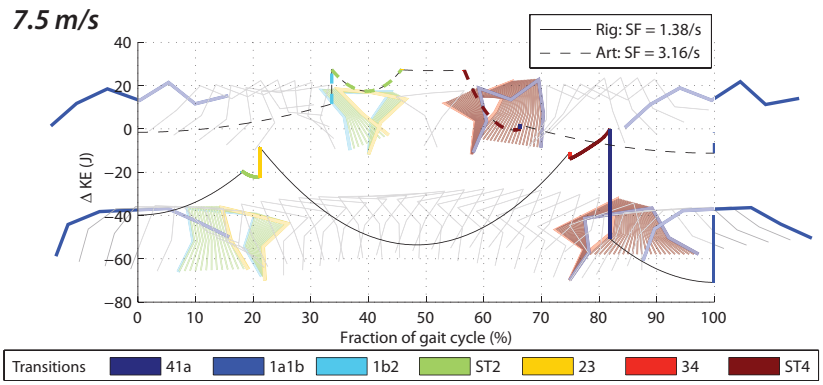

Figure 4.31 Instantaneous change in kinetic energy for best gaits at 7.5 m/s

tween phases, shown by the vertical lines on the Δ KE plots. Fig. 4.31 shows the details of the instantaneous change in kinetic energy plots for the medium speed simulated. The stick figure representation of the rigid and articulated gaits are overlaid on the plot to provide visual correlation between the gait and the change in kinetic energy. Starting from the beginning of the cycle, both models are accelerating during the second half of the extended flight phase. The rigid model has no discernible change at the *1b2* transition, showing a very efficient transfer of the energy between the extended flight and front stance phases. On the other hand, the articulated system has to increase the energy for the front stance phase due to the large amount of angular reconfiguration that occurs in this phase. The change over the stance phase is not significant for either model, although the articulated model spends more time in the front stance phase than the rigid model. The primary difference between the systems becomes evident during the gathered flight phase, however little change is necessary at the *34* transition for either model. The articulated system is decelerating from the start of the rear stance phase to the start of the extended flight phase and the rigid is accelerating. While the front stance phase had the largest reconfiguration for the articulated model, the rear stance phase has the largest amount of reconfiguration for the rigid model. As such, the transition between the rear stance and extended flight phases is very inefficient due to the deceleration necessary after the increase in energy needed to move the system through the angles in the short amount of time. Increasing the stance time or decreasing the angular change would both have benefitted the rigid model but seeds with solutions taking into account one or the other characteristic were either unusable gaits or energetically costly in some other portion of the gait.

The final figure, Fig. 4.32, presents the optimized values for the 9.0 m/s trials. The articulated model has a fairly flat change in kinetic energy profile, although, the large transitions of the rigid model alter the ordinate scale, compared to the previous plots at the

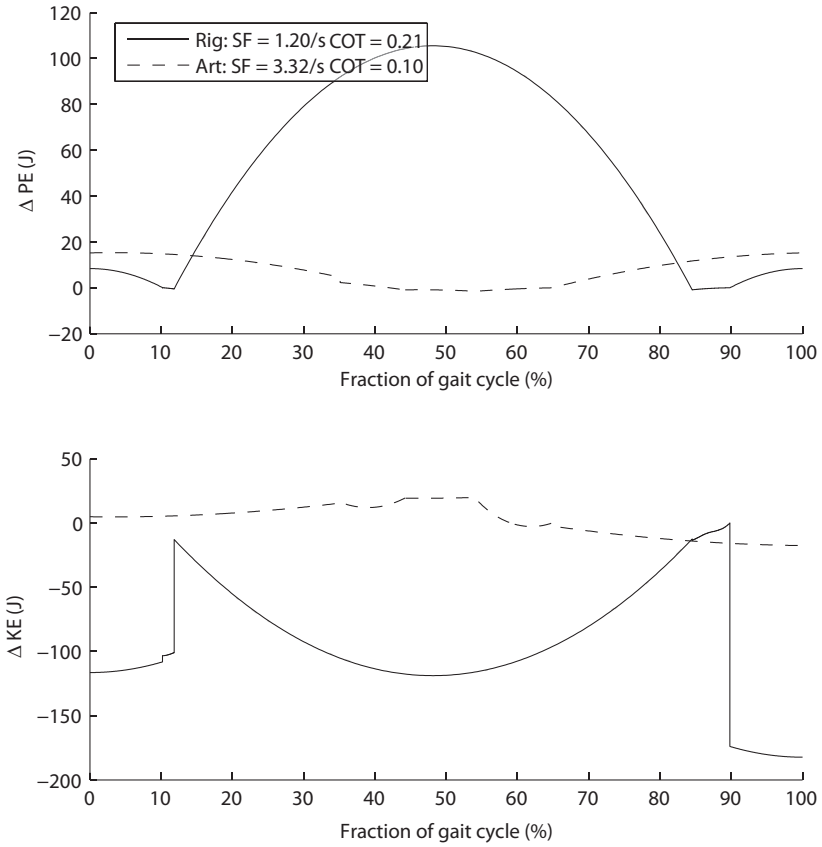

Figure 4.32 Instantaneous change in potential and kinetic energy for best gaits at 9.0 m/s

lower speeds. The transitions between the phases are very well balanced between the acceleration and deceleration of the limbs (Fig. 4.25). The rigid system's lengthy gathered flight phase (long flight phases overall, with only about 5% of the time spent in stance), is not well proportioned with the other phases. The system has to accelerate to cover the long distance, and then decelerate from the rear stance into the extended flight phase, another very costly transition with speeds that are poorly matched at the transitions. The articulated model is able to find a nearly seamless set of transitions over the full stride phase, displaying an efficient, high speed gait.

4.3.5 Final Recommendation

With all of the information provided in the sections above, the choice is clear: at high speeds, the inclusion of an articulating spine provides a reduction in the cost of transport by a factor of 2.5. The preferred stride frequency is more closely related to that favored by biological systems and the maximum vertical impulsive force is much lower than those for

the optimized rigid solution at the same speed.

Chapter 5

Conclusions and Future Research

The objective of this research was to develop models, conduct simulations, and compare the performance of two quadrupedal systems, similar in size to a medium sized dog, one with a rigid back and the other with a single node of articulation in the spine. Both systems were planar with equally distributed mass in the torso(s) and legs, employing frictionless pin joints and instantaneous impulsive transitions between the ballistic flight phases and active stance phases. The virtual leg concept was employed to simplify the analysis and to reduce the system from four legs down to two. The consequence of this simplification led to the high-speed gallop gait becoming a high-speed bound. The resultant motion mimicked the motion of a front-leg amputee canine, still able to run fast, despite its missing limb.

The results of the simulations are summarized below, conclusions regarding the analysis, discussion of the contributions of the work, lessons learned and future areas of exploration are listed.

5.1 Conclusions

Despite the simplicity of the model, the results confirmed the biological trends witnessed in nature. The contributions of an articulating spine to an animal's speed from Hildebrand (60) as evidenced in the simulations are addressed below.

Flight phase distance *As the swing of the limbs increases, the distance covered during the aerial phase is increased.* As the speed increases, the limbs of the body are moving faster relative to the center of mass, therefore the distance in flight increases. This is clear in both models and as speed increases, the duty factor decreases, indicating an increase in the flight duration.

Biarticular muscles *With the combination of spine muscles and limb muscles working concurrently, the limbs move faster than a single group of muscles working alone.*

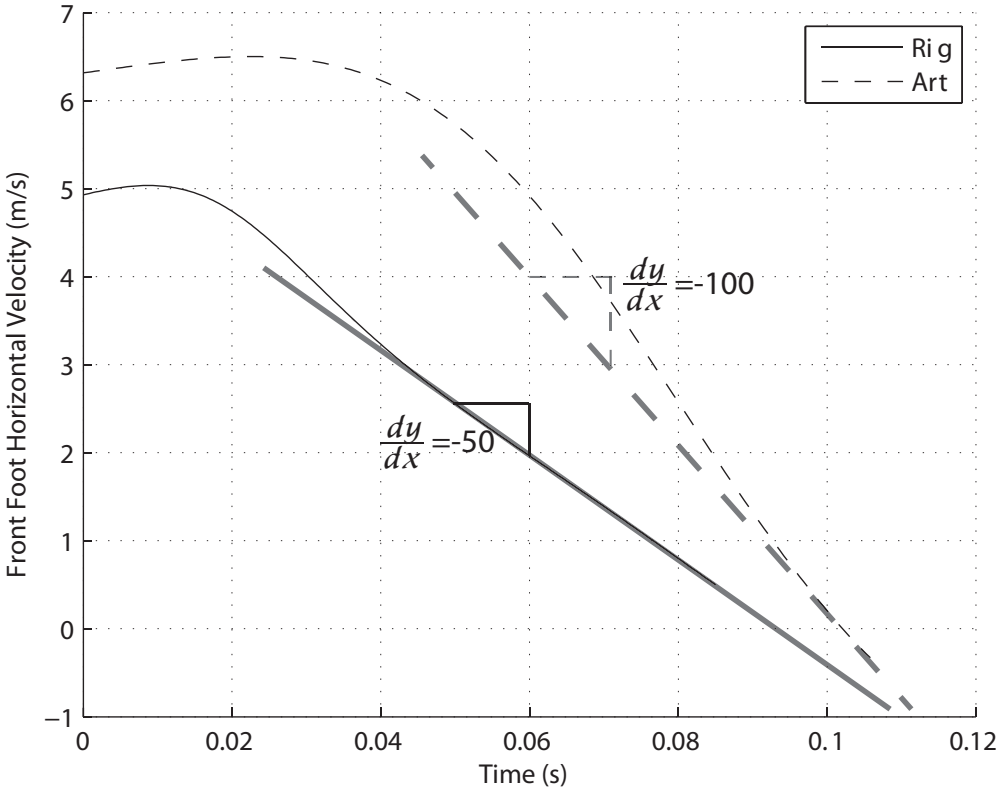

Figure 5.1 Horizontal foot velocities of the front foot over the descending portion of the extended flight phase for 9.0 m/s

Even though muscular models are not included in the simulation, the same general principle holds true for torques. Multiple torques working together are able to move the system quicker. Therefore, the back, haunch and knee can all work together in the articulated system, while the rigid can only use the haunch and knee. With the additional degree of freedom the back joint allows, the system is able to rotate the legs underneath the body more effectively, allowing for more efficient application of the impulsive forces. Fig. 5.1 shows the horizontal component of the front foot velocity during the latter portion of the extended flight phase at high speed. The articulated model's front foot velocity is able to move quicker than the rigid model's due to the increased number of joints.

Touchdown foot velocity *The spine adds to the maximum forward extension of the legs, increasing the maximum backward acceleration of the limbs before they strike the ground.* Part of this is tied in with the larger angular span that can be achieved via the articulation in the back. With the increased range of angles, the front legs have

more angle to swing through after the mid-flight transition, allowing higher backward acceleration. Both models accomplish this through the enforced horizontal foot velocity, but the rigid model develops a non-biological gaiting to incorporate the constraint. The rigid front foot has a slower magnitude of acceleration than the articulated front foot as shown in Fig. 5.1, supporting the claim.

Stance torso velocity *The spine reduces the relative forward velocity of the girdles when their respective limbs are moving the body.* This effect is most clear at the front stance phase, when the foreleg is locked to the ground, as shown in Fig. 5.2. For the articulated system, the forward velocity of the rear torso maintains its speed after the impulsive transition, but the forward velocity is transferred into a vertical component, lifting the rear portion of the body, allowing the back legs to move through and under the body in preparation for the cross over during front stance. In the rigid model, the torso is a single rigid body, so all of the forward momentum is transferred along the spine to the rear of the body. The darker arrows represent the weighted contributions of each half of the body (cranial and caudal).

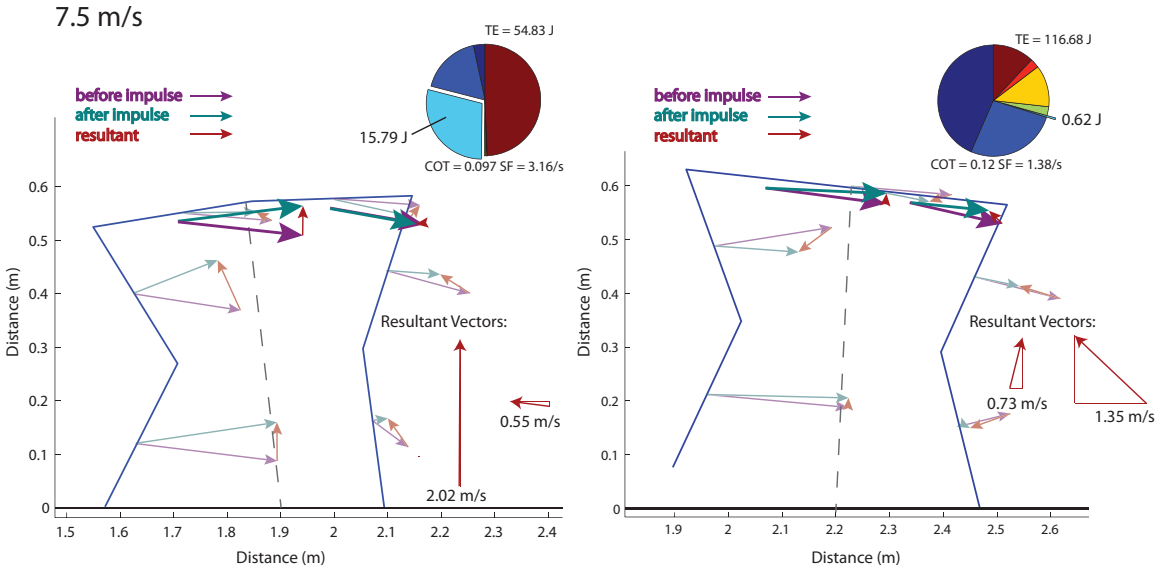

Figure 5.2 Body velocities at the *1b2* transition of best solutions for 7.5 m/s

All of these items contribute to the better CoT value for the articulated model in comparison to the rigid model at high speed.

5.1.1 Summary

Many simulations were conducted at speeds ranging from 6.0 to 9.0 m/s and stride frequencies from 0.95 to 4.5 s^{-1}. An objective function using the sum squared impulsive torques and forces, along with other weighted constraints, was used to obtain a reasonable gait. Once a converged gait was discovered, the solution was subsequently optimized with an objective function minimizing the total work required to travel a fixed distance, as determined by the step frequency and speed.

The results from this work show a decrease in the cost of transport (the work necessary to move a unit weight over a unit distance, Eqn. (3.12), as speed increases, for the articulated model and an increase in the cost of transport with increasing speed for the rigid system over the range of speeds investigated. Cost of transport (CoT) is proportional to mechanical work, defined as the sum of the absolute values of the sum of the changes in the limb kinetic energy over the impulsive transitions and stance phases. This metric is non-dimensional and represents more of a biological cost, rather than a physical cost if actuators were used. Using the absolute value includes the external work done on the system and the internal work of the legs moving relative to the center of mass. Whether a muscle is flexing or extending, energy is consumed. Including the motion of the limbs relative to the mass center, gives a more biologically realistic measure of the energy demands of the systems. Under this definition, the cost of transport for the articulated system is less than the rigid system at speeds greater than 7 m/s.

The height of the mass center of the system changes less in the articulated model than in the rigid and results in substantially lower impulsive forces than in the optimized rigid, but at the cost of higher impulsive joint torques. The maximum impulsive torque in the articulated model is in the back at the mid-flight transition, corresponding in a physical sense, to the contraction of the abdomen muscles. The rigid's large impulsive torque is in the haunch at the gathered flight to rear stance transition and is linked to the large amount of reconfiguration in a short amount of time.

5.1.2 Contributions

The hypothesis of this research was primarily interested in quantitatively evaluating the articulation in the back as a key component of efficient, high-speed running in quadrupeds. To make a fair and reasonable assessment of the flexible spine as a necessary artifact in fast gaits, two models operating under the same constraints, assumptions and parameters were constructed and evaluated. The only difference between the models was either locking the

single joint in the spine to create a rigid back or allowing it to rotate freely, as in the articulating model. The claim was verified, subject to the constraints and assumptions employed to ensure a tractable problem, through a rigorous parameter study evaluating the optimized energetics of converged solutions for a range of speeds and stride frequencies pertinent to the discussion. Although there are many quadruped models available in the literature, there were no models that evaluated *both* a rigid and articulated system at high speeds of *10 - 15 bodylengths/s.* The models provided insight into the effectiveness of biological systems, despite their simple construction.

5.2 Future Research

The analysis and results of this research present a starting point for additional avenues of investigation. With the advent of a high-speed quadruped robot on the horizon, there are further areas related to this work worthy of pursuit. The main topics addressed in this section are the virtual leg constraint, compliant mechanisms and the system stability characterization. Most of these areas of further study stem from the relaxation or removal of a constraint or assumption.

5.2.1 Virtual Leg

The virtual leg concept was employed to simplify the model. The use of point feet was also employed since leg and foot interaction are complicated mechanisms in and of themselves.

Removing the virtual leg simplification or adding an arc-like foot would allow for a better distribution of the impulsive forces, a primary concern in these systems where large impacts can damage the on-board electronics and structural components of the system. The impulsive forces and changes in kinetic energy were highest in the transitions before and after the rear stance phase in most cases. A continuous challenge with these models was the decrease in stance phase duration with increasing speed. With a four-legged quadruped model, the multi-limbed step out benefits the system by lengthening the duration the animal spends in stance, allowing for the necessary time to perform the desired reconfiguration while reducing the impulsive forces with the ground (127). Using large, arc-like feet could also accomplish this goal (1), without the additional limbs.

5.2.2 Active Torques

Another suggestion is to fine tune the models through the use of time-varying active torques (ones that change over the duration of the stance phase). These could be incorporated by including them as design variables and allowing the optimizer to search for their best values, turning on a combination of torques during stance rather than a single torque, or using time-varying torques.

The active torques could also be turned on during the flight phases to decrease the reliance on the impulsive transitions. The use of the impulsive transitions has been shown to be a reasonable methodology for intra-phase transfers, however their use limits the system in several different ways. Impulsive forces and torques are mathematical entities used to simplify the transitions, however, there are no true biological corollaries. Applying torques over a finite time period is of practical import, particularly when considering real motors and actuators.

5.2.3 Compliant Mechanisms

The definition of total work used for the energy minimization (150) uses an absolute value to count positive and negative work, since both flexion and extension of muscles contribute to the total metabolic cost of the system. However, it is observed [(8), (10), (22), (47), (64), (108)] that energy storage in elastic mechanisms contributes to efficient high-speed transport. Utilizing compliant mechanisms to store and release energy the stance phases, could further reduce the energy requirements of the systems.

A spring or other mechanism could be used in lieu of an active torque. One of the failings of the articulated model was clear in the precarious balance of the back joint. Without an active (torque) or passive (spring) mechanism in place to prevent the back from collapsing in on itself, some of the phases were rushed and purposefully short to avoid this problem. It was most noticeable in the gathered flight phase. At the lower stride frequencies, the articulating system had more issues due to the lengthening of this phase due to the absence of a mechanism to prevent the back from folding in on itself. Therefore, in order to achieve a more biologically realistic model and take advantage of acceleration / deceleration during the phases, compliant mechanisms should be included in the next model iteration.

5.2.4 Stability Characterization and Controller Development

Stability is a critical element in the design of a controller for any robotic system. Using a stable set of reference trajectories as a basis for the controller can reduce controller complexity (97), as well as reducing actuator demand and increasing energy efficiency by using the unforced system dynamics to partially drive the system (114). Gaiting and the transitions between gaits is also driven by stability measures (72). High-speed gaits are dynamically stable but are statically unstable, whereas walking gaits are the reverse. Other important functions of a quadruped's mobility, such as high-speed turning (80), are addressed through the exploitation of stability margins.

Controller development is a widely discussed and well-researched issue [(67), (87), (99), (115), (120), (123), (133)] and is a necessary component to translate this system into a physically realizable form. The ballistic trajectories developed herein can provide a basis for this controller (52). Choosing a controller that provides a balance between stability and maneuverability will be a challenging task, but one worth investigating. Not only are cheetahs able to attain high speed, but they are able to turn quickly and jump, aiding in their pursuit and evasion capabilities. These features on a robot (80) would be useful for military applications, and with the inclusion of an articulated spine, should allow better system maneuverability, otherwise lost or impaired with a rigid spine.

5.2.5 Anthropomorphic Variation

Another avenue to pursue worth investigating is the variation of the model's geometry to better represent biological system components by adjusting the masses and limb lengths. One of the energetic sinks in the models was the large amount of reconfiguration required during the rear stance phase. The kinetic energy changes of the lower forelimb contributed substantially to the high cost associated with this phase. Shortening the forelimb would decrease the kinetic energy associated with moving the leg from underneath the body, and is reflected in animal limb proportions. Implementing these simple variations would allow for allometric studies to categorize stride frequency and energetic costs related to speed [(53), (57), (54)], providing corroboration to prior work and demonstrating the scalability of the model to other species and quadruped variations other than the cheetah and greyhound.

Appendices

Appendix A

Code Diagram

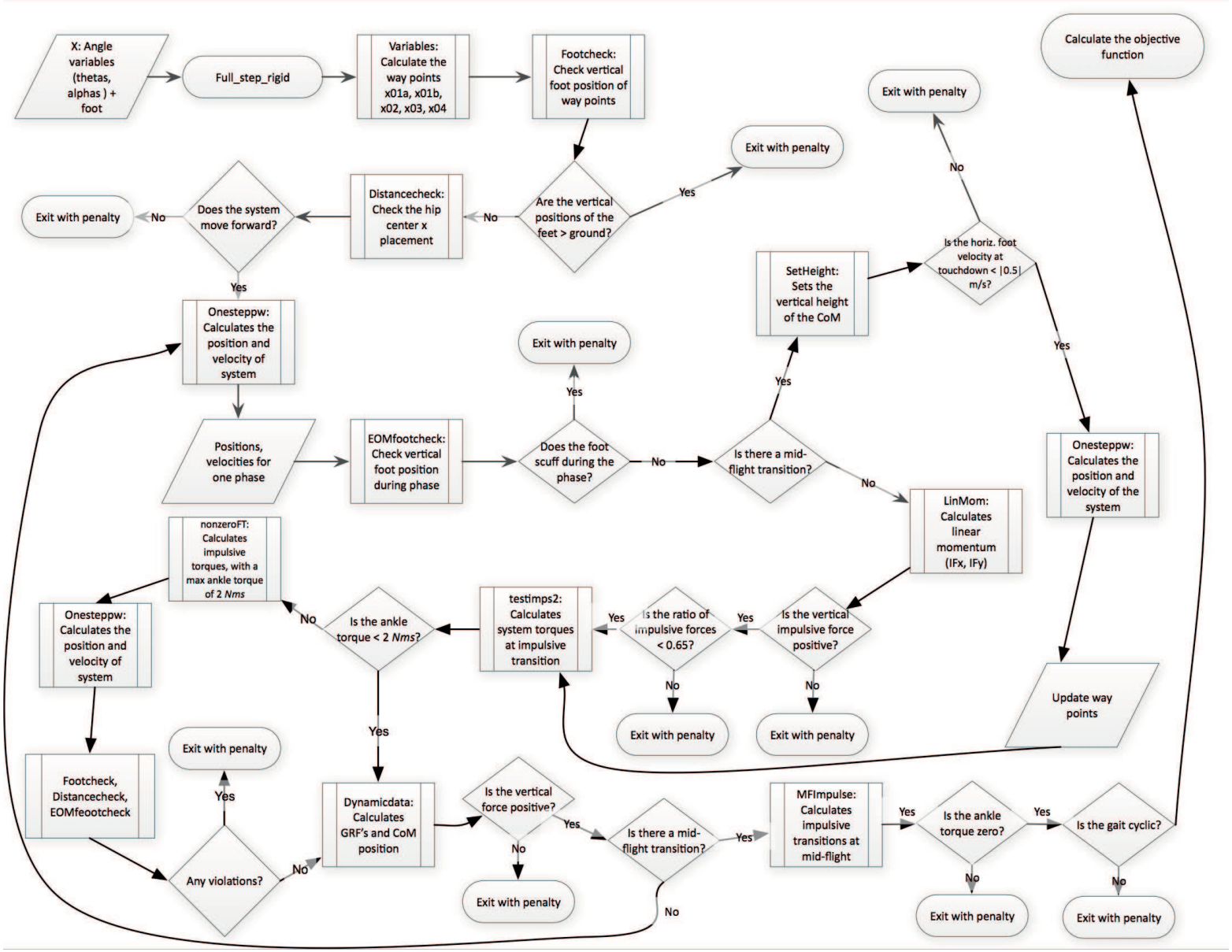

Figure A.1 Pseudo-code diagram for the simulations

Appendix B

Model Derivations

The following section presents the equations of motion for the rigid and articulated models.

Mathematica Code, Rigid Model

The text below represents the implementation of Kane's equations into *Mathematica* for the rigid model. The parameters for the model are repeated in Table (B.1 for completeness.

Model Parameter	Variable	Value
Lower / upper leg masses	m_1, m_2	2.25 kg
Torso mass	m_3	15 kg
Lower / upper leg lengths	l_1, l_2	0.3 m
Torso length	l_3	0.6 m
Lower / upper leg inertias	I_{l1}, I_{l2}	0.0173 $kg \cdot m^2$
Torso inertia	I_{l3}	0.4625 $kg \cdot m^2$
Distance to leg CoM from leg end	s_1, s_2	0.15 m
Distance to torso CoM from torso end	a	0.3 m

Table B.1 Model Parameters for the Rigid Model

Mathematica Inputs for the Rigid Model, Flight

Setup the angular velocities from (39).

OM = {0, θ'[t], 0};
O1 = {0, α1'[t] + θ'[t], 0};
O2 = {0, α2'[t] + θ'[t], 0};
O3 = {0, α3'[t] + θ'[t], 0};
O4 = {0, α4'[t] + θ'[t], 0};

Create the position vectors from (39).

rO2M = {-(a)*Cos[θ[t]], 0, (a)*Sin[θ[t]]};
rO2cO2 = {-(s2)*Sin[θ[t] + α2[t]], 0, -(s2)*Cos[θ[t] + α2[t]]};
rO1O2 = {-(l2)*Sin[θ[t] + α2[t]], 0, -(l2)*Cos[θ[t] + α2[t]]};
rO1cO1 = {-(s1)*Sin[θ[t] + α1[t]], 0, -(s1)*Cos[θ[t] + α1[t]]};
rf1O1 = {-(l1)*Sin[θ[t] + α1[t]], 0, -(l1)*Cos[θ[t] + α1[t]]};
rO3M = {(a)*Cos[θ[t]], 0, -(a)*Sin[θ[t]]};
rO3cO3 = {-(s2)*Sin[θ[t] + α3[t]], 0, -(s2)*Cos[θ[t] + α3[t]]};
rO4O3 = {-(l2)*Sin[θ[t] + α3[t]], 0, -(l2)*Cos[θ[t] + α3[t]]};
rO4cO4 = {-(s1)*Sin[θ[t] + α4[t]], 0, -(s1)*Cos[θ[t] + α4[t]]};
rf2O4 = {-(l1)*Sin[θ[t] + α4[t]], 0, -(l1)*Cos[θ[t] + α4[t]]};
rf1 = {x[t], 0, z[t]} + rO2M + rO1O2 + rf1O1;
rf2 = {x[t], 0, z[t]} + rO3M + rO4O3 + rf2O4;

Construct the velocity vectors for the system.

vM = {x'[t], 0, z'[t]} + OM×{0, 0, 0};
vO2 = vM + OM×rO2M;
v2 = vO2 + O2×rO2cO2;
vO1 = vO2 + O2×rO1O2;
v1 = vO1 + O1×rO1cO1;
vf1 = vO1 + O1×rf1O1;
vO3 = vM + OM×rO3M;
v3 = vO3 + O3×rO3cO3;
vO4 = vO3 + O3×rO4O3;
v4 = vO4 + O4×rO4cO4;
vf2 = vO4 + O4×rf2O4;

Take the derivative of the velocity vectors to obtain the accelerations of the system.

aM = D[vM, t];
a1 = D[v1, t];
a2 = D[v2, t];
a3 = D[v3, t];
a4 = D[v4, t];

Calculate the forces acting on the system.

```
FM = m3*aM;
F1 = m1*a1;
F2 = m2*a2;
F3 = m2*a3;
F4 = m1*a4;
```

Calculate the center of mass position, velocity and acceleration.

```
rCoM = ((rO2M + rO2cO2)*m2 + (rO2M + rO1O2 + rO1cO1)*m1 + ({0, 0, 0})*m3 +
(rO3M + rO3cO3)*m2 + (rO3M + rO4O3 + rO4cO4)*m1)/(2*m1 + 2*m2 + m3);
    vCoM = (vM*m3 + v1*m1 + v2*m2 + v3*m2 + v4*m1)/(2*m1 + 2*m2 + m3);
    aCoM = (aM*m3 + a1*m1 + a2*m2 + a3*m2 + a4*m1)/(2*m1 + 2*m2 + m3);
```

Mathematica Inputs for the Rigid Model, Rear Stance

Setup the angular velocities from (39).

```
OM = {0, θ'[t], 0};
O1 = {0, α1'[t] + θ'[t], 0};
O2 = {0, α2'[t] + θ'[t], 0};
O3 = {0, α3'[t] + θ'[t], 0};
O4 = {0, α4'[t] + θ'[t], 0};
```

Create the position vectors from (39).

```
rO1cf1 = {(s1)*Sin[θ[t] + α1[t]], 0, (s1)*Cos[θ[t] + α1[t]]};
rO1f1 = {(l1)*Sin[θ[t] + α1[t]], 0, (l1)*Cos[θ[t] + α1[t]]};
rO2cO1 = {(s2)*Sin[θ[t] + α2[t]], 0, (s2)*Cos[θ[t] + α2[t]]};
rO2O1 = {(l2)*Sin[θ[t] + α2[t]], 0, (l2)*Cos[θ[t] + α2[t]]};
rMO2 = {(a)*Cos[θ[t]], 0, -(a)*Sin[θ[t]]};
rO3M = {(a)*Cos[θ[t]], 0, -(a)*Sin[θ[t]]};
rO3cO3 = {-(s2)*Sin[θ[t] + α3[t]], 0, -(s2)*Cos[θ[t] + α3[t]]};
rO4O3 = {-(l2)*Sin[θ[t] + α3[t]], 0, -(l2)*Cos[θ[t] + α3[t]]};
rO4cO4 = {-(s1)*Sin[θ[t] + α4[t]], 0, -(s1)*Cos[θ[t] + α4[t]]};
rf2O4 = {-(l1)*Sin[θ[t] + α4[t]], 0, -(l1)*Cos[θ[t] + α4[t]]};
rf1 = {0, 0, 0};
```

rf2 = rO1f1 + rO2O1 + rMO2 + rO3M + rO4O3 + rf2O4;
rM = rO1f1 + rO2O1 + rMO2;

Construct the velocity vectors for the system.

vf1 = {0, 0, 0};
v1 = vf1 + O1×rO1cf1;
vO1 = vf1 + O1×rO1f1;
v2 = vO1 + O2×rO2cO1;
vO2 = vO1 + O2×rO2O1 ;
vM = vO2 + OM×rMO2;
vO3 = vM + OM×rO3M;
v3 = vO3 + O3×rO3cO3;
vO4 = vO3 + O3×rO4O3;
v4 = vO4 + O4×rO4cO4;
vf2 = vO4 + O4×rf2O4;

Take the derivative of the velocity vectors to obtain the accelerations of the system.

aM = D[vM, t];
a1 = D[v1, t];
a2 = D[v2, t];
a3 = D[v3, t];
a4 = D[v4, t];

Calculate the forces acting on the system.

FM = m3*aM;
F1 = m1*a1;
F2 = m2*a2;
F3 = m2*a3;
F4 = m1*a4;

Calculate the center of mass position, velocity and acceleration.

rCoM = (m1*rO1cf1 + m2*(rO2cO1 + rO1f1) + m3*(rO1f1 + rO2O1 + rMO2) + m2*(rO1f1 + rO2O1 + rMO2 + rO3M + rO3cO3) + m1*(rO1f1 + rO2O1 + rMO2 + rO3M + rO4O3 + rO4cO4))/(2*m1 + 2*m2 + m3);

vCoM = (vM*m3 + v1*m1 + v2*m2 + v3*m2 + v4*m1)/(2*m1 + 2*m2 + m3);
aCoM = (aM*m3 + a1*m1 + a2*m2 + a3*m2 + a4*m1)/(2*m1 + 2*m2 + m3);

Mathematica Inputs for the Rigid Model, Front Stance

Setup the angular velocities from (39).

OM = {0, θ'[t], 0};
O1 = {0, α1'[t] + θ'[t], 0};
O2 = {0, α2'[t] + θ'[t], 0};
O3 = {0, α3'[t] + θ'[t], 0};
O4 = {0, α4'[t] + θ'[t], 0};

Create the position vectors from (39).

rO4cf2 = {(s1)*Sin[θ[t] + α4[t]], 0, (s1)*Cos[θ[t] + α4[t]]};
rO4f2 = {(l1)*Sin[θ[t] + α4[t]], 0, (l1)*Cos[θ[t] + α4[t]]};
rO3cO4 = {(s2)*Sin[θ[t] + α3[t]], 0, (s2)*Cos[θ[t] + α3[t]]};
rO3O4 = {(l2)*Sin[θ[t] + α3[t]], 0, (l2)*Cos[θ[t] + α3[t]]};
rMO3 = {-(a)*Cos[θ[t]], 0, (a)*Sin[θ[t]]};
rO2M = {-(a)*Cos[θ[t]], 0, (a)*Sin[θ[t]]};
rO2cO2 = {-(s2)*Sin[θ[t] + α2[t]], 0, -(s2)*Cos[θ[t] + α2[t]]};
rO1O2 = {-(l2)*Sin[θ[t] + α2[t]], 0, -(l2)*Cos[θ[t] + α2[t]]};
rO1cO1 = {-(s1)*Sin[θ[t] + α1[t]], 0, -(s1)*Cos[θ[t] + α1[t]]};
rf1O1 = {-(l1)*Sin[θ[t] + α1[t]], 0, -(l1)*Cos[θ[t] + α1[t]]};
rf1 = rO4f2 + rO3O4 + rMO3 + rO2M + rO1O2 + rf1O1;
rf2 = {0, 0, 0};
rM = rO4f2 + rO3O4 + rMO3;

Construct the velocity vectors for the system.

vf2 = {0, 0, 0};
v4 = vf2 + O4×rO4cf2;
vO4 = vf2 + O4×rO4f2;
v3 = vO4 + O3×rO3cO4;
vO3 = vO4 + O3×rO3O4;
vM = vO3 + OM×rMO3;
vO2 = vM + OM×rO2M;

v2 = vO2 + O2×rO2cO2;
vO1 = vO2 + O2×rO1O2;
v1 = vO1 + O1×rO1cO1;
vf1 = vO1 + O1×rf1O1;

Take the derivative of the velocity vectors to obtain the accelerations of the system.

aM = D[vM, t];
a1 = D[v1, t];
a2 = D[v2, t];
a3 = D[v3, t];
a4 = D[v4, t];

Calculate the forces acting on the system.

FM = m3*aM;
F1 = m1*a1;
F2 = m2*a2;
F3 = m2*a3;
F4 = m1*a4;

Calculate the center of mass position, velocity and acceleration.

rCoM = (m1*rO4cf2 + m2*(rO3cO4 + rO4f2) + m3*(rO4f2 + rO3O4 + rMO3) + m2*(rO4f2 + rO3O4 + rMO3 + rO2M + rO2cO2) + m1*(rO4f2 + rO3O4 + rMO3 + rO2M + rO1O2 + rO1cO1))/(2*m1 + 2*m2 + m3);
vCoM = (vM*m3 + v1*m1 + v2*m2 + v3*m2 + v4*m1)/(2*m1 + 2*m2 + m3);
aCoM = (aM*m3 + a1*m1 + a2*m2 + a3*m2 + a4*m1)/(2*m1 + 2*m2 + m3);

Construct Equations of Motion for the Rigid Model

List the various vectors necessary for calculations.

Forces = Transpose[{{FM, F1, F2, F3, F4}}];
Velocities = Transpose[{{vM, v1, v2, v3, v4}}];
Omegas = Transpose[{{OM, O1, O2, O3, O4}}];
qs = Transpose[{{x[t], z[t], θ[t], α1[t], α2[t], α3[t], α4[t]}}];
Inertias = Transpose[{{Il3, Il1, Il2, Il2, Il1}}];

```
Masses = Transpose[{{m3, m1, m2, m2, m1}}];
Torques = Transpose[{{GM, G1, G2, G3, G4}}];
```

Create the qdot vector for Kane' s equations

```
For[i = 1, i <= Length[qs], i++, l[i] = Extract[D[qs, t], {i}]]
```

Construct the left hand side of the equations for Kane' s method with partial derivatives of velocities and omegas

```
For[i = 1, i <= Length[qs], i++, For[j = 1, j <= Length[Forces], j++, FFs[i, j] =
D[Velocities[[j, 1]], l[i]].Forces[[j, 1]] + D[Omegas[[j, 1]], l[i]].(Inertias[[j, 1]]*D[Omegas[[j,
1]], t])]]
    FFsT = Total[Table[FFs[i, j], {i, 7}, {j, 5}], {2}];
```

Start creating the mass matrix and right hand side equations to solve the system for the accelerations

```
For[i = 1, i <= Length[qs], i++, FFsTA[i] = CoefficientArrays[Extract[FFsT, {i}], Flat-
ten[D[qs, {t, 2}]]]];
```

Mass matrix creation

```
For[i = 1, i <= Length[qs], i++, FaMMrhs[i] = Normal[Extract[FFsTA[i], {1}]]];
    FaRHSt = Table[FaMMrhs[i], {i, 7}];
    For[i = 1, i <= Length[qs], i++, FaMM[i] = Normal[Extract[FFsTA[i], {2}]]];
    MM = Table[FaMM[i], {i, 7}] // FullSimplify;
```

Right hand side matrix creation

Construct the inertial forces for Kane' s method

```
For[i = 1, i <= Length[qs], i++, For[j = 1, j <= Length[Forces], j++, FFa[i, j] =
Masses[[j]]*g*{0, 0, 1}.D[Velocities[[j, 1]], l[i]]]];
    FFaT = Total[Table[FFa[i, j], {i, 7}, {j, 5}], {2}];
```

Construct the active force component of Kane' s equations.

```
For[i = 1, i <= Length[qs], i++, Dvfs[i] = {1, 0, 0}.D[vf1, l[i]]*FF1x[t] + {0, 0, 1}.D[vf1,
l[i]]*FF1z[t] + {1, 0, 0}.D[vf2, l[i]]*FF2x[t] + {0, 0, 1}.D[vf1, l[i]]*FF2z[t]];
```

DvfsT = Total[Table[Dvfs[i], {i, 7}], {2}];

Construct the active torques component of Kane' s equations.

$$\text{DgsT} = \begin{pmatrix} 0 & 0 & 0 & 0 \\ 0 & 0 & 0 & 0 \\ 0 & -1 & -1 & 0 \\ 1 & 0 & 0 & 0 \\ -1 & 1 & 0 & 0 \\ 0 & 0 & 1 & -1 \\ 0 & 0 & 0 & 1 \end{pmatrix} .\text{Transpose}\left[\begin{pmatrix} \text{G1} & \text{G2} & \text{G3} & \text{G4} \end{pmatrix}\right];$$

RHS = FFaT + FaRHSt;

Set up the constraints for the equations.

T1x = x[t] - a*Cos[θ[t]] - l1*Sin[θ[t] + α1[t]] - l2*Sin[θ[t] + α2[t]];
T1z = z[t] + a*Sin[θ[t]] - l1*Cos[θ[t] + α1[t]] - l2*Cos[θ[t] + α2[t]];
T2x = x[t] + a*Cos[θ[t]] - l1*Sin[θ[t] + α4[t]] - l2*Sin[θ[t] + α3[t]];
T2z = z[t] - a*Sin[θ[t]] - l1*Cos[θ[t] + α4[t]] - l2*Cos[θ[t] + α3[t]];

V1x = D[T1x, t]; V1z = D[T1z, t]; V2x = D[T2x, t]; V2z = D[T2z, t];

A1x = D[T1x, {t, 2}]; A1z = D[T1z, {t, 2}]; A2x = D[T2x, {t, 2}]; A2z = D[T2z, {t, 2}];

D1a = Extract[CoefficientArrays[D[T1x, t], Flatten[D[qs, t]]], {2}];
D1b = Extract[CoefficientArrays[D[T1z, t], Flatten[D[qs, t]]], {2}];
D2a = Extract[CoefficientArrays[D[T2x, t], Flatten[D[qs, t]]], {2}];
D2b = Extract[CoefficientArrays[D[T2z, t], Flatten[D[qs, t]]], {2}];

D1 = Transpose[{Normal[D1a], Normal[D1b]}];
D2 = Transpose[{Normal[D2a], Normal[D2b]}];

E1 = Join[{Extract[CoefficientArrays[A1x, Flatten[D[qs, {t, 2}]]], {1}]},
{Extract[CoefficientArrays[A1z, Flatten[D[qs, {t, 2}]]], {1}]}];
E2 = Join[{Extract[CoefficientArrays[A2x, Flatten[D[qs, {t, 2}]]], {1}]}, {
Extract[CoefficientArrays[A2z, Flatten[D[qs, {t, 2}]]], {1}]}];

Mathematica Code, Articulated Model

The text below represents the implementation of Kane's equations into *Mathematica* for the articulated model. The parameters for the model are repeated in Table (B.2 for completeness.

Model Parameter	Variable	Value
Lower / upper leg masses	m_1, m_2	2.25 kg
Torso masses	m_3	7.5 kg
Lower / upper leg lengths	l_1, l_2	0.3 m
Torso lengths	l_3	0.3 m
Lower / upper leg inertias	I_{l1}, I_{l2}	0.0173 $kg \cdot m^2$
Torso inertias	I_{l3}	0.0578 $kg \cdot m^2$
Lower / upper leg distance to CoM	s_1, s_2	0.15 m
Torso distance to CoM	$a/2$	0.15 m

Table B.2 Model Parameters for the Articulated Model

Mathematica Inputs for the Articulated Model, Flight

Setup the angular velocities.

OM1 = {0, 0, θ1'[t]};
OM2 = {0, 0, θ2'[t]};
O1 = {0, 0, θ1'[t] + α1'[t]};
O2 = {0, 0, θ1'[t] + α2'[t]};
O3 = {0, 0, θ2'[t] + α3'[t]};
O4 = {0, 0, θ2'[t] + α4'[t]};

Create the position vectors.

rMm1 = {-a/2*Cos[θ1[t]], -a/2*Sin[θ1[t]], 0};
rO2M = {-a*Cos[θ1[t]], -a*Sin[θ1[t]], 0};
rO2cO2 = {s2*Sin[θ1[t] + α2[t]], -(s2)*Cos[θ1[t] + α2[t]], 0};
rO1O2 = {l2*Sin[θ1[t] + α2[t]], -(l2)*Cos[θ1[t] + α2[t]], 0};
rO1cO1 = {s1*Sin[θ1[t] + α1[t]], -(s1)*Cos[θ1[t] + α1[t]], 0};
rf1O1 = {l1*Sin[θ1[t] + α1[t]], -(l1)*Cos[θ1[t] + α1[t]], 0};
rMm2 = {a/2*Cos[θ2[t]], a/2*Sin[θ2[t]], 0};
rO3M = {a*Cos[θ2[t]], a*Sin[θ2[t]], 0};
rO3cO3 = {(s2)*Sin[θ2[t] + α3[t]], -(s2)*Cos[θ2[t] + α3[t]], 0};
rO4O3 = {(l2)*Sin[θ2[t] + α3[t]], -(l2)*Cos[θ2[t] + α3[t]], 0};
rO4cO4 = {(s1)*Sin[θ2[t] + α4[t]], -(s1)*Cos[θ2[t] + α4[t]], 0};
rf2O4 = {(l1)*Sin[θ2[t] + α4[t]], -(l1)*Cos[θ2[t] + α4[t]], 0};
rf1 = {x[t], y[t], 0} + rO2M + rO1O2 + rf1O1;
rf2 = {x[t], y[t], 0} + rO3M + rO4O3 + rf2O4;

Construct the velocity vectors for the system.

vM = {0, 0, 0};
vm1 = vM + OM1×rMm1;
vO2 = vM + OM1×rO2M;
v2 = vO2 + O2×rO2cO2;
vO1 = vO2 + O2×rO1O2;
v1 = vO1 + O1×rO1cO1;
vf1 = vO1 + O1×rf1O1;
vm2 = vM + OM2×rMm2;
vO3 = vM + OM2×rO3M;
v3 = vO3 + O3×rO3cO3;
vO4 = vO3 + O3×rO4O3;
v4 = vO4 + O4×rO4cO4;
vf2 = vO4 + O4×rf2O4;

Take the derivative of the velocity vectors to obtain the accelerations of the system.

am1 = D[vm1, t];
am2 = D[vm2, t];
a1 = D[v1, t];
a2 = D[v2, t];
a3 = D[v3, t];
a4 = D[v4, t];

Calculate the forces acting on the system.

Fm1 = m3/2*am1;
Fm2 = m3/2*am2;
F1 = m1*a1;
F2 = m2*a2;
F3 = m2*a3;
F4 = m1*a4;

Calculate the center of mass position, velocity and acceleration.

rCoM = (rMm1*m3/2 + rMm2*m3/2 + (rO2M + rO2cO2)*m2 + (rO2M + rO1O2 + rO1cO1)*m1 + (rO3M + rO3cO3)*m2 + (rO3M + rO4O3 + rO4cO4)*m1)/(2*m1 + 2*m2

+ m3);

vCoM = (vm1*m3/2 + vm2*m3/2 + v1*m1 + v2*m2 + v3*m2 + v4*m1)/(2*m1 + 2*m2 + m3);

aCoM = (am1*m3/2 + am2*m3/2 + a1*m1 + a2*m2 + a3*m2 + a4*m1)/(2*m1 + 2*m2 + m3);

Mathematica Construction of Equations of Motion (Articulated, Rear Stance)

Setup the angular velocities.

OM1 = {0, 0, θ1'[t]};
OM2 = {0, 0, θ2'[t]};
O1 = {0, 0, θ1'[t] + α1'[t]};
O2 = {0, 0, θ1'[t] + α2'[t]};
O3 = {0, 0, θ2'[t] + α3'[t]};
O4 = {0, 0, θ2'[t] + α4'[t]};

Create the position vectors.

r01cf1 = {-s1*Sin[θ1[t] + α1[t]], (s1)*Cos[θ1[t] + α1[t]], 0};
rO1f1 = {-l1*Sin[θ1[t] + α1[t]], (l1)*Cos[θ1[t] + α1[t]], 0};
rO2cO1 = {-s2*Sin[θ1[t] + α2[t]], (s2)*Cos[θ1[t] + α2[t]], 0};
rO2O1 = {-l2*Sin[θ1[t] + α2[t]], (l2)*Cos[θ1[t] + α2[t]], 0};
rm102 = {a/2*Cos[θ1[t]], a/2*Sin[θ1[t]], 0};
rM02 = {a*Cos[θ1[t]], a*Sin[θ1[t]], 0};
rMm2 = {a/2*Cos[θ2[t]], a/2*Sin[θ2[t]], 0};
rO3M = {a*Cos[θ2[t]], a*Sin[θ2[t]], 0};
rO3cO3 = {(s2)*Sin[θ2[t] + α3[t]], -(s2)*Cos[θ2[t] + α3[t]], 0};
rO4O3 = {(l2)*Sin[θ2[t] + α3[t]], -(l2)*Cos[θ2[t] + α3[t]], 0};
rO4cO4 = {(s1)*Sin[θ2[t] + α4[t]], -(s1)*Cos[θ2[t] + α4[t]], 0};
rf2O4 = {(l1)*Sin[θ2[t] + α4[t]], -(l1)*Cos[θ2[t] + α4[t]], 0};
rf1 = {0, 0, 0};
rf2 = rO1f1 + rO2O1 + rM02 + rO3M + rO4O3 + rf2O4;
rM = rO1f1 + rO2O1 + rM02;

Construct the velocity vectors for the system.

vf1 = {0, 0, 0};
v1 = vf1 + O1×r01cf1;
vO1 = vf1 + O1×rO1f1;
v2 = vO1 + O2×rO2cO1;
vO2 = vO1 + O2×rO2O1;
vm1 = vO2 + OM1×rm102;
vM = vO2 + OM1×rM02;
vm2 = vM + OM2×rMm2;
vO3 = vM + OM2×rO3M;
v3 = vO3 + O3×rO3cO3;
vO4 = vO3 + O3×rO4O3;
v4 = vO4 + O4×rO4cO4;
vf2 = vO4 + O4×rf2O4;

Take the derivative of the velocity vectors to obtain the accelerations of the system.

am1 = D[vm1, t];
am2 = D[vm2, t];
a1 = D[v1, t];
a2 = D[v2, t];
a3 = D[v3, t];
a4 = D[v4, t];

Calculate the forces acting on the system.

Fm1 = m3/2*am1;
Fm2 = m3/2*am2;
F1 = m1*a1;
F2 = m2*a2;
F3 = m2*a3;
F4 = m1*a4;

Calculate the center of mass position, velocity and acceleration.

rCoM = ((rO1f1 + rO2O1 + rm102)*m3/2 + (rO1f1 + rO2O1 + rM02 + rMm2)*m3/2 + (rO1f1 + rO2cO1)*m2 + (r01cf1)*m1 + (rO1f1 + rO2O1 + rM02 + rO3M + rO3cO3)*m2

+ (rO1f1 + rO2O1 + rM02 + rO3M + rO4O3 + rO4cO4)*m1)/(2*m1 + 2*m2 + m3);

vCoM = (vm1*m3/2 + vm2*m3/2 + v1*m1 + v2*m2 + v3*m2 + v4*m1)/(2*m1 + 2*m2 + m3);

aCoM = (am1*m3/2 + am2*m3/2 + a1*m1 + a2*m2 + a3*m2 + a4*m1)/(2*m1 + 2*m2 + m3);

Mathematica Construction of Equations of Motion (Articulated, Front Stance)

Setup the angular velocities.

OM1 = {0, 0, θ1'[t]};
OM2 = {0, 0, θ2'[t]};
O1 = {0, 0, θ1'[t] + α1'[t]};
O2 = {0, 0, θ1'[t] + α2'[t]};
O3 = {0, 0, θ2'[t] + α3'[t]};
O4 = {0, 0, θ2'[t] + α4'[t]};

Create the position vectors.

rMm1 = {-a/2*Cos[θ1[t]], -a/2*Sin[θ1[t]], 0};
rO2M = {-a*Cos[θ1[t]], -a*Sin[θ1[t]], 0};
rO2cO2 = {s2*Sin[θ1[t] + α2[t]], -(s2)*Cos[θ1[t] + α2[t]], 0};
rO1O2 = {l2*Sin[θ1[t] + α2[t]], -(l2)*Cos[θ1[t] + α2[t]], 0};
rO1cO1 = {s1*Sin[θ1[t] + α1[t]], -(s1)*Cos[θ1[t] + α1[t]], 0};
rf1O1 = {l1*Sin[θ1[t] + α1[t]], -(l1)*Cos[θ1[t] + α1[t]], 0};
rO4cf2 = {-(s1)*Sin[θ2[t] + α4[t]], (s1)*Cos[θ2[t] + α4[t]], 0};
rO4f2 = {-(l1)*Sin[θ2[t] + α4[t]], (l1)*Cos[θ2[t] + α4[t]], 0};
rO3cO4 = {-(s2)*Sin[θ2[t] + α3[t]], (s2)*Cos[θ2[t] + α3[t]], 0};
rO3O4 = {-(l2)*Sin[θ2[t] + α3[t]], (l2)*Cos[θ2[t] + α3[t]], 0};
rm2O3 = {-a/2*Cos[θ2[t]], -a/2*Sin[θ2[t]], 0};
rMO3 = {-a*Cos[θ2[t]], -a*Sin[θ2[t]], 0};
rf2 = {0, 0, 0};
rf1 = rf1O1 + rO1O2 + rO2M + rMO3 + rO3O4 + rO4f2;
rM = rO4f2 + rO3O4 + rMO3;

Construct the velocity vectors for the system.

vf2 = {0, 0, 0};
v4 = vf2 + O4×rO4cf2;
vO4 = vf2 + O4×rO4f2;
v3 = vO4 + O3×rO3cO4;
vO3 = vO4 + O3×rO3O4;
vm2 = vO3 + OM2×rm2O3;
vM = vO3 + OM2×rMO3;
vm1 = vM + OM1×rMm1;
vO2 = vM + OM1×rO2M;
v2 = vO2 + O2×rO2cO2;
vO1 = vO2 + O2×rO1O2;
v1 = vO1 + O1×rO1cO1;
vf1 = vO1 + O1×rf1O1;

Take the derivative of the velocity vectors to obtain the accelerations of the system.

am1 = D[vm1, t];
am2 = D[vm2, t];
a1 = D[v1, t];
a2 = D[v2, t];
a3 = D[v3, t];
a4 = D[v4, t];

Calculate the forces acting on the system.

Fm1 = m3/2*am1;
Fm2 = m3/2*am2;
F1 = m1*a1;
F2 = m2*a2;
F3 = m2*a3;
F4 = m1*a4;

Calculate the center of mass position, velocity and acceleration.

rCoM = ((rMm1 + rMO3 + rO3O4 + rO4f2)*m3/2 + (rm2O3 + rO3O4 + rO4f2)*m3/2 + (rO2M + rO2cO2 + rMO3 + rO3O4 + rO4f2)*m2 + (rO2M + rO1O2 + rO1cO1 + rMO3 +

rO3O4 + rO4f2)*m1 + (rO3cO4 + rO4f2)*m2 + (rO4cf2)*m1)/(2*m1 + 2*m2 + m3);

vCoM = (vm1*m3/2 + vm2*m3/2 + v1*m1 + v2*m2 + v3*m2 + v4*m1)/(2*m1 + 2*m2 + m3);

aCoM = (am1*m3/2 + am2*m3/2 + a1*m1 + a2*m2 + a3*m2 + a4*m1)/(2*m1 + 2*m2 + m3);

Construct Equations of Motion for the Articulated Model

List the various vectors necessary for calculations.

```
Forces = Transpose[{{Fm1, Fm2, F1, F2, F3, F4}}];
Velocities = Transpose[{{vm1, vm2, v1, v2, v3, v4}}];
Omegas = Transpose[{{OM1, OM2, O1, O2, O3, O4}}];
qs = Transpose[{{x[t], y[t], θ1[t], θ2[t], α1[t], α2[t], α3[t], α4[t]}}];
Inertias = Transpose[{{Il3/8, Il3/8, Il1, Il2, Il2, Il1}}];
Masses = Transpose[{{m3/2, m3/2, m1, m2, m2, m1}}];
Torques = Transpose[{{GM1, GM2, G1, G2, G3, G4}}];
```

Create the qdot vector for Kane' s equations

```
For[i = 1, i <= Length[qs], i++, l[i] = Extract[D[qs, t], {i}]]
```

Construct the left hand side of the equations for Kane' s method with partial derivatives of velocities and omegas

```
For[i = 1, i <= Length[qs], i++, For[j = 1, j <= Length[Forces], j++, FFs[i, j] =
D[Velocities[[j, 1]], l[i]].Forces[[j, 1]] + D[Omegas[[j, 1]], l[i]].(Inertias[[j, 1]]*D[Omegas[[j,
1]], t])]]
    FFsT = Total[Table[FFs[i, j], {i, Length[qs]}, {j, Length[Forces]}], {2}];
```

Start creating the mass matrix and right hand side equations to solve the system for the accelerations

```
For[i = 1, i <= Length[qs], i++, FFsTA[i] = CoefficientArrays[Extract[FFsT, {i}], Flat-
ten[D[qs, {t, 2}]]]];
```

Mass matrix creation

```
For[i = 1, i <= Length[qs], i++, FaMMrhs[i] = Normal[Extract[FFsTA[i], {1}]]];
```

```
FaRHSt = Table[FaMMrhs[i], {i, Length[qs]}];
For[i = 1, i <= Length[qs], i++, FaMM[i] = Normal[Extract[FFsTA[i], {2}]]];
MM = Table[FaMM[i], {i, Length[qs]}] // FullSimplify;
```

Construct the inertial forces for Kane' s method

```
For[i = 1, i <= Length[qs], i++, For[j = 1, j <= Length[Forces], j++, FFa[i, j] =
Masses[[j]]*g*{0, 1, 0}.D[Velocities[[j, 1]], l[i]]]];
FFaT = Total[Table[FFa[i, j], {i, Length[qs]}, {j, Length[Forces]}], {2}];
```

Construct the active force component of Kane' s equations.

```
For[i = 1, i <= Length[qs], i++, Dvfs[i] = {1, 0, 0}.D[vf1, l[i]]*FF1x[t] + {0, 0, 1}.D[vf1,
l[i]]*FF1y[t] + {1, 0, 0}.D[vf2, l[i]]*FF2x[t] + {0, 0, 1}.D[vf1, l[i]]*FF2y[t]];
DvfsT = Total[Table[Dvfs[i], {i, Length[qs]}], {2}];
```

Construct the active torques component of Kane' s equations.

$$\text{DgsT} = \begin{pmatrix} 0 & 0 & 0 & 0 & 0 \\ 0 & 0 & 0 & 0 & 0 \\ 1 & 0 & -1 & 0 & 0 \\ -1 & 0 & 0 & -1 & 0 \\ 0 & 1 & 0 & 0 & 0 \\ 0 & -1 & 1 & 0 & 0 \\ 0 & 0 & 0 & 1 & -1 \\ 0 & 0 & 0 & 0 & 1 \end{pmatrix} .\text{Transpose}\left[\begin{pmatrix} \text{GM} & \text{G1} & \text{G2} & \text{G3} & \text{G4} \end{pmatrix}\right];$$

```
RHS = FFaT + FaRHSt;
```

Set up the constraints for the equations.

```
T1x = x[t] - a*Cos[θ1[t]] + l2*Sin[θ1[t] + α2[t]] + l1*Sin[θ1[t] + α1[t]];
T1y = y[t] - a*Sin[θ1[t]] - l2*Cos[θ1[t] + α2[t]] - l1*Cos[θ1[t] + α1[t]];
T2x = x[t] + a*Cos[θ2[t]] + l2*Sin[θ2[t] + α3[t]] + l1*Sin[θ2[t] + α4[t]];
T2y = y[t] + a*Sin[θ2[t]] - l2*Cos[θ2[t] + α3[t]] - l1*Cos[θ2[t] + α4[t]];
V1x = D[T1x, t]; V1y = D[T1y, t]; V2x = D[T2x, t]; V2y = D[T2y, t];
A1x = D[T1x, {t, 2}]; A1y = D[T1y, {t, 2}]; A2x = D[T2x, {t, 2}]; A2y = D[T2y, {t, 2}];
D1a = Extract[CoefficientArrays[D[T1x, t], Flatten[D[qs, t]]], {2}];
D1b = Extract[CoefficientArrays[D[T1y, t], Flatten[D[qs, t]]], {2}];
```

```
D2a = Extract[CoefficientArrays[D[T2x, t], Flatten[D[qs, t]]], {2}];
D2b = Extract[CoefficientArrays[D[T2y, t], Flatten[D[qs, t]]], {2}];
    D1 = Transpose[{Normal[D1a], Normal[D1b]}];
D2 = Transpose[{Normal[D2a], Normal[D2b]}];
    E1 = Join[{Extract[CoefficientArrays[A1x, Flatten[D[qs, {t, 2}]]], {1}]},
{Extract[CoefficientArrays[A1y, Flatten[D[qs, {t, 2}]]], {1}]}];
E2 = Join[{Extract[CoefficientArrays[A2x, Flatten[D[qs, {t, 2}]]], {1}]},
{Extract[CoefficientArrays[A2y, Flatten[D[qs, {t, 2}]]], {1}]}];
```

Appendix C

ADAMS Model Parameters

INSTRUCTIONS FOR VERIFYING MATLAB MODELS IN ADAMS

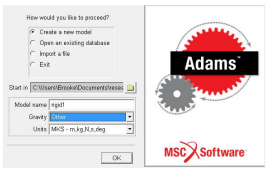

1. Create a new model. Set gravity to other and units to MKS.

2. Set gravity to -z direction.

3. Reorient the screen.

4. Set the orientation of the working grid to Global XZ. Change Angle units to radians.

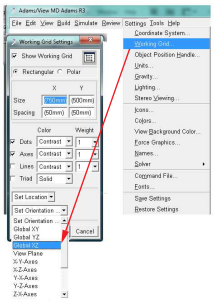

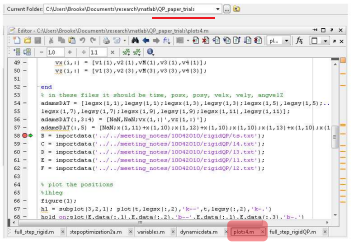

5. Switch to MATLAB. Load the delta from deltas.m. Run full_step_rigid(delta,1,2). Then run plots4(t,x) to get the ADAMS data.

6. Create 6 points and copy the ADAMS information.

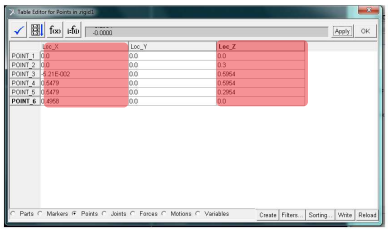

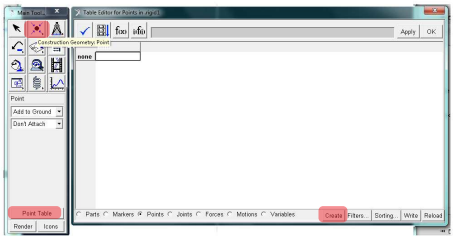

7. Create the limbs, setting the width and depth at 0.05m.

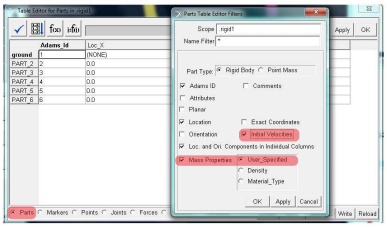

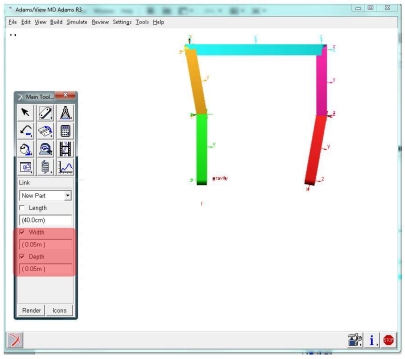

8. Using the Table Editor > Parts, add mass properties and initial velocities to filter items. Add the MATLAB data to the appropriate bodies. VX, VZ and WZ.

RIGID

9. Add the revolute joints and run the simulation for the desired time and 200 steps.

Figure C.1 Procedural outline for ADAMS model verification

Appendix D

Rigid Kinetic Energy Detail Plots

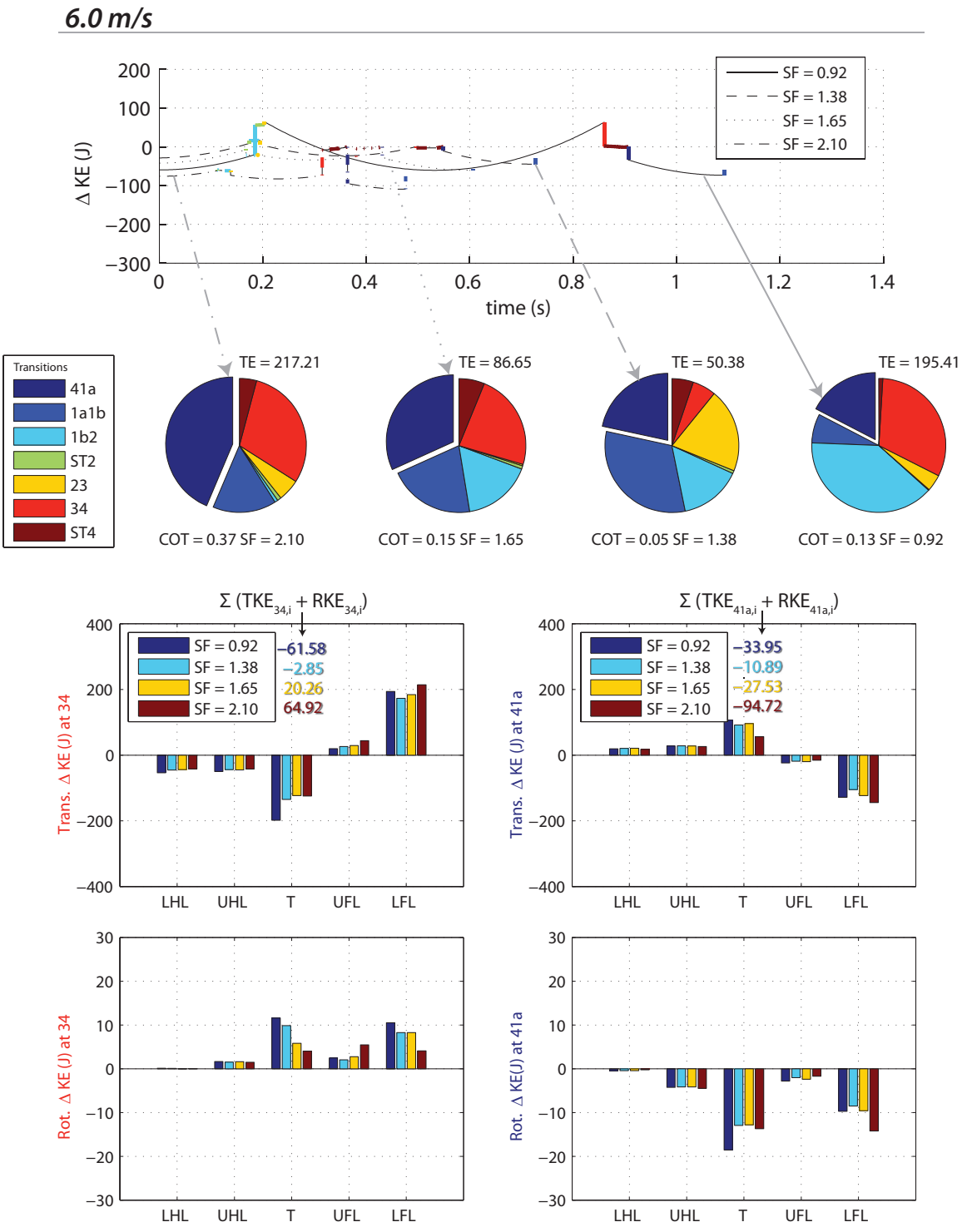

Figure D.1 Kinetic energy changes in detail for Rigid model at 6.0 m/s

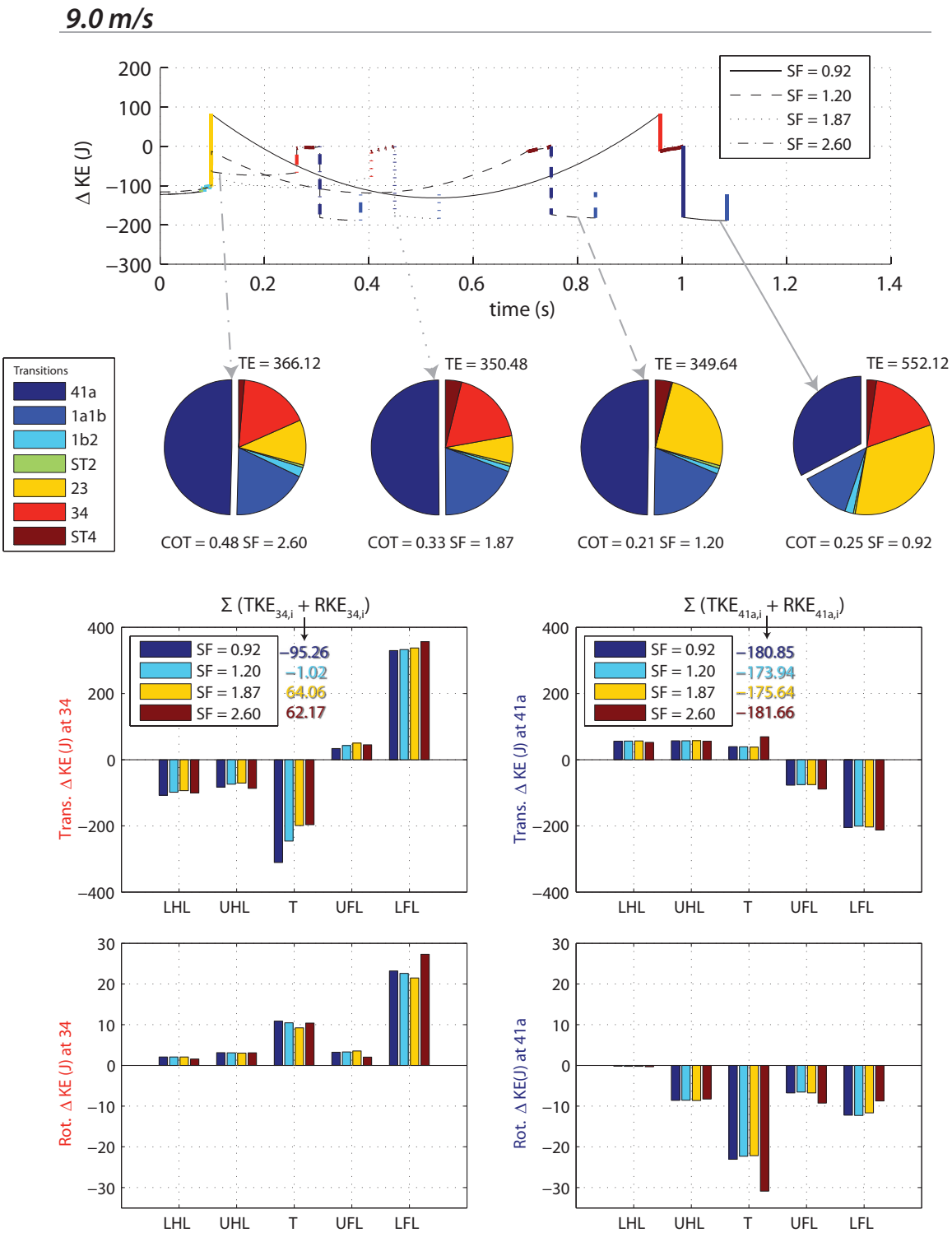

Figure D.2 Kinetic energy changes in detail for Rigid model at 9.0 m/s

Bibliography

[1] P. G. Adamczyk, S. H. Collins, and A. D. Kuo. The advantages of a rolling foot in human walking. *Journal of experimental biology*, 209(20):3953, 2006.

[2] SK Agrawal and KJ Waldron. Impulsive model for a quadruped running machine. In *Proc. of the Winter Annual Meeting of ASME*, volume 11, pages 139–148, 1989.

[3] M. Alamir, M. El Rafei, G. Hafidi, N. Marchand, M. Porez, and F. Boyer. Feedback design for 3d movement of an eel-like robot. In *2007 IEEE International Conference on Robotics and Automation*, page 6, Roma, Italy, 10-14 April 2007 2007. Dept. of Autom. control, GIPSA-Lab, France, IEEE.

[4] Jan Albiez and Karstan Berns. Biological inspired walking how much nature do we need?, 2005.

[5] Jan Albiez, Tobias Luksch, Karsten Berns, and Rudiger Dillmann. An activation-based behavior control architecture for walking machines. *The International Journal of Robotics Research*, 22(3-4):203–211, March 1 2003.

[6] R. M. Alexander. Estimates of energy cost for quadrupedal running gaits. *Journal of zoology*, 190:155, 1980.

[7] R. M. Alexander. The gaits of bipedal and quadrupedal animals. *The International Journal of Robotics Research*, 3(2):49–59, June 1 1984.

[8] R. M. Alexander. Elastic structures in the back and their role in galloping in some mammals. *Journal of zoology*, 207:467–482, 1985.

[9] R. M. Alexander. Optimization and gaits in the locomotion of vertebrates. *Physiological Reviews*, 69(4):1199–1227, October 1 1989.

[10] R. M. Alexander. Three uses for springs in legged locomotion. *The International Journal of Robotics Research*, 9(2):53–61, April 1 1990.

[11] R. M. Alexander. Mechanics of animal movement. *Current Biology*, 15(16):R616–R619, August 2005.

[12] R. M. Alexander. Models and the scaling of energy costs for locomotion. *Journal of Experimental Biology*, 208(9):1645–1652, May 1 2005.

[13] R.M. Alexander. Why mammals gallop. *American Zoologist*, 28(1):237–245, 1988.

[14] T. J. Allen, R. D. Quinn, R. J. Bachmann, and R. E. Ritzmann. Abstracted biological principles applied with reduced actuation improve mobility of legged vehicles. In *Proceedings of the International Conference on Intelligent Robots and Systems, 2003.*, volume 2, pages 1370–1375 vol.2, 2003.

[15] Yannick Aoustin, Christine Chevallereau, and Alexander Formal'sky. Numerical and experimental study of the virtual quadrupedal walking robot-semiquad. *Multibody System Dynamics*, 16(1):1–20, 08/01/ 2006.

[16] K.S. Aschenbeck, N.I. Kern, R.J. Bachmann, and R.D. Quinn. Design of a quadruped robot driven by air muscles. In *IEEE/RAS-EMBS International Conference on Biomedical Robotics and Biomechatronics, 2006.*, pages 875–880. IEEE, 2006.

[17] D.M. Badoux. Friction between feet and ground. *Nature*, 202:266–267, 1964.

[18] M.D. Berkemeier. Modeling the dynamics of quadrupedal running. *The International Journal of Robotics Research*, 17(9):971, 1998.

[19] K. Berns, W. Ilg, M. Deck, and R. Dillmann. The mammalian-like quadrupedal walking machine bisam. In *Proceedings*, AMC'98 - Coimbra. 1998 5th International Workshop on Advanced Motion Control, pages 429–33, Coimbra, Portugal, 29 June-1 July 1998 1998. IEEE.

[20] J. E. A. Bertram, D. V. Lee, H. N. Case, and R. J. Todhunter. Comparison of the trotting gaits of labrador retrievers and greyhounds. *American Journal of Veterinary Research*, 61(7):832–838, 2000.

[21] W. Blajer and W. Schiehlen. Walking without impacts as a motion/force control problem. *Journal of dynamic systems, measurement, and control*, 114:660, 1992.

[22] R. Blickhan. The spring-mass model for running and hopping. *Journal of Biomechanics*, 22(11-12):1217–1227, 1989.

[23] Bronek M. Boszczyk, Alexandra A. Boszczyk, and Reinhard Putz. Comparative and functional anatomy of the mammalian lumbar spine. *The Anatomical Record*, 264(2):157–168, 2001.

[24] R. Breithaupt, J. Dahnke, K. Zahedi, J. Hertzberg, and F. Pasemann. Robosalamander – an approach for the benefit of both robotics and biology. In *Proceedings of the Fifth International Conference on Climbing and Walking Robots*, page 55, September 2002.

[25] A. Bruce, I. Nourbakhsh, and R. Simmons. The role of expressiveness and attention in human-robot interaction. In *Proceedings of IEEE International Conference on Robotics and Automation, 2002.*, volume 4, pages 4138–4142. IEEE, 2002.

[26] Edna Brustein and Serge Rossignol. Recovery of locomotion after ventral and ventrolateral spinal lesions in the cat: Deficits and adaptive mechanisms. *Journal of Neurophysiology*, 80(3):1245–1267, September 1 1998.

[27] J. D. Bryant, M. B. Bennett, J. Brust, and R. Alexander. Forces exerted on the ground by galloping dogs (canis familiaris). *Journal of zoology*, 213(2):193–203, 1987.

[28] Čapek, P. Selver, and S. N. Playfair. *RUR (Rossum's universal robots): a fantastic melodrama in three acts and an epilogue*. S. French, 1923.

[29] G. A. Cavagna, N. C. Heglund, and C. R. Taylor. Mechanical work in terrestrial locomotion: two basic mechanisms for minimizing energy expenditure. *The American Journal of Physiology*, 233(5):R243–61, 1977.

[30] Jorge E. Collazos-Castro. Locomotor deficits and adaptive mechanisms after thoracic spinal cord contusion in the adult rat. *Journal of neurotrauma*, 23(1):1, 2006.

[31] A. Crespi. From swimming to walking with a salamander robot driven by a spinal cord model. *Science*, 315(5817):1416, 2007.

[32] Monica A. Daley and Andrew A. Biewener. Running over rough terrain reveals limb control for intrinsic stability. *Proceedings of the National Academy of Sciences*, 103(42):15681–15686, October 17 2006.

[33] A. Davids. Urban search and rescue robots: From tragedy to technology. *IEEE Intelligent Systems*, 17(2):81–83, 2002.

[34] P. Deegan, R. Grupen, A. Hanson, E. Horrell, S. Ou, E. Riseman, S. Sen, B. Thibodeau, A. Williams, and D. Xie. Mobile manipulators for assisted living in residential settings. *Autonomous Robots*, 24(2), 2008.

[35] Inneke H. Drespe, Gert K. Polzhofer, A. Simon Turner, and Jonathan N. Grauer. Animal models for spinal fusion. *The Spine Journal*, 5:S209–S216, 2005.

[36] Arthur W. English. The functions of the lumbar spine during stepping in the cat. *Journal of Morphology*, 165(1):55–66, 1980.

[37] Meg Evans. The prodigious jump of the click beetle. *New Scientist*, 21:490–494, 1972.

[38] C. T. Farley, J. Glasheen, and T. A. McMahon. Running springs: speed and animal size. *Journal of Experimental Biology*, 185(1):71–86, December 1 1993.

[39] A. Formal'sky, C. Chevallereau, and B. Perrin. On ballistic walking locomotion of a quadruped. *The International Journal of Robotics Research*, 19(8):743–761, August 1 2000.

[40] M. Fujita. On activating human communications with pet-type robot AIBO. *Proceedings of the IEEE*, 92(11):1804–1813, 2004.

[41] M. Fujita. On activating human communications with pet-type robot aibo. *Proceedings of the IEEE*, 92(11):1804–1813, 2004.

[42] R. J. Full, R. Blickhan, and L. H. Ting. Leg design in hexapedal runners. *Journal of Experimental Biology*, 158(1):369–390, July 1 1991.

[43] J. Furusho, A. Sano, M. Sakaguchi, and E. Koizumi. Realization of bounce gait in a quadruped robot with articular-joint-type legs. In *Proceedings of IEEE International Conference on Robotics and Automation*, volume 1, pages 697–702. IEEE, 1995.

[44] P. P. Gambaryan and H. Hardin. *How mammals run: anatomical adaptations*. Wiley, 1974.

[45] S. Gracovetsky. *The spinal engine*. Springer-Verlag, 1988.

[46] B. Graf, R.D. Schraft, and J. Neugebauer. A mobile robot platform for assistance and entertainment. In *International Symposium on Robotics, Montreal, Canada*. Citeseer, 2000.

[47] C. S. Gregersen, N. A. Silverton, and D. R. Carrier. External work and potential for elastic storage at the limb joints of running dogs. *The Journal of experimental biology*, 201(23):3197, 1998.

[48] Timothy M. Griffin, Rodger Kram, Steven J. Wickler, and Donald F. Hoyt. Biomechanical and energetic determinants of the walk-trot transition in horses. *Journal of Experimental Biology*, 207(24):4215–4223, November 15 2004.

[49] Remi Hackert. *Dynamics of pikas' half-bound : spinal flexion contributes to dynamic stability.* PhD thesis, Jena, 2003.

[50] Remi Hackert, Nadja Schilling, and Martin S. Fischer. Mechanical self-stabilization, a working hypothesis for the study of the evolution of body proportions in terrestrial mammals? *Comptes Rendus Palevol*, 5(3-4):541–549, 2006.

[51] M. W. Hannan and I. D. Walker. Analysis and initial experiments for a novel elephant's trunk robot. In *Proceedings of the IEEE/RSJ International Conference on Intelligent Robots and Systems*, volume 1, pages 330–337 vol.1, 2000.

[52] M. Hardt and O. von Stryk. Dynamic modeling in the simulation, optimization, and control of bipedal and quadrupedal robots. *Zeitschrift fur Angewandte Mathematik und Mechanik*, 83(10):648–62, 2003.

[53] N. C. Heglund, M. A. Fedak, C. R. Taylor, and G. A. Cavagna. Energetics and mechanics of terrestrial locomotion. IV. total mechanical energy changes as a function of speed and body size in birds and mammals. *The Journal of experimental biology*, 97:57, 1982.

[54] N. C. Heglund and C. R. Taylor. Speed, stride frequency and energy cost per stride: how do they change with body size and gait? *Journal of Experimental Biology*, 138(1):301–318, Sept. 1988.

[55] N. C. Heglund, C. R. Taylor, and T. A. McMahon. Scaling stride frequency and gait to animal size: Mice to horses. *Science*, 186(4169):1112–1113, December 20 1974.

[56] B. Hennion, J. Pill, and J.C. Guinot. A biologically inspired model for quadruped locomotion. *Climbing and Walking Robots*, pages 49–56, 2006.

[57] H. M. Herr, G. T. Huang, and T. A. McMahon. A model of scale effects in mammalian quadrupedal running. *Journal of experimental biology*, 205(7):959–967, 2002.

[58] H. M. Herr and T. A. McMahon. A trotting horse model. *The International Journal of Robotics Research*, 19(6):566–581, June 1 2000.

[59] H. M. Herr and T. A. McMahon. A galloping horse model. *The International Journal of Robotics Research*, 20(1):26–37, January 1 2001.

[60] M. Hildebrand. Motions of the running cheetah and horse. *Journal of Mammalogy*, 40(4):481–495, Nov. 1959.

[61] M. Hildebrand. Further studies on locomotion of the cheetah. *Journal of mammalogy*, 42(1):84–91, Feb. 1961.

[62] M. Hildebrand. The quadrupedal gaits of vertebrates. *Bioscience*, 39(11, Animals in Motion):766–775, Dec. 1989.

[63] P. Holmes, R. J. Full, D. Koditschek, and J. Guckenheimer. The dynamics of legged locomotion: Models, analyses, and challenges. *SIAM Review*, 48(2):207–304, June 2006.

[64] Donald F. Hoyt and C. Richard Taylor. Gait and the energetics of locomotion in horses. *Nature*, 292(5820):239–240, July 1981.

[65] S. H. Hyon, X. Jiang, T. Emura, and T. Ueta. Passive running of planar 1/2/4-legged robots. In *Proceedings of IEEE/RSJ International Conference on Intelligent Robots and Systems*, volume 4, pages 3532–3539. IEEE, 2004.

[66] F. Iida, R. Dravid, and C. Paul. Design and control of a pendulum driven hopping robot. In *Proceedings of IEEE/RSJ International Conference on Intelligent Robots and Systems*, volume 3, pages 2141–6. IEEE, 2002.

[67] F. Iida, G. Gomez, and R. Pfeifer. Exploiting body dynamics for controlling a running quadruped robot. In *Proceedings of 12th International Conference on Advanced Robotics*, pages 229–235, 2005.

[68] F. Iida and R. Pfeifer. Cheap rapid locomotion of a quadruped robot: Self-stabilization of bounding gait. *Intelligent Autonomous Systems*, 8:642–649, 2004.

[69] T. Ishida. Development of a small biped entertainment robot qrio. In *Proceedings of the 2004 International Symposium on Micro-Nanomechatronics and Human Science, 2004 and The Fourth Symposium Micro-Nanomechatronics for Information-Based Society, 2004*, pages 23–28, 2004.

[70] K.W. Jeong, I.J. Cho, and Y.J. Lee. Development of autonomous eating mechanism for biomimetic robots. In *Proceedings of SPIE*, volume 6042, page 60423G, 2005.

[71] Theodore Garland Jr. Scaling the ecological cost of transport to body mass in terrestrial mammals. *The American Naturalist*, 121(4):571–587, Apr. 1983.

[72] Karčnik, T. Stability in legged locomotion. *Biological cybernetics*, 90(1):51–58, 2004.

[73] T. S. Keller, A. M. Weisberger, J. L. Ray, S. S. Hasan, R. G. Shiavi, and D. M. Spengler. Relationship between vertical ground reaction force and speed during walking, slow jogging, and running. *Clinical Biomechanics*, 11(5):253–259, 1996.

[74] Kyoung-Ho Kim, Se-Hoon Park, and Yun-Jung Lee. Development of biomimetic quadruped walking robot with 2-dof waist joint. In *Proceedings of SPIE*, page 60422. SPIE, December 2005.

[75] H. Kimura, S. Akiyama, and K. Sakurama. Realization of dynamic walking and running of the quadruped using neural oscillator. *Autonomous Robots*, 7(3):247–58, 11 1999.

[76] H. Kimura, Y. Fukuoka, and A. H. Cohen. Biologically inspired adaptive walking of a quadruped robot. *Philosophical Transactions of the Royal Society A: Mathematical, Physical and Engineering Sciences*, 365(1850):153–170, Jan. 2007.

[77] D. E. Koditschek, J. Robert, and M. Buehler. Mechanical aspects of legged locomotion control. *Arthropod Structure & Development*, 33:251–272, 2004.

[78] R. Kram and C.R. Taylor. Energetics of running: a new perspective. *Nature*, 1990.

[79] D. P. Krasny and D. E. Orin. Generating high-speed dynamic running gaits in a quadruped robot using an evolutionary search. *IEEE Transactions on Systems, Man, and Cybernetics, Part B*, 34(4):1685–1696, 2004.

[80] D. P. Krasny and D. E. Orin. Evolution of dynamic maneuvers in a 3d galloping quadruped robot. In *Proceedings of IEEE International Conference on Robotics and Automation.*, pages 1084–1089. IEEE, 2006.

[81] A. D. Kuo, J. M. Donelan, and A. Ruina. Energetic consequences of walking like an inverted pendulum: step-to-step transitions. *Exercise and sport sciences reviews*, 33(2):88, 2005.

[82] D. V. Lee, J. E. A. Bertram, and R. J. Todhunter. Acceleration and balance in trotting dogs. *Journal of Experimental Biology*, 202(24):3565–3573, December 15 1999.

[83] D. V. Lee, M. P. McGuigan, E. H. Yoo, and A. A. Biewener. Compliance, actuation, and work characteristics of the goat foreleg and hindleg during level, uphill, and downhill running. *Journal of applied physiology*, 104(1):130, 2008.

[84] K. F. Leeser. Locomotion experiments on a planar quadruped robot with articulated spine. Master's thesis, Massachusetts Institute of Technology, 1996.

[85] W. A. Lewinger. *Insect-inspired, actively compliant robotic hexapod*. PhD thesis, Case Western Reserve University, 2005.

[86] M. A. Lewis. *Self-organization of locomotory controllers in robots and animals*. PhD thesis, University of Southern California, 1996.

[87] D. W. Marhefka, D. E. Orin, J. P. Schmiedeler, and K. J. Waldron. Intelligent control of quadruped gallops. *Mechatronics, IEEE/ASME Transactions on*, 8(4):446–456, 2003.

[88] T. Matsuki, I. Mizuuchi, S. Kagami, M. Inaba, and H. Inoue. Motion generation and action control of a walking quadruped robot with flexible spine structure. *Nippon Kikai Gakkai Robotikusu, Mekatoronikusu Koenkai Koen Ronbunshu*, 2, 1999.

[89] M. L. McEwen and J. E. Springer. Quantification of locomotor recovery following spinal cord contusion in adult rats. *Journal of neurotrauma*, 23(11):1632–1653, Nov 2006.

[90] I. Mizuuchi, M. Inaba, and H. Inoue. A flexible spine human-form robot-development and control of the posture of the spine. In *Proceedings of RSJ/IEEE International Conference on Intelligent Robots and Systems*, volume 4, pages 2099–104. IEEE, 2001.

[91] I. Mizuuchi, Y. Kuniyoshi, R. Tajima, H. Inoue, K. Nagashima, D. Sato, T. Yoshikai, and M. Inaba. The design and control of the flexible spine of a fully tendon-driven humanoid "Kenta". *Proceedings IEEE/RSJ International Conference on Intelligent Robots and Systems*, 3:2527–32, 2002.

[92] I. Mizuuchi, T. Matsuki, M. Inaba, and H. Inoue. Ga-based motion generation for quadruped robot which has soft spine structure. *Nippon Robotto Gakkai Gakujutsu Koenkai Yokoshu*, 17(199-200), 1999.

[93] I. Mizuuchi, S. Yoshida, M. Inaba, and H. Inoue. The development and control of a flexible-spine for a human-form robot. *Advanced Robotics*, 17(2):179–96, 2003.

[94] I. Mizuuchi, T. 1. Yoshikai, M. 1. Inaba, and Y. 1. Nakanishi. A reinforceable-muscle flexible-spine humanoid "Kenji". *2005 IEEE/RSJ International Conference on Intelligent Robots and Systems*, pages 4143–8, 2005.

[95] S. Mochon and T. A. McMahon. Ballistic walking. *J Biomech*, 13(1):49–57, 1980.

[96] J. M. Morrey, B. Lambrecht, A. D. Horchler, R. E. Ritzmann, and R. D. Quinn. Highly mobile and robust small quadruped robots. In *Proceedings of IEEE/RSJ International Conference on Intelligent Robots and Systems, 2003.*, volume 1, pages 82–87, 2003.

[97] A. Muraro, C. Chevallereau, and Y. Aoustin. Optimal trajectories for a quadruped robot with trot, amble and curvet gaits for two energetic criteria. *Multibody System Dynamics*, 9(1):39–62, 02/01/ 2003.

[98] P. Nanua. *Dynamics of a galloping quadruped*. PhD thesis, Ohio State University, 1992.

[99] P. Nanua and K. J. Waldron. Instability and chaos in quadruped gallop. *Journal of Mechanical Design*, 116(4):1096–1101, Dec. 1994.

[100] P. Nanua and K. J. Waldron. Energy comparison between trot, bound, and gallop using a simple model. *Journal of Biomechanical Engineering*, 117(4):466–473, Nov. 1995.

[101] A. Neishtadt and Z. Li. Stability proof of raibert's four-legged hopper in bounding gait. Technical Report 578, New York State University, 1991.

[102] H. G. Nguyen and J. P. Bott. Robotics for law enforcement: Applications beyond explosive ordnance disposal. In *SPIE Proc. 4232: Technologies for Law Enforcement*, pages 5–8, 2000.

[103] J. G. Nichol, S. P. N. Singh, K. J. Waldron, L. R. Palmer III, and D. E. Orin. System design of a quadrupedal galloping machine. *International Journal of Robotics Research*, 23(10):1013–27, Oct. 2004.

[104] C. Nielsen, S. M. Stover, K. S. Schulz, M. Hubbard, and D. A. Hawkins. Two-dimensional link-segment model of the forelimb of dogs at a walk. *American Journal of Veterinary Research*, 64(5):609–617, 2003.

[105] J. Nilsson and A. Thorstensson. Ground reaction forces at different speeds of human walking and running. *Acta Physiologica Scandinavica*, 136(2):217–227, 1989.

[106] Jun Nishii. An analytical estimation of the energy cost for legged locomotion. *Journal of Theoretical Biology,*, 238(3):636–645, 2/7 2006.

[107] D. M. Nunamaker and P. D. Blauner. Normal and abnormal gait. In *Textbook of small animal orthopedics*, pages 1083–1095. JB Lippincott, 1985.

[108] Hamid A. Oral. Legged locomotion review. In *Proceedings of the 2nd Biennial European Joint Conference on Engineering Systems Design and Analysis. Part 8-C (of 8), Jul 4-7 1994*, volume 64 of *American Society of Mechanical Engineers*,

Petroleum Division (Publication) PD, pages 837–847, London, Engl, 1994. Istanbul Technical Univ, Turk, Publ by ASME, New York, NY, USA.

[109] J. Osada, S. Ohnaka, and M. Sato. The scenario and design process of childcare robot, papero. In *Proceedings of the 2006 ACM SIGCHI International Conference on Advances in Computer Entertainment Technology*, page 80, 2006.

[110] Se-Hoon Park and Yun-Jung Lee. Discontinuous zigzag gait planning of a quadruped walking robot with a waist-joint. *Advanced Robotics*, 21(1):143–164, Jan. 2007.

[111] Elizabeth Pennisi. Evolution: Robot suggests how the first land animals got walking. *Science*, 315(5817):1352a–1353, March 9 2007.

[112] R. Pfeifer, F. Iida, and J. Bongard. New robotics: design principles for intelligent systems. *Artificial Life*, 11(1):99–120, 2005.

[113] R. Playter, M. Buehler, and M. H. Raibert. Bigdog. In *Proceedings of SPIE*, volume 6230, page 62302O. SPIE, May 2006.

[114] I. Poulakakis, E. Papadopoulos, and M. Buehler. On the stability of the passive dynamics of quadrupedal running with a bounding gait. *The International Journal of Robotics Research*, 25(7):669, 2006.

[115] I. Poulakakis, J. A. Smith, and M. Buehler. Modeling and experiments of untethered quadrupedal running with a bounding gait: the Scout II robot. *International Journal of Robotics Research*, 24(4):239–56, 04 2005.

[116] I. Poulakakis, J. A. Smith, and M. Buehler. On the dynamics of bounding and extensions towards the half-bound and the gallop gaits. *Adaptive Motion of Animals and Machines*, pages 77–86, 2005.

[117] M. H. Raibert. *Legged Robots That Balance*. The MIT Press, Cambridge, MA, 1985.

[118] M. H. Raibert. Legged robots. *Communications of the ACM*, 29(6):499–514, 1986.

[119] M. H. Raibert. Running with symmetry. *The International journal of robotics research*, 5(4):3, 1986.

[120] M. H. Raibert. Trotting, pacing and bounding by a quadruped robot. *Journal of Biomechanics*, 23(Supplement 1):79–81, 1990.

[121] M. H. Raibert. Dynamic legged locomotion in robots and animals. Technical report, NASA STI/Recon, 1995.

[122] M. H. Raibert, M. Chepponis, and H. B. Brown Jr. Running on four legs as though they were one. *IEEE Journal of Robotics and Automation*, 2(2):70–82, 1986.

[123] J. R. Rebula, P. D. Neuhaus, B. V. Bonnlander, M. J. Johnson, and J. E. Pratt. A controller for the littledog quadruped walking on rough terrain. In *Robotics and Automation, 2007 IEEE International Conference on*, pages 1467–1473, 2007. VL:.

[124] L. Righetti and A. J. Ijspeert. Pattern generators with sensory feedback for the control of quadruped locomotion, 2008.

[125] J. Riskin. The defecating duck, or, the ambiguous origins of artificial life. *Critical Inquiry*, 29(4):599–633, 2003.

[126] R. E. Ritzmann. Control of obstacle climbing in the cockroach, Blaberus discoidalis. I. Kinematics. *Journal of comparative physiology A: Neuroethology, Sensory, Neural, and Behavioral Physiology*, 188(1):39, 2002.

[127] Andy Ruina, John E. A. Bertram, and Manoj Srinivasan. A collisional model of the energetic cost of support work qualitatively explains leg sequencing in walking and galloping, pseudo-elastic leg behavior in running and the walk-to-run transition. *Journal of theoretical biology*, 237(2):170–192, Nov. 2005.

[128] U. Scarfogliero, C. Stefanini, and P. Dario. A bioinspired concept for high efficiency locomotion in micro robots: the jumping robot grillo. In *Proceedings of IEEE International Conference on Robotics and Automation, 2006*, pages 4037–4042, 2006.

[129] Nadja Schilling and Remi Hackert. Sagittal spine movements of small therian mammals during asymmetrical gaits. *Journal of Experimental Biology*, 209(19):3925–3939, October 1 2006.

[130] J. P. Schmiedeler. *The mechanics of and robotic design for quadrupedal galloping*. PhD thesis, Ohio State University, 2001.

[131] J. P. Schmiedeler, D. W. Marhefka, D. E. Orin, and K. J. Waldron. A study of quadruped gallops. In *Proceedings of 2001 NSF Design, Service, and Manufacturing Grantees and Research Conference*, 2001.

[132] J. P. Schmiedeler and K. J. Waldron. The mechanics of quadrupedal galloping and the future of legged vehicles. *The International Journal of Robotics Research*, 18(12):1224–1234, December 1 1999.

[133] Andre Seyfarth, Hartmut Geyer, and Hugh Herr. Swing-leg retraction: a simple control model for stable running. *Journal of Experimental Biology*, 206(15):2547–2555, August 1 2003.

[134] N.C.C. Sharp. Timed running speed of a cheetah (Acinonyx jubatus). *Journal of Zoology*, 241(3):493–494, 1997.

[135] M. F. Silva, J. A. T. Machado, and A. M. Lopes. Modelling and simulation of artificial locomotion systems. *Robotica*, 23:595–606, 2005.

[136] M. F. Silva and J. A. Tenreiro Machado. Energy efficiency of quadruped gaits, 2006.

[137] M. F. Silva and J. A. Tenreiro Machado. Kinematic and dynamic performance analysis of artificial legged systems. *Robotica*, pages 1–21, June 2007.

[138] T. H. Smit. The use of a quadruped as an *in vivo* model for the study of the spine - biomechanical considerations. *European spine journal*, 11(2):137–144, Apr 2002.

[139] S. M. Song and K. J. Waldron. *Machines that walk: the adaptive suspension vehicle*. The MIT Press, 1989.

[140] T. Standage. *The Turk: The Life and Times of the Famous Eighteenth-century Chess-playing Machine*. Walker & Co, 2002.

[141] J. R. Usherwood and A. M. Wilson. Biomechanics: no force limit on greyhound sprint speed. *Nature*, 438(7069):753–754, 2005.

[142] K. J. Waldron. Energy comparison between trot, bound, and gallop using a simple model. *Journal of biomechanical engineering*, 117(4):466, 1995.

[143] Rebecca M. Walter and David R. Carrier. Ground forces applied by galloping dogs. *Journal of Experimental Biology*, 210(2):208–216, January 15 2007.

[144] Zhiqiang Weng and Hidekazu Nishimura. Final-state control of a two-link cat robot. *Advanced Robotics*, 16:325–343(19), 1 July 2002.

[145] P. G. Weyand, R. F. Sandell, D. N. L. Prime, and M. W. Bundle. The biological limits to running speed are imposed from the ground up. *Journal of applied physiology*, 108(4):950, 2010.

[146] P. G. Weyand, D. B. Sternlight, M. J. Bellizzi, and S. Wright. Faster top running speeds are achieved with greater ground forces not more rapid leg movements. *Journal of applied physiology*, 89(5):1991, 2000.

[147] S. J. Wickler, D. F. Hoyt, E. A. Cogger, and R. McGuire. The cost of transport in an extended trot. *Equine Veterinary Journal*, 34(S34):126–130, 2002.

[148] S. B. Williams, J. R. Usherwood, K. Jespers, A. J. Channon, and A. M. Wilson. Exploring the mechanical basis for acceleration: pelvic limb locomotor function during accelerations in racing greyhounds (canis familiaris). *Journal of Experimental Biology*, 212(4):550, 2009.

[149] S. B. Williams, A. M. Wilson, L. Rhodes, J. Andrews, and R. C. Payne. Functional anatomy and muscle moment arms of the pelvic limb of an elite sprinting athlete: the racing greyhound (*Canis familiaris*). *Journal of anatomy*, 213(4):361–372, 2008.

[150] D. A. Winter. A new definition of mechanical work done in human movement. *Journal of Applied Physiology*, 46(1):79, 1979.

[151] Z. G. Zhang, H. Kimura, and Y. Fukuoka. Autonomously generating efficient running of a quadruped robot using delayed feedback control. *Advanced Robotics*, 20(6):607–629, 2006.

[152] H. Zou and J. P. Schmiedeler. The effect of asymmetrical body-mass distribution on the stability and dynamics of quadruped bounding. *IEEE Transactions on Robotics*, 22(4):711–723, 2006.